Extended Solid Earth Science ESDR System (ES^3):

Algorithm Theoretical Basis Document (ATBD)

February 17, 2022

MEaSUREs ROSES-17

Yehuda Bock, Peng Fang, Alistair Knox, Anne Sullivan, Songnian Jiang
Katherine Guns, Dorian Golriz

Scripps Institution of Oceanography

&

Angelyn Moore, Donald Argus, Zhen Liu, Sharon Kedar

Jet Propulsion Laboratory

MEaSUREs Web Pages
http://sopac-csrc.ucsd.edu/index.php/measures-2/

MGViz: Map and GNSS Products Visualization
http://mgviz.ucsd.edu

Table of Contents

1. Overview

Since its inception in the early 1980's, GPS/GNSS geodesy has contributed to a wide range of scientific and societal applications including tectonic motion, crustal deformation, natural and anthropogenic processes and hazards, including earthquakes, tsunamis, volcanoes, the cryosphere, extreme weather, sea level rise, climate change and hydrology. Our project "Extended Solid Earth Science ESDR System" (ES^3), a continuation and expansion of the MEaSUREs "Solid Earth Science ESDR System" (SESES) project (2012-2018), provides the basic infrastructure, data and data products for these applications. It is a collaborative effort of the Jet Propulsion Laboratory (JPL) and Scripps Institution of Oceanography (SIO) and its Scripps Orbit and Permanent Array Center (SOPAC). The Earth Science Data Records (ESDRs) from SESES (Table 1, items 1.1-1.5) now span thirty years for the earliest stations and are now available for thousands of global and regional continuous GPS stations (Figure 1). These ESDRs will continue to be generated for a significantly expanded list of stations. In ES^3 we provide four new ESDRs (Table 1, items 2.1-2.3): (1) continuous high-rate (1 Hz) geodetic (GNSS) and seismogeodetic displacement records for historical earthquakes, (2) slow slip events (SSEs), including episodic tremor and slip (ETS) in Cascadia, (3) weekly displacement and strain rate grids, and (4) total near-surface water content over the Western U.S. We are incorporating technological developments including GPS modernization, multiple satellite constellations (GNSS) and new processing methods.

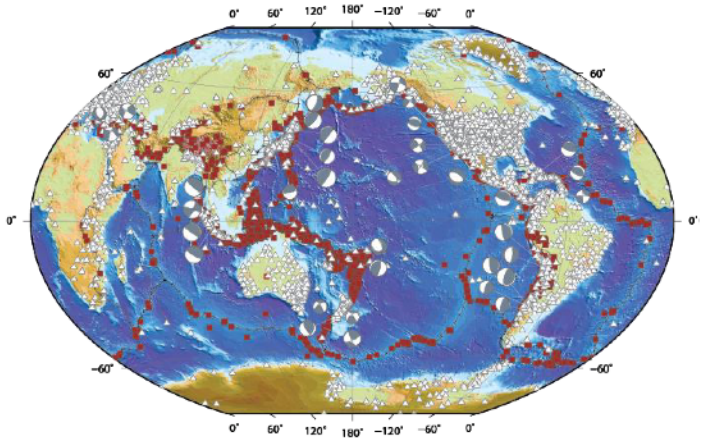

Figure 1. The project is adding new ESDRs (Table 1) to enhance geographical coverage with hundreds of additional GNSS stations (white triangles) focusing on tectonic plate boundaries (black lines) for crustal deformation and natural hazards applications, and the continental U.S. for near-surface water content. Shown are earthquakes greater than magnitude 5 (brown squares) since 1990 with their global centroid moment tensor (CMT) solutions.

The purpose of this document is to describe the ES^3 data products and the theoretical basis for their generation.

The ESDRs for the project (Table 1) are captured schematically in the flow diagram (Figure 2). They begin with the production of two Level 1 products: (1) long-term daily and continuous raw displacement time series that are generated using identical GNSS observations (carrier phase and pseudorange) and metadata stored in a unified database maintained at SOPAC (http://garner.ucsd.edu/pub/ - username: anonymous; password: your email address). The JPL and SOPAC displacement time series are generated using independent processing strategies and

software: the GipsyX Network Processor (NWPx) and GAMIT/GLOBK software, respectively; (2) troposphere delay estimates at two intervals (5 and 60 minutes at JPL and 60 minutes at SOPAC; and (3) high-rate GNSS and seismogeodetic (GNSS + accelerometer data) waveforms at SOPAC. Level 2 ESDRs are calibrated and validated: (1) combined daily displacement time series (Figure 3) that underly the generation of higher-level ESDRs[1]; (2) troposphere and precipitable water time series at 5-minute intervals by JPL; and (3) high-rate displacement and seismic velocity waveforms for historical earthquakes at SOPAC.

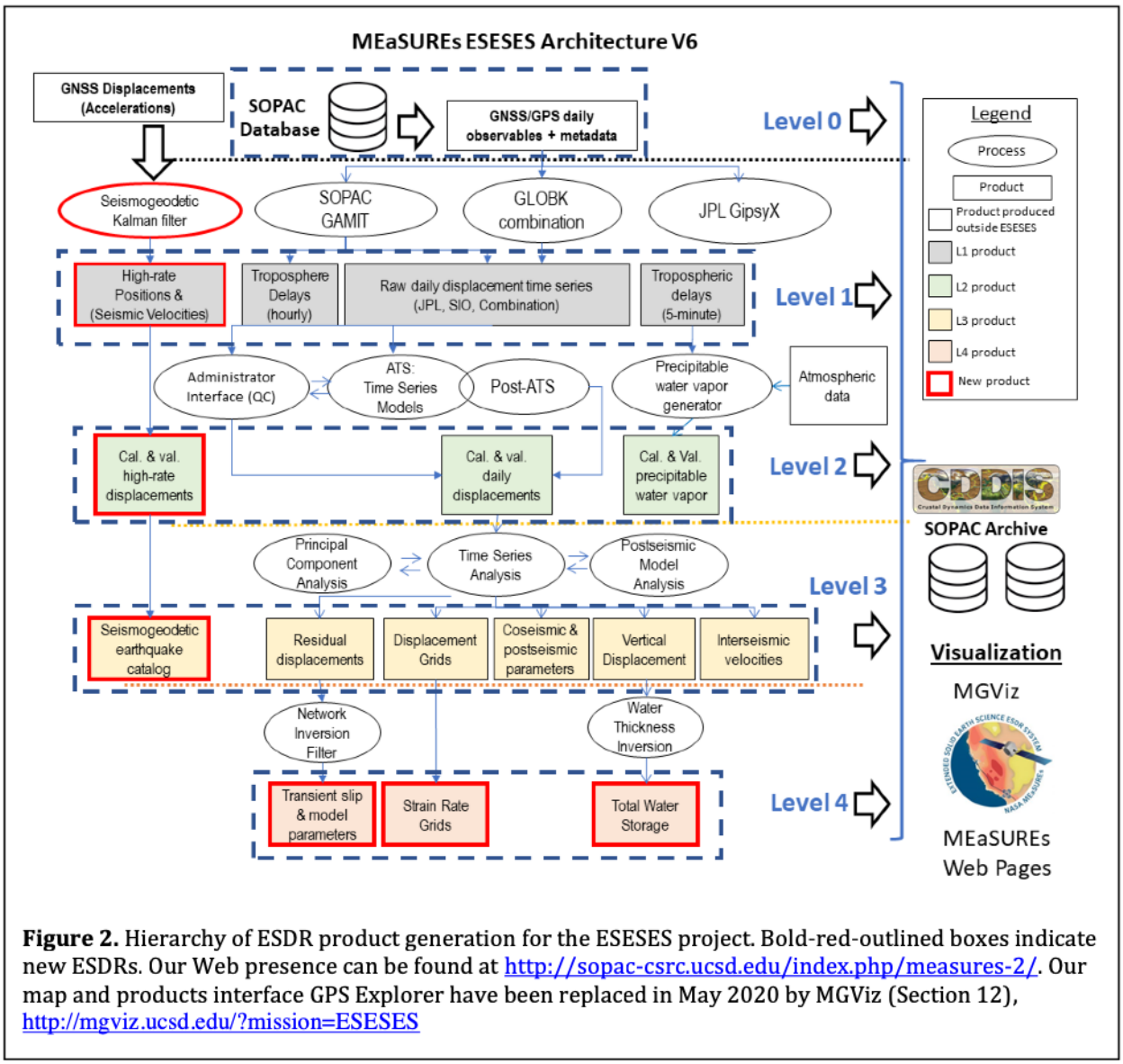

Figure 2. Hierarchy of ESDR product generation for the ESESES project. Bold-red-outlined boxes indicate new ESDRs. Our Web presence can be found at http://sopac-csrc.ucsd.edu/index.php/measures-2/. Our map and products interface GPS Explorer have been replaced in May 2020 by MGViz (Section 12), http://mgviz.ucsd.edu/?mission=ESESES

[1] This data production model originates in the recommendations from the science advisory council of the Southern California Integrated GPS Network (SCIGN) project and adopted by the Plate Boundary Observatory (PBO) and other monitoring projects.

The Level 3 ESDRs are derivatives of Level 2, Including, (1) estimated displacement time series parameters (residuals, coseismic and postseismic, interseismic velocities and vertical displacements), (2) displacement grids including steady-state and physical transient motions (postseismic, hydrological, magmatic, etc.), and (3) seismogeodetic catalog of historical earthquakes. Level 4 include derived ESDRs: (1) transient slip and models in particular ETS events in Cascadia (JPL), (2) strain-rate grids (SOPAC), and (3) total water storage for hydrological studies (JPL).

All projects ESDRs are stored at NASA's Archive of Space Geodetic Data (CDDIS) under "GPS Explorer"–- https://cddis.nasa.gov/archive/GPS_Explorer/. The ESDRs are also available at the SOPAC archive–- http://garner.ucsd.edu/pub/measuresESESES_products/ (username: anonymous; password: your e-mail address).

Table 1: Original proposed hierarchy of ESDRs from the ESESES proposal to NASA's MEaSUREs program, which has been subsequently been modified as described in this ATBD document.

Table 1: ESDRs to be produced under ESESES and their response to the Science Challenges posed by NASA's Earth Surface and Interior

	ESDR	ESDR Description	Level	Algorithm Source	Need / Usage	CORE 2016* Sci. Challenge						
						1	2	3	4	5	6	7
Continued Production (MEaSUREs 2012)	1.1 Global Calibrated/Validated Geodetic Displacement Time Series	Daily, combined, cleaned and filtered, GIPSY-GAMIT long-term time series of CGPS station positions (global and regional) in the latest version of ITRF, automatically updated weekly.	1&2	NASA REASoN; MEaSUREs 2006 & 20012	Basis for all higher-level products. Need identified in CORE 2016.	X			X	X		
	1.2 Global Calibrated/Validated Geodetic Velocities	Weekly updated velocity field + velocity field histories in various reference frames; compendium of all model parameters including earthquake catalog, coseismic offsets, and postseismic model parameters (exponential or logarithmic).	2		Long-term, high-resolution monitoring of changes in Earth's surface addressing. Need identified in CORE 2016.	X			X	X		
	1.3 Calibrated/Validated Troposphere Delay Time Series	Long-term time series of troposphere delay (30-min resolution) at geodetic stations, necessarily estimated during position time series production and automatically updated weekly.	2	(Davis, 1985; Bevis, 1992) JPL + NASA AIST + MEaSUREs 2012	Forms the basis for Precipitable Water Vapor (PWV) ESDR and calibration maps for InSAR.	X			X	X		
	1.4 Calibrated/Validated Precipitable Water Vapor Time Series	Long-term time series of precipitable water vapor (PWV) at geodetic (global and regional) stations, automatically updated weekly.	2		Addresses key areas of uncertainty in the climate system and its potential changes (Gaffen, 2000).		X	X				
	1.5 Seismogeodetic records for historic earthquakes	High-rate broadband displacement and seismic velocity time series combining 1 Hz GPS displacements and 100 Hz accelerometer data for select large earthquakes and collocated CGPS and seismic instruments from regional networks.	3	NASA AIST 2008 + MEaSUREs 2012	Finite fault slip models, earthquake early warning and rapid response algorithms.	X				X		
New ESDRs	2.1 Continuous High-Rate Position time series	Multi-year continuous high-rate geodetic and seismogeodetic time series in tectonically active regions.	2	Penna et al. 2015	Investigate the full spectrum of Earth motions, transition from seismic to geodetic motions.	X			X	X		
	2.2 Plate Boundary Aseismic Transients	Cataloging and parameterizing transient deformation in tectonically active areas known for aseismic transient motion such as episodic tremor and slip (ETS), first discovered in Japan and Cascadia.	4	Crowell et al., 2016 + Liu et al., 2010, 2015b	Continuous monitoring of the state of subduction plate boundary; earthquake-cycle study and seismic hazard	X				X		
	2.3 Change in Total Water Storage Time Series	Continuous estimation and cataloging of total near-surface water content derived from continuous GNSS time series over the continental U.S.	4	NASA ESI 2013	Determination of changes in total water storage at high resolution to constrain snow, soil moisture, and groundwater		X	X				X

A quick reference to all our products, relevant features and their access locations will be shortly available in our archive at http://garner.ucsd.edu/pub/measuresESESES_products/. In addition, the products are fully described in the relevant sections of this document.

2. Displacement Time Series (Levels 1-2)

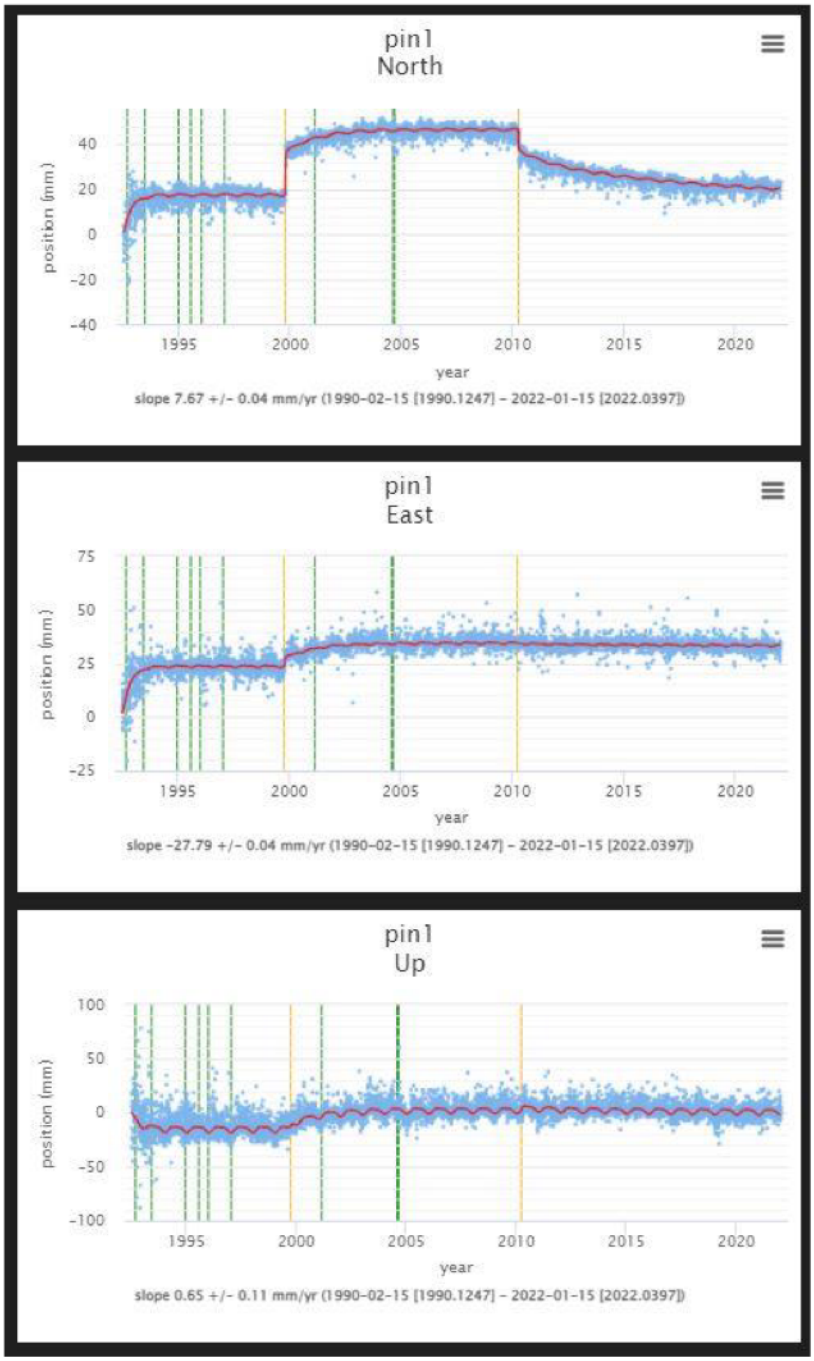

Figure 3: Example of combined displacement time series using the weighted mean approach. Unfiltered combined displacement time series (section 2.1.4) in North, East, and Up components for station PIN1 from July 1992 to January 2022. The time series are detrended and include the effects of coseismic (orange vertical lines) and postseismic deformation. The L1-level time series have gone through extensive calibration and validation (section 2.1.11) to produce these L2-level time series (Figure 2). Dashed black vertical lines denote non-tectonic offsets that have been corrected, primarily due to unlike antenna changes. The early scatter in the data (1992-1995) is due to insufficient infrastructure for GPS orbit and reference frame determination preceding the establishment of the International GNSS Service (e.g., Noll et al., 2009).

2.1. Methods

Definition: Long-term daily three-dimensional displacement time series of GNSS global and regional stations.

Both the JPL and the SOPAC analysis centers use the Level 0 GPS observables, consisting of multi-frequency phase and pseudorange observations stored in Hatanaka-compressed (https://terras.gsi.go.jp/ja/crx2rnx.html) RINEX files (Figure 2). In addition, we use a single source of station information (metadata) stored in the SOPAC archive to ensure maximum consistency between our respective displacement time series and higher-level products. The stations used are identified by a master list of global and regional continuous GPS stations that is maintained through the SOPAC archive and database (http://garner.ucsd.edu/pub/ - username: anonymous; password: your email address). The primary metadata consist of nominal station ITRF2014 positions, GPS equipment (receiver and antenna) models and serial numbers, and antenna offsets from the monument reference point. Changes in the metadata are entered into the database and reflected in IGS-formatted site logs obtained from other data centers, as well as for those stations managed by SOPAC (http://sopac-csrc.ucsd.edu/index.php/sitelogs/).

2.1.1 JPL GIPSY Analysis & Raw Time Series

Processing strategy–- Precise Point Positioning

The JPL Level 1 ESDR consists of daily GNSS station positions estimated using the GipsyX Network Processor (NWPx), which runs the GipsyX GPS data analysis software. The NWPx has been developed to analyze daily positions for large GPS networks using precise point positioning (PPP) (*Zumberge et al.*, 1997) with ambiguity resolution (*Bertiger et al.*, 2010) in a no-net-rotation frame, later transformed into the IGS realization of ITRF. In the PPP strategy, satellite clock and orbits are fixed to the values provided from a separate precise orbit determination process. The JPL analysis uses their final (also historically termed JPL FLINN) no-net-rotation orbits and satellite clock data products, which are the highest precision orbits released by JPL, with a latency of 4-14 days to allow for remote stations with slower data transmission to be included.

Analysis strategy and physical models

1. Solid Earth tides (IERS 2010 convention (*Petit and Luzum*, 2010))
2. Ocean tidal loading (IERS 2010 convention)
3. Pole tide (IERS 2010 convention)
4. Satellite yaw model (GYM95 (*Bar-Sever*, 1996))
5. GPT2w (*Boehm*, 2015) tropospheric mapping function for hydrostatic and wet components of the troposphere
6. JPL Small-Body Database (https://ssd.jpl.nasa.gov/tools/sbdb_lookup.html#/) for solar and lunar effects and nutation
7. General relativity effect (periodic clock corrections and gravity bending corrections applied) (IERS 2010 convention)
8. Absolute IGS phase center maps for receiver and transmitter antennas (https://files.igs.org/pub/station/general/antenna_README.pdf)

9. GNSS data observations decimated to 5-minute intervals
10. Elevation angle cut-off set at 7 degrees.

An atmospheric tidal loading model is currently not applied. The wet zenith delay and two tropospheric gradient parameters are estimated as random walk parameters, updated every 5 minutes (*Bar-Sever et al*., 1998), with variance of 5 x 10^{-8} km/sqrt(sec) and 5x10^{-9} km/sqrt(sec), respectively.

A priori information and constraints

The GNSS analysis software requires the following a priori information for each station: station coordinates, antenna and receiver equipment type, phase center offsets for antenna, and the vector from the station monument to the reference point on the antenna. These metadata are kept up-to-date by SOPAC and are managed through its Oracle database. JPL retrieves this information from an XML file generated from the database and placed in the SOPAC archive for retrieval via http. A priori values for hydrostatic and wet delays are extracted from the GPT2w model (*Boehm*, 2015).

Ambiguity Resolution

Single station ambiguity resolution is performed using Wide Lane Phase Bias Files delivered with the JPL orbits (*Bertiger et al*., 2010).

Raw 3-D daily displacements and variance-covariance matrices

The GipsyX solutions are stored in daily STACOV files, available from http://garner.ucsd.edu/pub/solutions/gipsy/. There are two files in each directory:

(1) The constrained solution with the XYZ station positions and the (symmetric) 3x3 variance-covariance matrix for each station (represented by six elements corresponding to 3 sigma values and 3 correlations); the cross-station covariances are zero and are not explicitly printed, according to the stacov format. (e.g., http://garner.ucsd.edu/pub/solutions/gipsy/2022/001/2022-01-01.stacov.gz) . The station positions resulting from this analysis are in a non-fiducial frame, defined by the orbits and clocks used in the PPP analysis. These station positions are then rotated with minimal internal constraints into the ITRF2014 (*Altamimi et al*., 2016) using a 7-parameter Helmert transformation, defined in a file provided with the JPL precise satellite ephemeris. The XYZ positions and full variance-covariance matrices extracted from the STACOV files are uploaded to the SOPAC database, extracted and converted to NEU coordinates as described in section 2.1.4. The reference epoch is chosen as the date of the first RINEX file, stored in the SOPAC database and extracted from IGS station log files.

The daily station-by-station NEU displacements and uncertainties (section 2.1.4), making up the JPL Level 1 "raw" displacement time series (section 2.2).

(2) The loosely-constrained STACOV file with XYZ station positions and full variance-covariance matrices (e.g., http://garner.ucsd.edu/pub/solutions/gipsy/2022/001/2022-01-01.stacov.loose.gz). These are the same coordinates as the constrained solution, but

loosened with the following parameters: rotation = 3189 mm, translation = 40 mm, scale = 1.91134411 mm. The daily loosely-constrained STACOV files are input to the GLOBK software along with the loosely-constrained GAMIT h-files to produce a combination solution (section 2.1.3). **[However, we now use the weighted mean approach for our "official" combination solutions].**

2.1.2 SOPAC GAMIT Analysis

Processing Strategy–- Distributed sub-network processing

Daily GPS processing is carried out using the GAMIT/GLOBK software (http://www-gpsg.mit.edu/~simon/gtgk/; http://sopac-csrc.ucsd.edu/index.php/gambit-globk/; (*Herring et al.*, 2018) using a distributed processing approach (*Zhang,* 1996) on two sets of stations: global and regional. Both solutions use 24-hour (0:00-23:59:30 GPST) RINEX-formatted data sampled at 30 s. The global solution uses data from 300+ IGS sites, divided into multiple (~8) sub-networks. The regional solution uses data from approximately 2000 western North America stations and stations in certain regions of special interest (Figure 1), divided into ~40 sub-networks. Any individual sub-network has at least 3-6 overlapping stations with its immediate neighboring sub-network, in order to provide the necessary ties within a common reference frame in the process of combining the sub-networks using the GLOBK software (Figure 4).

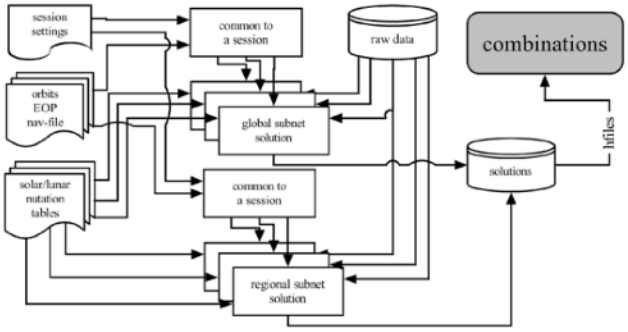

Figure 4. Distributed sub-network GAMIT processing performed at SIO.

GAMIT solutions are iterated. That is, a pre-fit solution is followed by a post-fit solution to refine the modeling errors by taking advantage of post-fit residuals. In this process, a set of elevation-dependent functions, based on actual observations, are constructed on a site-by-site basis to down-weight noisier data at lower elevations.

Analysis strategy and physical models

1. Solid Earth tides (IERS 2010 convention (*Petit and Luzum*, 2010)
2. Ocean tidal loading (FES04 model with center of mass correction) (Agnew, 2012)
3. Pole tide (IERS 2010 convention)
4. Satellite yaw model (GYM95 (*Bar-Sever*, 1996))
5. VMF1 tropospheric mapping function (*Boehm et al.*, 2006) for hydrostatic and wet components of the troposphere
6. 2nd and 3rd order ionospheric correction using the IGS AC published IONEX model

7. Absolute IGS phase center maps for station and satellite antennas (https://files.igs.org/pub/station/general/antenna_README.pdf)
8. General relativity effects (IERS 2010 convention)
9. IGS differential code bias (DCB, *Wang et al., 2016*)
10. BERN 15-parameter solar radiation model (*Springer et al.,* 1999)
11. JPL Small-Body Database (https://ssd.jpl.nasa.gov/tools/sbdb_lookup.html#/) for solar and lunar effects and nutation.

Atmospheric tidal loading model in GAMIT is currently not applied. The first-order ionospheric effects and the satellite and receiver clock errors are eliminated through double differencing of the GPS observations (*Dong and Bock,* 1989). The elevation cutoff is set to 10° while automatic data cleaning uses all data regardless of their elevation. The atmospheric tidal loading model in GAMIT is currently not applied.

A priori information and constraints

The a priori parameters include IGS rapid orbits, IERS Bulletin A Earth orientation parameters (EOP) https://www.iers.org/IERS/EN/DataProducts/EarthOrientationData/eop.html, and station positions. The a priori positions (in the current definition of ITRF, currently ITRF2014) are taken from SOPAC's previous weekly solution, except IGS14 (IGS realization of ITRF2014, updated to iGb14) core stations whose epoch-date positions are taken as published (https://www.igs.org/wg/reference-frame/#documents). ITRF core station positions are constrained to 2-3 mm horizontally, and 5-10 mm vertically. For other reference stations, the constraints are set to 25 mm horizontally and 50-150 mm vertically. New stations are allowed to freely adjust. For orbit and radiation parameters, the constraints are 10 cm. For polar motion X and Y components, they are constrained to 3 mas (~10 cm) in position, and to 0.1 mas/day in rate. For UT1-UTC, the constraints are set to 0.02 ms in epoch, 0.1 ms/day in rate. The tropospheric zenith delays are constrained to 0.5 m within each estimation interval (hourly), and their variations are constrained to 10 cm between intervals with correlation time set to 100 hours.

During per station modeling and automatic data cleaning, GAMIT uses all observations at the specified sampling interval, currently 30 s. To save computational time, at the stage of solving the normal equations, the pre-fit solution only uses every 10^{th} double-difference observable epoch (=300 s sampling interval). The post-fit solution uses every 4^{th} epoch (=120 s sampling interval).

Solutions and estimated parameters

1. Satellite orbits (3 XYZ positions and 3 XYZ velocities plus 9 radiation parameters (*Springer et al., 1999)* 24 hourly)
2. Earth orientation parameters (EOP) (24 hourly)
3. Station positions (24 hourly)
4. Tropospheric zenith delay parameters (hourly)

5. Tropospheric delay gradients (12-hourly in north-south and east-west directions)
6. L1 and L2 phase ambiguities

Four-step GAMIT solution

1. Coordinates and orbits constrained, phase ambiguities are free.
2. Coordinates and orbits constrained, phase ambiguities are fixed to integer values.
3. Coordinates and orbits loosely constrained, phase ambiguities are free.
4. Coordinates and orbits loosely constrained, phase ambiguities are fixed to integer values.

The estimated parameters and the full covariance matrices of step 4 for each of the individual sub-networks is saved into a set of GAMIT solution files (h-files) as the quasi observations for further processing for the SOPAC and combined raw displacement time series. The loosely-constrained daily sub-network GAMIT h-files are located at http://garner.ucsd.edu/pub/solutions/regional & http://garner.ucsd.edu/pub/solutions/global/.

GLOBK adjustment for SOPAC raw time series

The daily sub-network GAMIT h-files are combined weekly with GLOBK, tightly constrained to IGS14/ITRF14 (updated to iGb2014 – section 2.1.4). The output .org files (e.g., gk2110_pos.org) are located at http://garner.ucsd.edu/pub/combinations/ sorted by GPS week. The XYZ values and their 3x3 covariance matrices (corresponding to three sigma values and three correlations) are uploaded to the SOPAC database, extracted and converted to NEU displacements, sigma values and correlations (section 2.14). The reference epoch is chosen as the date of the first deployment of receiver/antenna at a station, as stored in the SOPAC database and extracted from IGS station log files.

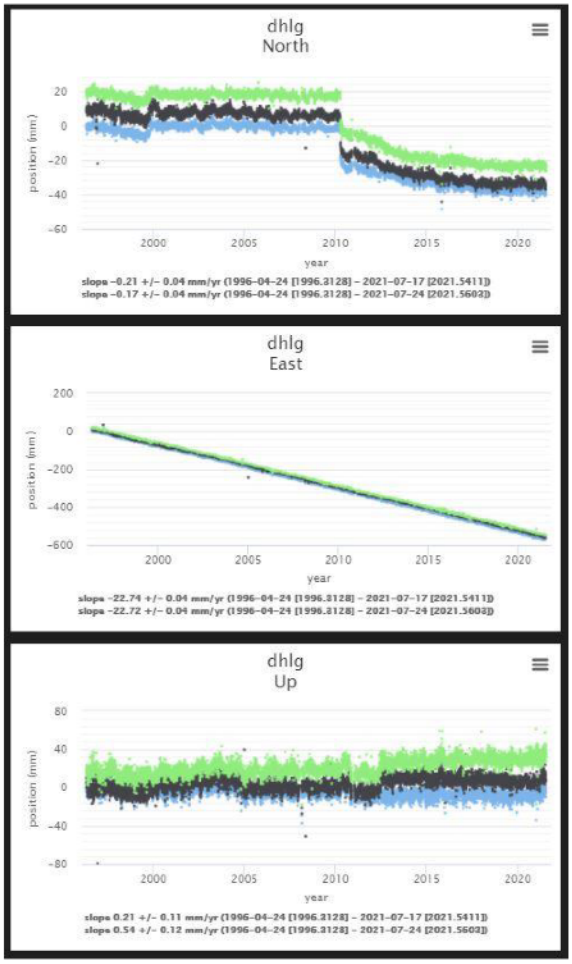

Figure 5. Combination (turquoise), JPL (black) and SIO (green) daily raw NEU displacement time series for station DHLG near the Salton Sea showing the long-term trend due to tectonic motion, punctuated by two earthquakes – the 1999 Mw7.2 Hector Mine and 2010 Mw7.2 El Mayor-Cucapah earthquakes with coseismic and postseismic deformation.

The daily NEU values make up the Level 1 SOPAC "raw" displacement time series, available in "trended" and "detrended" versions (section 2.2). (Figure 5)

The h-files are input to the (JPL/SIO) GLOBK combination along with the loosely-constrained GipsyX STACOV files, as described in section 2.1.3 (Figure 5). [However, we now use the weighted mean approach for our "official" combination solutions].

2.1.3 Combination Analysis

Definition: Daily displacement time series of continuous GNSS stations based on the combined solutions from the JPL and SOPAC analysis centers.

The primary ESDR for the project and the basis for further ESDRs is an optimal combination of the JPL STACOV files and SOPAC h-files into a single set of daily displacements that are intended/assumed to be more precise than the individual and independent JPL and SOPAC solutions described in sections 2.1.1 and 2.1.2. Although JPL and SOPAC use different GNSS software and processing strategies, they both use the identical metadata from the SOPAC archive and the same set of a priori station positions for the GipsyX and GAMIT analyses.

We have considered two strategies for estimating the combined time series:

(1) Use a weighted mean algorithm to combine the post-ATS SOPAC and JPL Raw_M XYZ time series (cleaned of outliers and non-coseismic offsets – section 2.1.9) (Figure 6). Since both sets of time series are with respect to the latest version of ITRF/IGS14 (updated to ITRF2014/iGb14 – section 2.1.4) the assumption is that it is valid to take their weighted mean without applying transformation parameters between the JPL and SOPAC time series. The algorithm is performed on a station-by-station basis, assuming that there are no correlations between stations but using the variance-covariance matrices for each solution. We take into account temporal correlations (colored noise) in assigning uncertainties. We believe that this approach is also useful in identifying single- to multiple-epoch outliers for each station. It is also very efficient. The weighted mean algorithm is given in Appendix A.3.

(2) Use the GLOBK software described in section 2.1.2 for the SOPAC time series but instead use the software to combine both the loosely-constrained JPL (section 2.1) and SOPAC (section 2.2) time series. This combination approach applies a Kalman filter using the full variance-covariance matrices, estimating transformation parameters between the two solutions with respect to ITRF/IGS14 (updated to ITRF2014/iGb14) (section 2.1.4).

In late 2021, we adopted the weighted mean combination for our published combination solutions after transitioning from the st_filter software. It is referred to as the "comb" solution. The GLOBK combination is still performed as a comparison and can be viewed in MGViz (section 10.2), http://mgviz.ucsd.edu/?mission=ESESES.

In both cases, the XYZ values are transformed into NEU displacements using the transformed geodetic coordinates of the first epoch of RINEX data in the SOPAC archive (Figure 6) rather than the date of the first receiver and antenna installation as recorded in the IGS station log files and entered into the SOPAC database. This is done to address the problem when we haven't processed the earlier data from a station that is in the process of being backfilled in preparation for reprocessing by JPL and SOPAC.

The daily NEU values make up the Level 1 "raw" (weighted mean) combination displacement time series, available in "trended" and "detrended" versions (section 2.2).

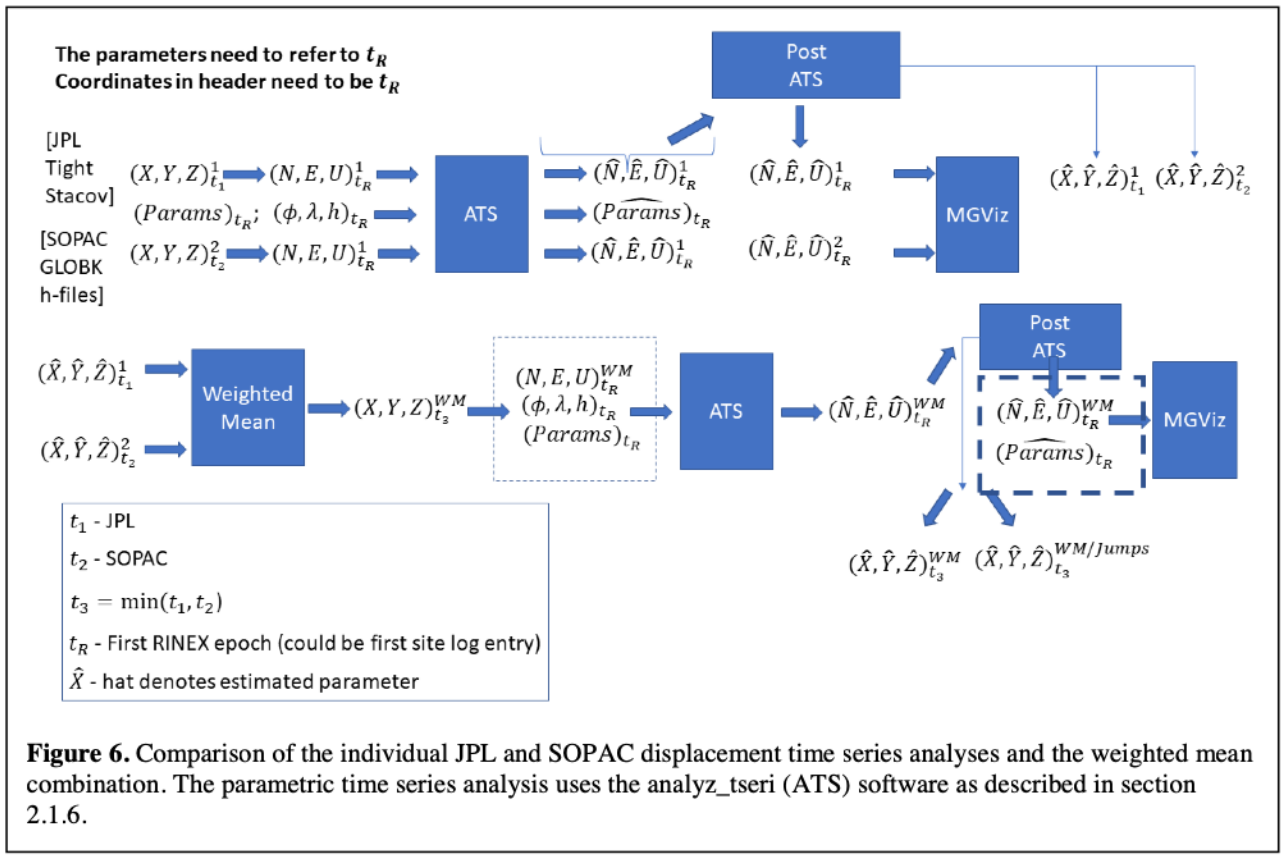

Figure 6. Comparison of the individual JPL and SOPAC displacement time series analyses and the weighted mean combination. The parametric time series analysis uses the analyz_tseri (ATS) software as described in section 2.1.6.

2.1.4 Coordinate systems

The JPL and SOPAC analyses provide daily station position estimates (X, Y, Z) in a global Earth-fixed, Earth-centered terrestrial reference frame (the latest being the iGb14 (updated from IGS14 - (https://www.igs.org/wg/reference-frame/#documents) realization of ITRF2014 (https://itrf.ensg.ign.fr/ITRF_solutions/2014/ – Altamimi et al. (2016)) and their covariance matrices collected in STACOV (GIPSY) and h-files (GAMIT), respectively. We transform these coordinates into more intuitive and physically meaningful horizontal and vertical displacements $(\Delta N, \Delta E, \Delta U)$ at epoch t_i with respect to station positions (X_0, Y_0, Z_0) at an initial epoch t_0, according to:

$$\begin{bmatrix}\Delta N\\ \Delta E\\ \Delta U\end{bmatrix}_{t_i} = \begin{bmatrix}-sin\phi cos\lambda & -sin\lambda sin\phi & cos\phi\\ -sin\lambda & \cos\lambda & 0\\ cos\lambda cos\phi & cos\phi sin\lambda & sin\phi\end{bmatrix}_{t_0} \left\{ \begin{bmatrix}X\\ Y\\ Z\end{bmatrix}_{t_i} - \begin{bmatrix}X\\ Y\\ Z\end{bmatrix}_{t_0} \right\}$$

$$= G \left\{ \begin{bmatrix}X\\ Y\\ Z\end{bmatrix}_{t_i} - \begin{bmatrix}X\\ Y\\ Z\end{bmatrix}_{t_0} \right\} \quad (1)$$

The relationship between "geodetic" coordinates (ϕ, λ, h), (ellipsoidal latitude, longitude and height) and spatial (X, Y, Z) coordinates is

$$\begin{bmatrix}X\\ Y\\ Z\end{bmatrix} = \begin{bmatrix}(\eta + h)\cos\phi\cos\lambda\\ (\eta + h)\cos\phi\sin\lambda\\ [\eta(1-e^2)+h]\sin\phi\end{bmatrix}; \eta = a/(1-e^2\sin\phi)^{1/2}; e^2 = 2f - f^2 \quad (2)$$

with semimajor axis a, inverse flattening ($1/f$), and e the ellipsoidal eccentricity. The parameters used in the transformation are the WGS84 values: a=6378137 and 1/f=298.257223563. The initial epoch $t_0$refers to the first daily position and is in general different for each station.

Given the covariance matrix $\boldsymbol{C}_{X,Y,Z}$ from the GPS position analysis,

$$\boldsymbol{C}_{X,Y,Z} = \begin{bmatrix}\sigma_X^2 & \sigma_{XY} & \sigma_{XZ}\\ \sigma_{XY} & \sigma_Y^2 & \sigma_{YZ}\\ \sigma_{XZ} & \sigma_{YZ} & \sigma_Z^2\end{bmatrix} \quad (3)$$

the propagation to the covariance matrix in the local frame at epoch t is given by

$$\boldsymbol{C}_{\Delta N,\Delta E,\Delta U} = \begin{bmatrix}\sigma_{\Delta N}^2 & \sigma_{\Delta N\Delta E} & \sigma_{\Delta N\Delta U}\\ \sigma_{\Delta N\Delta E} & \sigma_{\Delta E}^2 & \sigma_{\Delta E\Delta U}\\ \sigma_{\Delta N\Delta U} & \sigma_{\Delta E\Delta U} & \sigma_{\Delta U}^2\end{bmatrix} = \boldsymbol{G}\boldsymbol{C}_{X,Y,Z}\boldsymbol{G}^{\boldsymbol{T}}. \quad (4)$$

2.1.5 Offsets in Displacement Time Series

The daily displacement time series may contain various offsets due to either geophysical sources (i.e., earthquake rupture – coseismic displacements) or non-coseismic sources (e.g., antenna height

changes, metadata errors, changes to unlike antennas, phase center modeling errors, reference frame inconsistencies between the two analysis centers). Most of the non-geophysical offsets are due to changes in the type of antenna. Although both analysis centers use absolute antenna phase center models provided by the IGS, there still are residual offsets due to imperfections in the antenna production and calibrations (manifested mostly in the horizontal components). Other than possible reference frame inconsistencies (for example, an update from ITRF2008 to ITRF2014, which are initiated by either SOPAC and/or JPL at different times, in principle, all other offsets should be present in both solutions). In all cases, non-coseismic offsets are considered to apply to both horizontal and vertical components. The complete set of identified offsets (from SOPAC and JPL time series – section 2.1.6) are carried over to the combination time series (section 2.1.3), where additional offsets may become apparent through, for example, visual inspection of the affected time series.

The dates of the non-coseismic offsets are derived from IGS-type station log files when a change is detected (this information is incorporated into the database) and the dates of the coseismic offsets from earthquake catalogs (e.g., from the USGS). An antenna and/or receiver change may or may not result in a significant offset. Occasionally, the cause of an offset may be unknown. It is the responsibility of the time series administrator to identify significant offsets and assign new offset parameters. A pernicious problem are metadata changes that are not incorporated into the database in a timely fashion, that is, after the GAMIT and/or GipsyX analysis. In this case, additional offsets may be required. Infrequent and costly reruns of the entire data holdings, motivated by the change in the ITRF definition, will allow these offsets to be retroactively estimated.

The complete list of assigned coseismic parameters and estimates, updated weekly, can be found at http://garner.ucsd.edu/pub/measuresESESES_products/CoseismicOffsets/).

2.1.6 Time Series Analysis

The position estimates (XYZ) and their variance-covariance matrices are output as ITRF-constrained STACOV files from the Gipsy-X analysis (section 2.1.1) and the GLOBK output (constrained adjustment of the GAMIT subnetwork h-files) (section 2.1.2) from which the Level 1 JPL and SOPAC displacement time series are derived (section 2.2). The JPL and SOPAC XYZ solutions are converted to displacements in an NEU system using the WGS84 ellipsoid parameters and the epoch (t_0) as the reference epoch (section 2.1.4). The reference epoch is chosen as the earliest RINEX file stored in the SOPAC database and extracted from IGS station log files. For each station, the 3x3 block diagonal elements (represented by 6 elements based on the symmetry of the covariance matrices) are retained for each station's NEU displacements after transformation from global (X, Y, Z) coordinates (equation 1). We can neglect the cross-correlations between stations based of the analysis of Zhang (1996) who shows that their values are insignificant. Furthermore, the NEU correlations are small (<0.1) (not the XYZ correlations) and it is justified to perform a parametric time series analysis, separately for each component.

An individual component time series (ΔN, ΔE, or ΔU) at discrete epochs t_i can be modeled as

$$y(t_i) = a + bt_i + csin(2\pi t_i) + dcos(2\pi t_i) + esin(4\pi t_i) + fcos(4\pi t_i) +$$
$$+\sum_{j=1}^{n_g} g_j H\left(t_i - T_{g_j}\right) + \sum_{j=1}^{n_h} h_j H\left(t_i - T_{h_j}\right) t_i +$$
$$+\sum_{j=1}^{n_k} k_j (1 - e^{\left[-\left(\frac{t_i - T_{k_j}}{\tau_j}\right)\right]}) H\left(t_i - T_{k_j}\right) + \varepsilon_i \quad (12)$$

where H denotes the discrete Heaviside function,

$$H = \begin{Bmatrix} 0, & t_i - T_{k_j} < 0 \\ 1, & t_i - T_{k_j} \geq 0 \end{Bmatrix}$$

The coefficient a is the value at the initial epoch t_0 and t_i denotes the time elapsed from t_0 in units of years. The linear rate (slope) b represents the interseismic secular tectonic motion, typically expressed in mm/yr. The coefficients c, d, e, and f denote unmodeled annual and semi-annual variations present in GPS position time series. Annual and semiannual terms are estimated when enough data (12 months for velocity and seasonal terms) have been collected. Amplitude and phase of annual and semiannual signals are expressed according to the sine convention $A*\sin(\omega(t-t_Y)+\varphi)$, where t_Y is January 1. The magnitudes g of n_g offsets (jumps, steps, discontinuities) are due to coseismic deformation and/or non-coseismic changes at epochs T_g (section 2.5). Possible n_h changes in velocity are denoted by new velocity values h at epochs T_h. Coefficients k are for n_k postseismic deformation starting at epochs T_k and decaying exponentially with a time constant τ_j. The "logarithmic" model is another parameterization associated with afterslip on the fault surface; th18xponentntial model is associated with motion below the crust (mantle) (Wang et al. 2012a). The logarithmic model is expressed as

$$\sum_{j=1}^{n_k} k_j log\left(1 + \frac{t_i - T_{k_j}}{\tau_j}\right) H\left(t_i - T_{k_j}\right) \quad (13)$$

and was applied, for example, to 2004 Mw6.0 Parkfield, California earthquake (Freed 2007).

The event times T (g, h, k) can be determined from earthquake catalogs, site logs, automatic detection algorithms, or by visual inspection. The postseismic decay times τ_j are typically estimated separately by maximum likelihood methods, so that estimation of the remaining time series coefficients can be expressed as a linear inverse problem.

$$\boldsymbol{y} = \boldsymbol{A}\boldsymbol{x} + \boldsymbol{\varepsilon};\ E\{\boldsymbol{\varepsilon}\} = \boldsymbol{0};\ D\{\boldsymbol{\varepsilon}\} = \sigma_0^2 \boldsymbol{C}_{\boldsymbol{\varepsilon}} \quad (14)$$

where **A** is the design matrix and $\boldsymbol{x}$ is the parameter vector,

$$\boldsymbol{x} = (a\ b\ c\ d\ e\ f\ \boldsymbol{g}\ \boldsymbol{h}\ \boldsymbol{k})^T. \quad (15)$$

E denotes statistical expectation, D denotes statistical dispersion, $\boldsymbol{C}_{\boldsymbol{\varepsilon}}$ is the covariance matrix of observation errors, $\mathbf{P} = \boldsymbol{C}_{\varepsilon}^{-1}$ is the weight matrix, and σ_0^2 is an *a priori* variance factor. The output

from the adjustment are the modeled daily displacement series, the model parameters and their uncertainties. An examination of the postfit residuals $\hat{\boldsymbol{\varepsilon}} = \boldsymbol{y} - \boldsymbol{A}\hat{\boldsymbol{x}}$ are important to identify deviations from the parametric model, including any physical transients, and mismodeling.

The time series analysis is performed by JPL's analyz_tseri (ATS) software (https://qoca.jpl.nasa.gov/advclass/tsa_intro.html) for the individual JPL and SOPAC time series and for the combination (section 2.2).

Other parameters can be estimated in the ATS adjustment but have not been generally applied. For example, a local polynomial is available to model local environmental changes due to groundwater extraction in California's Central Valley or geophysical activity such as magmatic swelling of the Long Valley Caldera (Figure 7).

A tutorial for the ATS process can be found at https://qoca.jpl.nasa.gov/advclass/tsa_intro.html; https://qoca.jpl.nasa.gov/tutor_base.html).

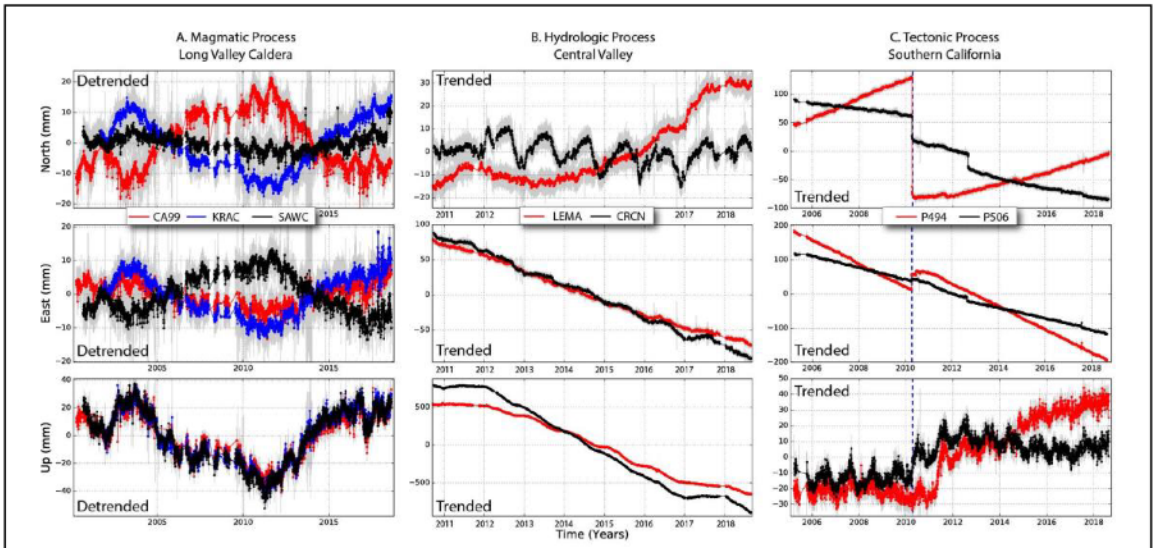

Figure 7. Examples of daily displacement time series exhibiting tectonic and non-tectonic phenomena. A) Long Valley Caldera in three equi-angle directions; B) Central Valley; C) Southern California (the 2010 Mw7.2 El Mayor-Cucapah earthquake is denoted by the dashed blue vertical line). The Long Valley Caldera components have been detrended by the long-term velocity *b*; other time series are shown trended. Source: (Klein et al. 2019).

2.1.7 Regionally-filtered time series (PCA)

Examination of the post-fit residuals $\hat{\boldsymbol{\varepsilon}} = \boldsymbol{y} - \boldsymbol{A}\hat{\boldsymbol{x}}$ from the least squares adjustment often reveals common signatures within a geographical region (e.g., Western U.S.), indicating a larger-scale source. Spatio-temporal filtering of the residuals can be used to estimate and remove the "common-mode error (CME)" allowing for improved discernment of tectonic signals. An early study

suggested a simple stacking procedure (Wdowinski et al. 1997), a simple form of principal component analysis (PCA).

PCA is used to perform spatio-temporal regional filtering as described in Dong et al. (2006). Currently, PCA is only performed for the western North America (WNAM) stations. We are also considering a focused filter on other regional sub-networks. The PCA analysis generates both the major principal component time series, as well as the spatial responses of each station for the major principal components. The advantage of the PCA method compared to the traditional removal of the CME calculated using the stacking method is the elimination of the implicit assumption of uniform CME across the network. Furthermore, PCA identifies the modes of 3D motion common to all sites and allows for spatial weighting of the CME. After the CME estimates are subtracted, the same time series estimation process described in the previous section is repeated.

It is important to note that the effect of PCA is to reduce the noise (rms) of the displacement time series so that signals of interest are more recognizable. It does not eliminate the signals of interest, e.g., postseismic deformation, episodic tremor and slip (ETS – section 7). In addition, a subset of stations may be excluded from the PCA analysis because of the presence of unmodeled effects (e.g., magmatic motion at Long Valley caldera). . We maintain a list of stations whose time series are used in the PCA process. However, the results of the PCA are applied to all WNAM time series. Currently, we only apply the first principal component.

The PCA process is as follows (Dong et al. 2006). The post-fit residuals are stored column-wise in a matrix **X** according to the displacement components in north, east and up directions for epoch m (m=1, M) and station n (n=1, N) assuming $m>n$ (this is always the case in geodetic analysis). The "covariance" matrix is defined by

$$\boldsymbol{B} = \frac{1}{M-1}\boldsymbol{X}^T\boldsymbol{X}, \tag{16}$$

which is decomposed by

$$\boldsymbol{B} = \boldsymbol{V}\boldsymbol{\Lambda}\boldsymbol{V}^T. \tag{17}$$

B is a full rank matrix of dimension N, **V** is the eigenvector matrix and **Λ** has k non-zero eigenvalues along its diagonal ($N \geq k$). Then, using **V** as an orthonormal basis at epoch i

$$X(t_i, x_n) = \sum_{k=1}^{N} a_k(t_i)v_k(x_m) \tag{18}$$

$$a_k(t_i) = \sum_{n=1}^{N} X(t_i, x_j)v_k(x_n) \tag{19}$$

The eigenvalue $a_k(t_i)$ is the kth principal component representing the temporal variations and $v_k(x_n)$ is the corresponding eigenvector representing the spatial responses to the principal components. The largest principal component corresponds to the primary contributor to the

variance of the network-wide residual time series, while the smallest principal component has the least contribution.

The daily NEU displacements resulting from PCA make up the Level 2 "WNAM_Filter" time series, available in "trended" and "detrended" versions (section 2.2).

2.1.8 Residuals

The post-fit "residuals" $\hat{\boldsymbol{\varepsilon}} = \boldsymbol{y} - \boldsymbol{A}\hat{\boldsymbol{x}}$ from the time series analysis (ATS) are differences between the observed and (parametrically) modeled time series parameters and indicate how well the model fits the data. The residual time series are not subject to the post-ATS step (section 2.1.9). There are residual time series for the cleaned and filtered time series. They are detrended by definition since the slope is one of the estimated parameters.

The daily NEU residuals from the JPL, SOPAC and Combination ATS processes make up the "Clean_ResidNeu" time series (section 2.2).

2.1.9 Post-ATS Analysis

In Year 3 of the project, we introduced an improved set of displacement time series products derived from the SOPAC, JPL and combination ATS solutions. Using "Post-ATS" Python scripts we remove the outliers detected in the ATS process, correct for the non-coseismic offsets and reinsert any coseismic offsets. All level 2 displacement time series are subject to the post-ATS procedure. The ATS and post-ATS processes are compared in Figure 6. Thus, they reflect our best estimate of the actual physical motions of the stations that have been calibrated, validated and verified, as desribed in section 2.10.

After the post-ATS process, we create a "modified raw" time series that are not parametrically modeled but are corrected for non-coseismic offsets, estimated during the ATS process, and outliers. This allows researchers to directly use these time series for further analysis and modeling without laborious quality control. We refer to these as "Raw_M" time series (Figure 6). They include:

Detrended NEU time series: **WNAM_Raw_M_DetrendNeu & GLB_Raw_M_DetrendNeu**

Detrended NEU time series: **WNAM_Raw_M_TrendNeu & GLB_Raw_M_TrendNeu**

Trended XYZ positions: **WNAM_Raw_M_TrendXYZ & GLB_Raw_M_TrendXYZ**

Trended XYZ positions **WNAM_RawJumps_TrendXYZ** & **GLB_RawJumps_TrendXYZ** with both non-coseismic and coseismic offsets intact, with outliers removed.

Note: The RawJumpsXYZ time series have been created by request for the Crustal Motion Model (CMM) (http://scecinfo.usc.edu/resources/data/index.html) developed under the aegis of the Southern California Earthquake Center (SCEC). This allows our time series to be compatible with other community time series.

The residual time series (section 2.1.8) are not subject to the post-ATS step.

2.1.10 Parameter uncertainties

In converting from (X,Y,Z) coordinates to (N,E,U) displacements and the propagation of errors, we assume that the coordinates are uncorrelated (Zhang, 1996). We extract the along-diagonal 3x3 (X,Y,Z) covariance matrix (from the full STACOV or GLOBK covariance matrices) to propagate the 3x3 (N,E,U) covariance matrix (section 2.1.4) for each station. The correlations between the (N,E,U) displacements are small (~0.1-0.2; the XYZ correlations are ~0.8) so we can perform the time series analysis component-by-component.

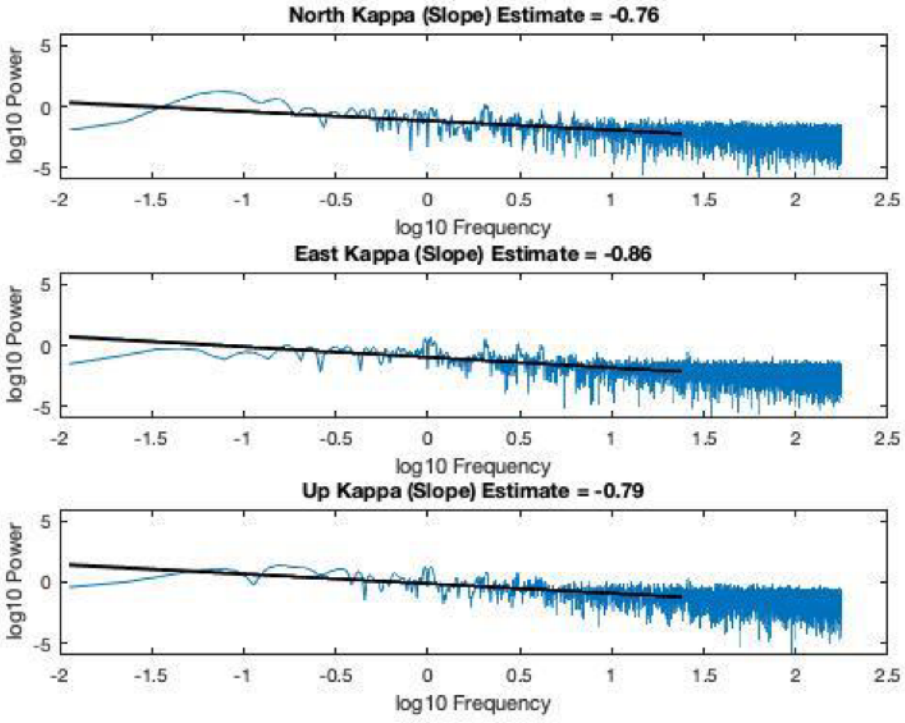

Figure 8. We estimate a best-fit line to the computed power and frequency in log-log space, to obtain the slope (spectral index, κ), and the best-fit y-intercept value (b). Frequencies greater than log10(1/15) days are excluded to avoid having the white noise bias the colored noise components..

We use a weighted least squares analysis of the 1-D displacement vector $\boldsymbol{y}$ to estimate the vector of the parameters $\boldsymbol{x}$ with the following formulation,

$$\boldsymbol{y} = \boldsymbol{A}\boldsymbol{x} + \boldsymbol{\varepsilon};\ E\{\boldsymbol{\varepsilon}\} = \boldsymbol{0};\ D\{\boldsymbol{\varepsilon}\} = \sigma_0^2 \boldsymbol{C}_{\boldsymbol{\varepsilon}} \tag{14}$$

where $\boldsymbol{A}$ is the design matrix. The error $\boldsymbol{\varepsilon}$ is assumed to be unbiased with unscaled covariance matrix $\boldsymbol{C}_{\boldsymbol{\varepsilon}}$. It is well known that assuming only white noise (a diagonal $\boldsymbol{C}_{\boldsymbol{\varepsilon}}$) yields unrealistically-low uncertainties for the estimated parameters, which then propagates to overly optimistic uncertainties in higher-level products and when input to geophysical models. White noise can also

be expressed as the "one-sigma" uncertainty of a single daily displacement (north, east or up). There is also a temporally-correlated "colored noise" component that needs to be considered in constructing $\boldsymbol{C_\varepsilon}$. Studies have investigated different colored noise processes including flicker noise, random walk, a combination of flicker and random walk, power law noise, first-order Gauss-Markov plus random walk noise; and power law plus broadband, seasonal noise (Langbein, 2008). We assume a power law noise function according to Williams (2003) and express the covariance matrix as the sum of a time-independent "white noise" matrix and a time-dependent "colored noise" matrix such that,

$$\boldsymbol{C_\varepsilon}(t) = a^2\boldsymbol{I} + b^2\boldsymbol{J_\kappa}(t)$$

Coefficients a and b are the magnitudes of white noise and colored noise, respectively, and $\boldsymbol{\kappa}$ is the spectral index. The index does not need to be an integer. Special cases include white noise with spectral index = 0, flicker noise = -1 and random walk noise = -2. We estimate b and κ through spectral analysis of the residual displacements to construct $\boldsymbol{C_\varepsilon}$, as described in Appendix A.3 (Figure 8).

2.1.11 Calibration, Validation and Verification

Calibration is the process of discovering biases and scale factors in a method of processing instrument data and correcting the data for these factors. **Validation** ensures that a system satisfies the stated functional intent of the system and the requirements of a project. **Verification** ensures the correct operation of a process according to its stated operating specifications.

Calibration

Level 2 consists of calibrated and validated Level 0-1 products that then provide the basis for higher order products (Figure 2), including the following:

(1) Level 0: Accuracy and timeliness of metadata, in particular changes in antenna model and height. Metadata are gathered through collection of IGS-type station log files and ingested into the database. Late and/or inaccurate metadata will propagate into the ESDRs and introduce spurious offsets into the displacement time series, as well as loss of precision. This requires setting an offset parameter in the time series analysis. The offset can be removed after a re-processing of the GNSS data.

(2) Level 0: Completeness and timeliness of station RINEX data. RINEX data that do not arrive on time cause gaps in the time series and disruptions in the production of ESDRs. However, missing data can be back-filled prior to re-processing of the entire data holdings.

(3) Detection of outliers in the ATS process (Table 2). Individual criteria can be specified for each station, as needed:

weak_obs (big sigma) criteria (mm): based on the formal errors.
If at one epoch the formal sigma values of one site are bigger than the specified criteria, the solution of this site at this epoch will be ignored. The order is East, North, Up.

outlier (big o-c) criteria (mm): based on the postfit residuals.

If at one epoch the residuals of one site are bigger than the specified criteria, the solution of this site at this epoch will be ignored. This command prevents outliers from contaminating the time series analysis results. The order is East, North, Up.

very bad_obs criteria (mm): based on gross outlier threshold.

If the data have gross outliers the initial adjustments will be biased. They are removed before the adjustment. The order is East, North, Up.

Table 2. Default values from the analyze_tseri (ATS) driver file

Criteria	East(mm)	North(mm)	Up(mm)
weak_obs (big sigma)	40.	40.	80.
outlier (big o-c)	25.	25.	35.
very bad_obs	1000.	1000.	3000.

Further detection of data outliers occurs through visual inspection, which are flagged during any of the different product levels, for example, by anomalies in the displacement grids (section 5). Outliers are removed from all ESDRs, except _RAW data (section 2.2). We maintain a Google document called "omit_span" where outliers are recorded and removed in subsequent ATS analyses:

https://docs.google.com/spreadsheets/d/1lp6dZSycCT1by7xxbO1b6H_D-1L29Ep5/edit#gid=213666945 (**Not publicly available – available on request)**

(4) The GAMIT and GIPSY analyses that produce the Level 1 SOPAC and JPL raw time series are seeded with a-priori station coordinates derived from the latest weekly ATS processes (preferably the cleaned combination solution). Gross errors in the a priori coordinates can adversely affect the analyses and result in gaps in the time series. The a priori coordinates are entered by JPL and SOPAC through parallel processes that extract the information from the SOPAC database. JPL uses station XML files, while SOPAC uses a flat file generated from the SOPAC database. These need to checked periodically to ensure that they are indeed equivalent.

(5) Large adjustments from the a priori coordinates are flagged on a weekly basis for review by the time series administrator. These can be due to geophysical signals (e.g., coseismic displacements), inaccurate metadata or problems in the GNSS analyses.

(6) The latest estimated velocities (section 4) estimated by JPL and SOPAC are regularly compared to identify, understand and repair any significant differences – we focus on discrepancies greater than 5 mm/yr for stations that have more than 2.5 years of data (Figure 9). In addition, JPL identifies annual amplitude terms (section 2.1.6) that exceed a certain percentage (50% for the horizontal and 150% for the vertical).

(7) We maintain a Master List (http://geoapp02.ucsd.edu:8080/gpseDB/psite?op=showCleanList – VPN required, available on request) of stations that are processed. From time to time a station may be removed altogether based on several factors, for example, very few data points have been recorded for a defunct station (no longer operational).

(8) Interactive examination of the displacement time series is performed to identify and flag problematic time series related to the eight items above. This is performed by the time series administrator through the GPS Explorer interface that is in the process of moving to a different platform. This requires administrator privileges. The administrator is also responsible for adding new parameters for the time series analysis. For example, after an earthquake occurs coseismic offsets must be estimated for all stations that have had significant permanent (static) displacements and eventually postseismic parameters must be set. Depending on the earthquake's fault mechanism (strike-slip, thrust, normal), the time series may only require horizontal (N and E) offsets. Likewise, a limited number of stations closest to the epicenter may also require vertical offsets as was the case for the July 6, 2019 Mw7.1 Ridgecrest earthquake. When an antenna model change has been recorded in the station log files, the date is flagged and the administrator determines if has caused a significant offset in the time series. Our philosophy is to add a new model parameter only when it is required.

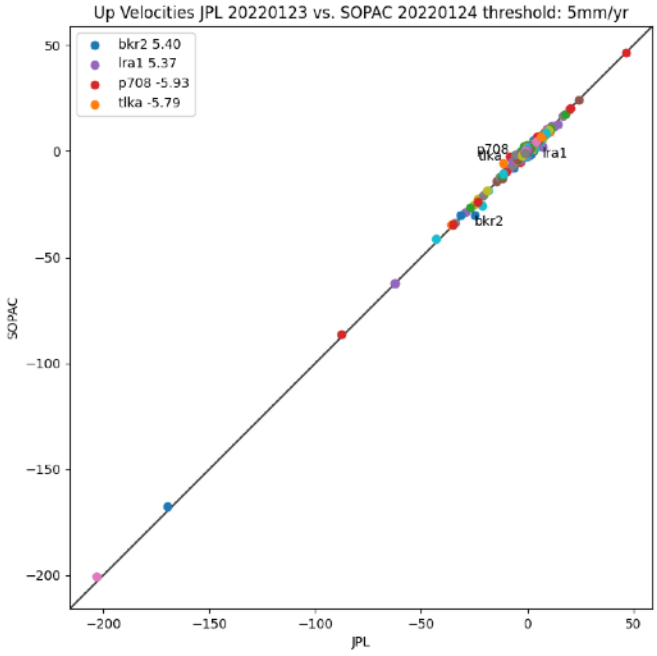

Figure 9. Comparison of SOPAC and JPL velocity estimates prepared in late January, 2022. Outliers are identified along with their velocities in mm/yr.

Validation and Verification

This document describes the elements of our ESESES system, as summarized in the flow chart of Figure 2 with the agreed upon ESDRs. Validation requires the verification of a complete and accurate transfer of these products to the project page at CDDIS (https://cddis.nasa.gov/archive/GPS_Explorer/), according to the schedule determined by the nature of the product. For example, the displacement time series tar files (section 2.2) are delivered to CDDIS once per week, while the ETS transients (section 7) are updated as ETS events occur (with an interval of about 14 months). The ESDRs are also available at the SOPAC archive–-

http://garner.ucsd.edu/pub/measuresESESES_products/ (username: anonymous; password: your e-mail address).

2. Displacement Time Series

Here we summarize the complete suite of daily displacement time series described in the previous sections. There are three overall sets including JPL ("jpl"), SOPAC ("sopac") and combined ("comb") products. Currently, the time series are divided according to stations in Western North America (WNAM) and all other geographic locations (GLB). The time series are extended weekly and a set of new tar files are created. We use two coordinate systems, XYZ and NEU (section 2.1.4). The time series are appended with seven data points each week and parametrically-fit weekly (section 2.1.6). Each week, a set of tar files are created and stored at two archives:

SOPAC:
http://garner.ucsd.edu/pub/timeseries/measures/ats/WesternNorthAmerica/
http://garner.ucsd.edu/pub/timeseries/measures/ats/Global/
CDDIS: http://cddis.nasa.gov/pub/GPS_Explorer/

Notes:

- The time series can be viewed with our interactive user interface, MGViz (section 10.2), http://mgviz.ucsd.edu/?mission=ESESES
- File headers contain estimated time series model parameters & uncertainties (sections 2.1.6, 2.1.10).
- All the time series except""Ra"" have outliers and jumps (non-coseismic offsets) removed.
- All the time series retain the coseismic offsets (values in header).
- The file headers in the "Raw_M" time series are included for documentation purposes only – they have not gone through a time series analysis but have used information (location of offsets and outliers) from the modeled cleaned time series. Outliers have been removed and non-coseismic offsets corrected.
- PCA filtering is only performed for "WNAM" time series.
- YYYYMMDD indicates the date that the tar file was created.

(1) NEU raw time series (no corresponding XYZ raw)

(e) ***Trended:*** **Western North America**

WNAM_Raw_TrendNeuTimeSeries_comb_YYYYMMDD.tar.gz
WNAM_Raw_TrendNeuTimeSeries_jpl_YYYYMMDD.tar.gz
WNAM_Raw_TrendNeuTimeSeries_sopac_YYYYMMDD.tar.gz

(b) Global

GLB_Raw_TrendNeuTimeSeries_comb_YYYYMMDD.tar
GLB_Raw_TrendNeuTimeSeries_jpl_YYYYMMDD.tar
GLB_Raw_TrendNeuTimeSeries_sopac_YYYYMMDD.tar

(2) NEU modeled ("Clean") time series

Trended:

(a) Western North America

WNAM_Clean_TrendNeuTimeSeries_comb_YYYYMMDD.tar
WNAM_Clean_TrendNeuTimeSeries_jpl_YYYYMMDD.tar
WNAM_Clean_TrendNeuTimeSeries_sopac_YYYYMMDD.tar

(b) Global

GLB_Clean_TrendNeuTimeSeries_comb_YYYYMMDD.tar.gz
GLB_Clean_TrendNeuTimeSeries_jpl_YYYYMMDD.tar.gz
GLB_Clean_TrendNeuTimeSeries_sopac_YYYYMMDD.tar.gz

Detrended:

(a) Western North America

WNAM_Clean_DetrendNeuTimeSeries_comb_YYYYMMDD.tar.gz
WNAM_Clean_DetrendNeuTimeSeries_jpl_YYYYMMDD.tar.gz
WNAM_Clean_DetrendNeuTimeSeries_sopac_YYYYMMDD.tar.gz

(b) Global

GLB_Clean_DetrendNeuTimeSeries_comb_YYYYMMDD.tar.gz
GLB_Clean_DetrendNeuTimeSeries_jpl_YYYYMMDD.tar.gz
GLB_Clean_DetrendNeuTimeSeries_sopac_YYYYMMDD.tar.gz

(3) NEU residual displacements (detrended by definition)

(a) Western North America

WNAM_Clean_ResidNeuTimeSeries_comb_YYYYMMDD.tar.gz
WNAM_Clean_ResidNeuTimeSeries_jpl_YYYYMMDD.tar.gz
WNAM_Clean_ResidNeuTimeSeries_sopac_YYYYMMDD.tar.gz

(b) Global

GLB_Clean_ResidNeuTimeSeries_comb_YYYYMMDD.tar.gz
GLB_Clean_ResidNeuTimeSeries_jpl_YYYYMMDD.tar.gz
GLB_Clean_ResidNeuTimeSeries_sopac_YYYYMMDD.tar.gz

(4) PCA-filtered displacements (WNAM only)

Trended:

WNAM_Filter_TrendNeuTimeSeries_comb_YYYYMMDD.tar.gz
WNAM_Filter_TrendNeuTimeSeries_jpl_YYYYMMDD.tar.gz
WNAM_Filter_TrendNeuTimeSeries_sopac_YYYYMMDD.tar.gz

Detrended:

WNAM_Filter_DetrendNeuTimeSeries_comb_YYYYMMDD.tar.gz
WNAM_Filter_DetrendNeuTimeSeries_jpl_YYYYMMDD.tar.gz
WNAM_Filter_DetrendNeuTimeSeries_sopac_YYYYMMDD.tar.gz

(5) NEU filtered residual displacements (detrended by definition)

WNAM_Filter_ResidNeuTimeSeries_comb_YYYYMMDD.tar.gz
WNAM_Filter_ResidNeuTimeSeries_jpl_YYYYMMDD.tar.gz
WNAM_Filter_ResidNeuTimeSeries_sopac_YYYYMMDD.tar.gz

(6) NEU raw-modified (Raw_M) time series

Trended:

(a) Western North America

WNAM_Raw_M_TrendNeuTimeSeries_comb_YYYYMMDD.tar.gz
WNAM_Raw_M_TrendNeuTimeSeries_jpl_YYYYMMDD.tar.gz
WNAM_Raw_M_TrendNeuTimeSeries_sopac_YYYYMMDD.tar.gz

(b) Global

Global_Raw_M_TrendNeuTimeSeries_comb_YYYYMMDD.tar.gz
Global_Raw_M_TrendNeuTimeSeries_jpl_YYYYMMDD.tar.gz
Global_Raw_M_TrendNeuTimeSeries_sopac_YYYYMMDD.tar.gz

Detrended:

(a) Western North America

WNAM_Raw_M_DetrendNeuTimeSeries_comb_YYYYMMDD.tar.gz
WNAM_Raw_M_DetrendNeuTimeSeries_jpl_YYYYMMDD.tar.gz
WNAM_Raw_M_DetrendNeuTimeSeries_sopac_YYYYMMDD.tar.gz

(b) Global

GLB_Raw_M_DetrendNeuTimeSeries_comb_YYYYMMDD.tar.gz
GLB_Raw_M_DetrendNeuTimeSeries_jpl_YYYYMMDD.tar.gz
GLB_Raw_M_DetrendNeuTimeSeries_sopac_YYYYMMDD.tar.gz

(7) ITRF2014 XYZ displacements

Raw time series – coseismic and non-coseismic offsets uncorrected, outliers removed

(a) Western North America

WNAM_RawJumps_TrendXYZTimeSeries_comb_YYYYMMDD.tar.gz
WNAM_RawJumps_TrendXYZTimeSeries_jpl_YYYYMMDD.tar.gz
WNAM_RawJumps_TrendXYZTimeSeries_sopac_YYYYMMDD.tar.gz

(b) Global

GLB_RawJumps_TrendXYZTimeSeries__YYYYMMDD.tar.gz
GLB_RawJumps_TrendXYZTimeSeries_jpl_YYYYMMDD.tar.gz
GLB_RawJumps_TrendXYZTimeSeries_sopac_YYYYMMDD.tar.gz

Raw time series – non-coseismic jumps corrected, outliers removed

(a) Western North America

WNAM_Raw_M_TrendXYZTimeSeries_YYYYMMDD.tar.gz
WNAM_Raw_M_TrendXYZTimeSeries_jpl_YYYYMMDD.tar.gz
WNAM_Raw_M_TrendXYZTimeSeries_sopac_YYYYMMDD.tar.gz

(a) Global

GLB_Raw_M_TrendXYZTimeSeries_YYYYMMDD.tar.gz
GLB_Raw_M_TrendXYZTimeSeries_jpl_YYYYMMDD.tar.gz
GLB_Raw_M_TrendXYZTimeSeries_sopac_YYYYMMDD.tar.gz

3. Troposphere Delay & Precipitable Water

3.1 Method

3.1.2 Troposphere delay

As described in sections 2.1 and 2.2 (Level 1A) both JPL and SOPAC estimate troposphere parameters as part of the GIPSY/OASIS and GAMIT analysis, respectively. The total tropospheric delay (TD) observed by GPS is the integrated refractivity of the atmosphere, N, over the signal ray path

$$TD = \int_{s=raypath} N\,ds = \int_{s=raypath} (k_1 \frac{P}{T} + k_2 \frac{e}{T} + k_3 \frac{e}{T^2})ds \quad (5)$$

where P is the atmospheric pressure, T is temperature, e is water vapor partial pressure, and the k's are empirically determined physical constants in an expression for N (*Bevis et al.*, 1994). Therefore, the estimated tropospheric signal delay provides information about the unknown moisture above the station. The tropospheric delay observed for a given satellite at angle θ from vertical is modeled as *Davis et al.* (1994),

$$TD(\theta) = ZHD \times mh(\theta) + ZWD \times mw(\theta) \quad (6)$$

where ZHD is the zenith hydrostatic delay, ZWD is the zenith wet delay, and *mh* and *mw* are mapping functions that describe the variation of ZHD and ZWD with varying elevation angle. Both JPL and SOPAC currently utilize the gridded Vienna Mapping Function [VMF1 – (*Boehm et al.* 2006); (https://vmf.geo.tuwien.ac.at/trop_products/GNSS/) for a priori hydrostatic and wet troposphere delay components values and to model zenith delay variance. Use of final GPS orbits (at 7- to10-day latency) ensures the highest fidelity troposphere series for retrospective studies (Moore et al., 2016; Wang et al., 2019). Troposphere delays are estimated at 5-minute resolution by JPL and hourly by SIO. These solutions are available at https://cddis.nasa.gov/archive/GPS_Explorer/archive/trop/. The SOPAC solutions are in http://garner.ucsd.edu/pub/troposphere but have not been updated since 2011 (GPS week 1258). **The data beyond 2011 need to be extracted from the GAMIT output.**

Currently, there is no combination solution for the troposphere ESDRs.

3.1.2 Precipitable Water Vapor

With a modest investment in computation following established algorithms (e.g., Bevis et al., 1994), the zenith total delays (ZTD) necessarily estimated during the displacement time series processing with temporal resolution up to 5 min become the basis for an ESDR consisting of precipitable water vapor (PWV) time series. The conversion to PWV requires the zenith wet delay

(ZWD), obtained by subtracting from the ZTD an accurate zenith hydrostatic delay (ZHD) (Saastamoinen, 1973) as a function of surface pressure, latitude, and orthometric height. 1 hPa of pressure error implies uncertainty of 0.35mm in PWV (Nilsson and Elgered, 2008), an accuracy easily obtained by onsite barometers. PWV time series are useful for tracking extreme weather events such as monsoons (Figure 10) and atmospheric rivers that can lead to flash flooding (Moore et al., 2015; Wang et al., 2019). We produce PWV records in the SINEX_TRO2.0 Provisional format for stations with onsite meteorological measurements. The conversion from ZWD to PWV further requires a measure of mean atmospheric temperature, which can be estimated from surface temperature (Bevis, 1994) and is a lesser source of PWV error in comparison to pressure. These PWV solutions are available at https://cddis.nasa.gov/archive/GPS_Explorer/archive/trop/.

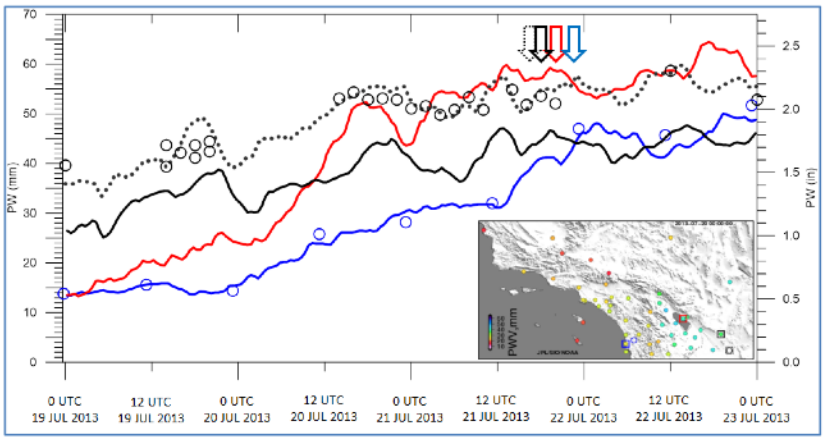

Figure 10: GPS PWV measurements were used both operationally to track a North American Monsoon event and forecast flash flooding. Circles represent PW (cm) for radiosondes at San Diego, California (blue), and Yuma, Arizona (black). Solid traces show GPS PW measurements at San Diego, California (blue), Durmid, California (red), Glamis, California (black), and Yuma, Arizona (dotted black). Arrows indicate the times of passage of an upper low at the identified GPS-Met sites. Map locates GPS stations with squares at San Diego (blue), Durmid (red), Glamis (black), and Yuma (dotted black), and radiosondes with circles at San Diego (blue) and Yuma (black). PW in mm at the GPS stations is shown, according to the color scale, at 1700 PDT 19 Jul (0000 UTC 20 Jul). Source: (Moore et al. 2015).

3.2 Nomenclature

The Level 1 ESDRs are referred to as "**Zenith Troposphere Delay (ZTD)**" time series. These ESDRs form the basis for the Level 2 "**Precipitable Water Vapor (PWV)**" time series.

Note: The trop file at CDDIS includes both ZTD and PWV (if available) values

3.3 Status

JPL 5-minute troposphere delay and PWV time series since 1992 uploaded to CDDIS and automatically updated weekly.

Need to replace GAMIT troposphere delay solutions (1-hour intervals) from ITRF2014 reprocessing completed in Year 3.

4. Level 3 Displacement Products

4.1 Description

Definition: Weekly updates of displacement products: 3-D Velocities, Coseismic

The analysis of the Level 2 displacement time series (section 2.1.6) results in Level 3 estimated parameters that represent the different phases of the crustal deformation cycle (interseismic, coseismic, postseismic). The time series also include unmodeled effects of irregular uplift and subsidence, magmatism and other transient motions that may obscure the tectonic signals. Level 4 products include transient signals related to episodic tremor and slip (ETS) (section 7) and horizontal strain-rate gids (section 8), as well as hydrological signals (section 9).

Figure 11: An example of ITRF2004 horizontal velocities estimated from the combined time series of JPL and SIO. Significant (M>6) earthquakes denoted by red circles. This is a screen shot from MGViz (section 10.2), http://mgviz.ucsd.edu/?mission=ESESES

4.2 Station Velocities

The 3-D station velocity estimates at each station (Figure 11) are a direct product of the time series analysis (section 2.1.6). The velocity is represented as the slope of the displacement time series (equation 12 – parameter *b*) where all offsets (coseismic and non-coseismic) and seasonal and postseismic effects have also been simultaneously modeled. A new velocity estimate is produced weekly for each of the solution types, the combined, JPL and SOPAC time series, both unfiltered

and filtered. Since the time series analysis is performed separately for each coordinate (NEU displacement), the 3D velocities are assumed to be uncorrelated (zero covariances).

In the ATS process, the velocity uncertainties are scaled according to Williams (2003) to take into account colored noise

$$\hat{\sigma}_b{}^2 \cong \frac{9b_k^2}{16\Delta T^2(N^2-1)}. \quad (20)$$

where n is the number of time series data points equally spaced in time, T is the total time span and $b_k$is the colored noise coefficient. **We are in the process of replacing the colored noise algorithm so that all estimated parameters can be assigned realistic uncertainties (ATS only does this for velocities). See section 2.1.10 and Appendix A3.**

The horizontal and vertical velocities and their estimates can be viewed with MGViz (section 10.2), http://mgviz.ucsd.edu/?mission=ESESES .

Station motions may not be adequately modeled by a single velocity (Figure 7). There is a provision for assigning multiple velocities but we no longer use this option since it is quite subjective. We prefer to let users examine the **Raw_M_Trend** time series and make their own choices. These time series have non-coseismic jumps corrected and outliers removed (sections 2.2)

Note: The residuals for a time series that require more than one velocity (slope) will not look intuitive since a sub-optimal model (only one velocity) was used to fit the data. Therefore, it most useful to start with the Raw_M time series.

The velocities are estimated in the ITRF (currently, ITRF2014) rather than a regional frame such as the Stable North America Reference Frame (SNARF).https://www.unavco.org/projects/past-projects/snarf/snarf.html) or a plate-fixed frame (e.g., Pacific plate). The velocities can then be transformed from ITRF to any other reference frame with the appropriate transformation parameters (e.g., plate parameters, Helmert transformation parameters). We plan to provide the option to transform the velocities to a plate-fixed frame.

Product details

A single station velocities file is created every week in parallel with the displacement time series. They are extracted from the time series file headers of the unfiltered combined weighted mean product ("comb") (section 2.2). The files are stored at:

http://garner.ucsd.edu/pub/measuresESESES_products/Velocities/

The file naming convention is:

ESESES_velocities_YYYYMMDD.txt

e.g., ESESES_velocities_20210920.txt

Older files are moved to the "previous" directory

For CDDIS the filename is

~/GPS_Explorer/archive/Velocities/ ESESES_velocities_YYYYMMDD.txt

The file header contains the information on the contents of the file. Here is an example of the header with several velocities:

NASA MEaSUREs project: Extended Solid Earth Science ESDR System (ESESES)
Station velocities and uncertainties in mm/yr
Ellipsoidal height in meters
Derived from daily displacement time series – combined product (weighted mean)
Uncertainties include the effects of colored noise in daily time series
The north, east and up velocities are assumed to be uncorrelated
Note: Stations include a minimum of 2.5 years of data
Reference:
Bock, Y., Moore, A.W., Argus, D. F., Fang, P., Jiang, S., Kedar, S., Knox, S.A. Liu, Z. & Sullivan A. (2021),
Extended Solid Earth Science ESDR System (ES3): Algorithm Theoretical Basis Document: Chapter 4.2
http://sopac-csrc.ucsd.edu/wp-content/uploads/2021/08/ESESES-ATBD.pdf

Site	Longitude	Latitude	Height	Nvel	Evel	Uvel	Nerr	Eerr	Uerr
7odm	242.906808	34.116407	762.06757	6.48	-27.31	0.92	0.11	0.16	0.25
ab01	185.795244	52.209505	25.46008	-22.73	-6.62	1.6	0.39	0.18	0.32
ab02	191.14533	52.970606	192.78532	-21.07	-7.99	1.5	0.17	0.15	0.26

4.3 Coseismic offsets

The weekly time series analysis (section 2.1.6) includes estimates of offsets (jumps, discontinuities) that can be due to sudden coseismic motions or data artifacts due to (mostly) antenna model changes, metadata errors, changes in reference frames, or unknown sources (e.g., Figure 3). The offsets are modeled as (section 2.1.6):

$$\sum_{j=1}^{n_g} g_j \, H\left(t_i - T_{g_j}\right)$$

with magnitudes g of n_g offsets (jumps, steps, discontinuities) at epochs T_g (section 2.5). In this parameterization, we do not distinguish between coseismic and "non-coseismic" offsets, however, they are selected and identified in the headers of the time series files (section 2.2). Furthermore, non-coseismic offsets are estimated and corrected in the various time series products, while the coseismic offsets are not corrected in order that the time series reflect only physical motions of the stations. A particular earthquake may cause significant coseismic offsets at hundreds of stations

for the largest earthquakes, for example, the 2019 Mw7.1 Ridgecrest earthquake displaced almost 300 stations (by >2-3 mm to about a meter) within a radius of about 300 km from its epicenter. Non-coseismic offsets mostly correlate with changes in antenna models although not all antenna changes will result in a visible offset. There have been efforts to automatically detect offsets in displacement time series using various algorithms but these are not foolproof and some user interaction is required through the administrator interface. In order to reduce the number of offset parameters, current practice is to keep track of antenna changes and then determine visually if there is a significant offset to be estimated. Although, the IGS calibrates the absolute phase centers of all available geodetic-quality antennas, these are not perfect and may leave residual offsets in the displacement time series (see also section 2.1.5). Note that coseismic offsets may only be applied to horizontal components (N.E), while non-coseismic offsets are automatically applied to all three components. Also note, for daily displacement time series the offset is usually applied to the day after the recorded date if the antenna changed or earthquake occurred after 12:00 UTC.

We are in the process of introducing a colored noise algorithm so that all estimated parameters, including the offsets, can be assigned realistic uncertainties. See section 2.1.10 and Appendix A3.

Product details

The coseismic offsets are extracted from the weighted mean combination ("comb") time series file headers (section 2.1.9). The coseismic offset files are updated weekly and stored at:

http://garner.ucsd.edu/pub/measuresESESES_products/CoseismicOffsets/

The file naming convention is:

ESESES_CoseismicOffsets_YYYYMMDD.txt (YYYYMMDD is the same as corresponding time series)

e.g., ESESES_CoseismicOffsets_20210920.txt

Older files are moved to the "previous" directory

For CDDIS the filename is

~/GPS_Explorer/archive/CoseismicOffsets/ESESES_CoseismicOffsets_YYYYMMDD.txt

The offsets are re-estimated every week so there is a new file every week to correspond to the time series products of that week. Although there may not be a new earthquake every week, sometimes we will add coseismic offsets for particular events as the time series grow, quality controlled or backfilled.

The coseismic offsets directory contains a file CoseismicOffset_EarthquakeMasterList (to be done, shortly) with a list of all the earthquakes that have been modeled in the ESESES displacement time series and sorted by date and time.

The coseismic offsets file header contains the information on the contents of the file. Here is an example of a header:

NASA MEaSUREs project: Extended Solid Earth Science ESDR System (ESESES)
Coseismic and postseismic offsets are sorted by earthquake (event)
Derived from headers of daily displacement time series – combined product (weighted mean)

Reference:
Bock, Y., Moore, A.W., Argus, D. F., Fang, K. Guns, P., Jiang, S., Kedar, S., Knox, S.A. Liu, Z. & Sullivan A. (2021),
Extended Solid Earth Science ESDR System (ES3): Algorithm Theoretical Basis Document: Section 4.3
http://garner.ucsd.edu/pub/measuresESESES_products/ATBD/ESESES-ATBD.pdf (username:anonymous; password: your e-mail address)

The estimated coseismic offsets and their uncertainties estimates can be viewed with MGViz (section 10.2), http://mgviz.ucsd.edu/?mission=ESESES

The north, east and up offsets are assumed to be uncorrelated
Station coseismic offsets and uncertainties in mm
Ellipsoidal height in meters; latitude and longitude (East) in decimal degrees
All earthquake onset times are in UTC

List of all earthquakes in ESESES daily displacement time series: CoseismicOffset_EarthquakeMasterList (sorted by date and time)

Date	YYYY-MM-DDD	Site	Latitude	Longitude	Height	Noffset	Eoffset	Uoffset	Nerr	Eerr	Uerr
1992.4904	1992-06-28	jplm	34.204818	241.826779	423.978	12.53	-4.07	19.8	1.21	0.68	4.14

5. Level 3: Displacement Fields (Grids)

5.1 Background

Definition: Automated weekly update of horizontal and vertical displacement grids

The Level 2 displacement time series provide a record of horizontal and vertical transient motions over and above secular, long-term processes such as interseismic deformation, represented by station velocities (Figure 12). The transient motions include coseismic and postseismic motions from earthquakes, magmatic deformation at Long Valley Caldera (e.g., Liu et al., 2011), subsidence in California's San Joaquin Valley (Argus et al., 2017), and episodic tremor and slip (ETS) in Cascadia (Rogers and Dragert, 2003). Transients other than coseismic and postseismic deformation are not modeled as part of the time series analysis (section 5.1). The detection of transients is important in fault slip modeling and assessing seismic risk and is the basis of the Level 4 ESDRs (section 7).

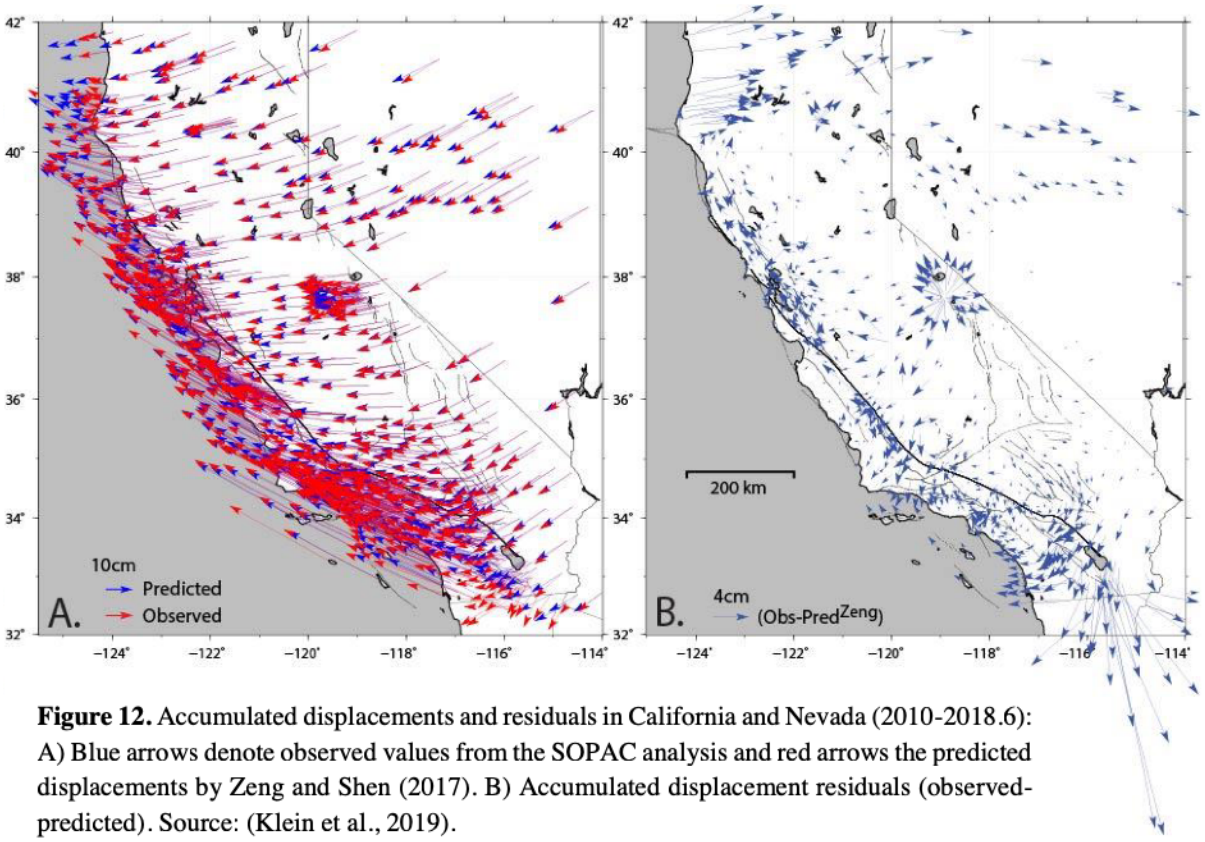

Figure 12. Accumulated displacements and residuals in California and Nevada (2010-2018.6): A) Blue arrows denote observed values from the SOPAC analysis and red arrows the predicted displacements by Zeng and Shen (2017). B) Accumulated displacement residuals (observed-predicted). Source: (Klein et al., 2019).

5.2 Methodology: Horizontal Displacement Fields

The station displacements corrected for non-coseismic offsets (section 2.1.5) are interpolated on a weekly basis to generate an updated displacement field (grid). Direct interpolation of the observed horizontal displacements is not optimal in the near-field of active geologic faults, where elastic deformation is occurring and the number and spatial distribution of stations is lacking. Therefore, we supplement our Level 2 displacements with displacements predicted by forward modeling the secular horizontal fault slip model of Zeng and Shen (2017) for the western U.S. that takes into account fault geometry and slip rates. Their model is derived from survey-mode and cGPS data supplemented by geologic slip rates. The residuals in Figure 12 are defined as the difference between the observed weekly station displacements minus the geologic-based model-predicted displacements and reflect transient motions (Klein et al., 2019). In Figure 12B, we show the accumulated transient displacements from an arbitrary initial epoch 2010.0 to 2018.6 compared to the secular model, showing the effects of postseismic deformation, subsidence, magmatism, as well as deviations from the Zeng and Shen (2017) secular model.

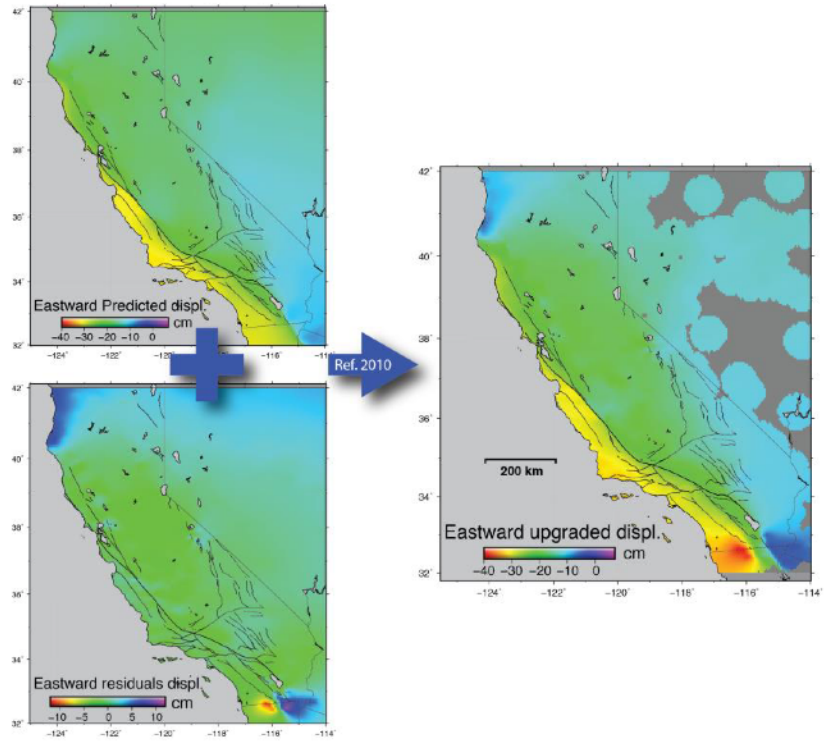

Figure 13. The final upgraded weekly displacement grid (right), here at t = 2017.7 for the east component, is the sum of the displacement field predicted by the interseismic model of Zeng and Shen (2017) (upper left), and the surface interpolation of residuals between observations and model (lower left) with respect to $t_0 = 2010$. The weekly displacement grid is one element of the dynamic datum (Klein et al., 2019), including the combined effect of secular and transient motions.

First, we use a median filter to create a weekly time series. Then, the interpolation of the horizontal displacement residuals is accomplished using a remove/interpolate/restore approach as follows:

(1) Construct north and east horizontal displacement 1 km grid spacing at some time t after a reference epoch (for demonstration purposes we use $t_0 = 2010.00$) by multiplying Zeng and Shen (2017) surface velocity map by $t - t_0$.

(2) Subtract the model displacements from the observed displacements (residuals) at the reference stations in north and east directions. We assume here that the residuals will be smooth so they have spatial variations at length scales greater that the spacing of the cGPS sites (> 10 km).

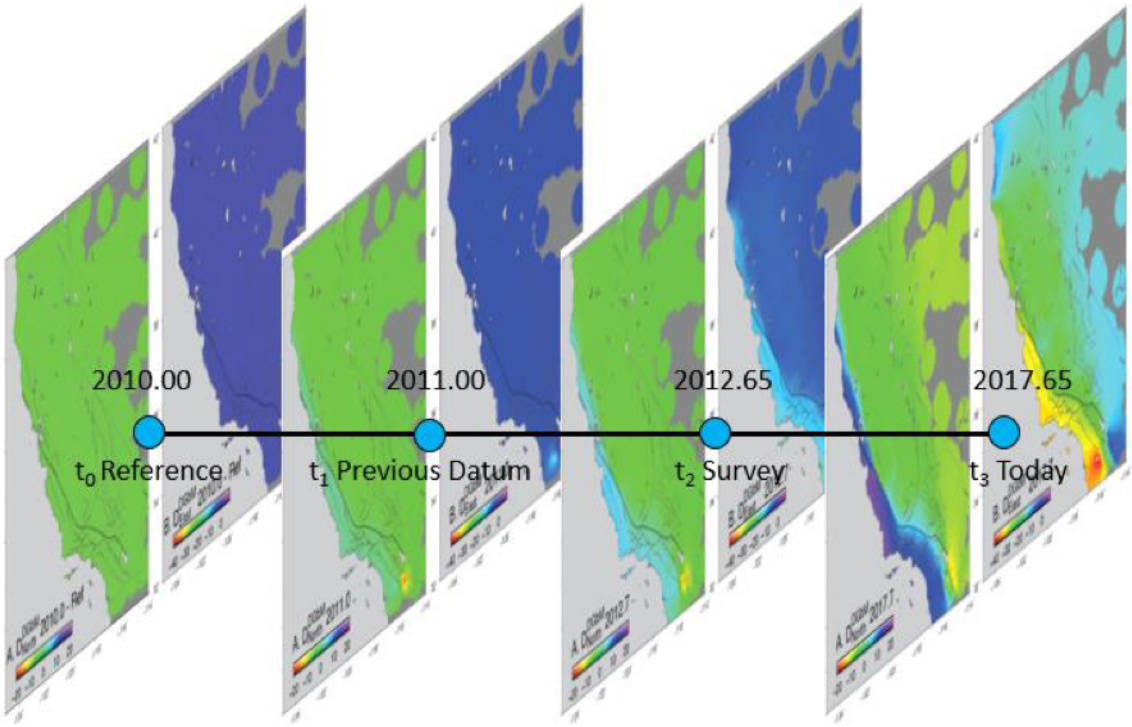

Figure 14. Horizontal residual displacement fields at four different epochs based on a 2010.0 reference epoch. Source: (Klein et al., 2019).

(3) Interpolate the north and east residuals (modeled minus predicted displacements) at a 1 km grid spacing using a 2-D elastic model to provide coupling between the two horizontal components (Haines & Holt, 1993; Haines et al., 2015; Sandwell & Wessel, 2016). This is accomplished using gpsgridder in the GMT software (https://docs.generic-mapping-tools.org/latest/supplements/geodesy/gpsgridder.html), where we retain only the 800 largest eigenvalues to solve for an approximate surface (-Cn800), assume a typically elastic medium (-S0.5), choose a constant offset fudging scheme (-Fd8), and incorporate the displacement measurement uncertainties as weighting factors in the interpolation (see -W flag). The majority of the interpolated residual grid fits the displacement residuals to within their uncertainties, though in regions of recent coseismic and postseismic motions this is not the case.

(4) Add the residual grid to the ZS2017 displacement model to achieve the final horizontal displacement grids, with 1 km spatial resolution.

The grids now contain the total motion accumulated since the initial epoch, that is, the predicted secular motions plus the observed transient motions (Figure 13). Each week's displacement field is stored in the SOPAC archive. Horizontal displacement fields from 4 epochs are shown in Figure 14. Moving between different epochs provides the basis of a dynamic datum (reference frame) (Klein et al., 2019).

In addition to the total displacement grids, we also create grids of the residual displacements representing the transient motions, tables of input data at the reference stations and movies that highlight the time evolution of each product. One product shows the non-accumulating weekly residual motions so that effects such as postseismic motions will appear to dissipate in time.

5.3 Vertical Displacements

For the vertical component, we spatially interpolate the vertical displacements without the use of an underlying model as described by Klein et al. (2019). In Figure 15 we show the accumulated vertical displacements between 1999.5 and 2018.6 in California and Nevada. The accumulated weekly vertical displacement maps, tables and movies are also archived on a weekly basis.

5.4 Misfits

The misfits between the observed displacements and those interpolated from the displacement fields at the reference stations provide a measure of interpolation uncertainty at any location within the area of interest in the horizontal (Figure 16) and, similarly for the vertical components. This interpolation uncertainty also includes the measurement uncertainties as a weighting factor in the interpolation, and thus provides a fuller measure of uncertainty. They are created by comparing the observed displacements and the interpolated

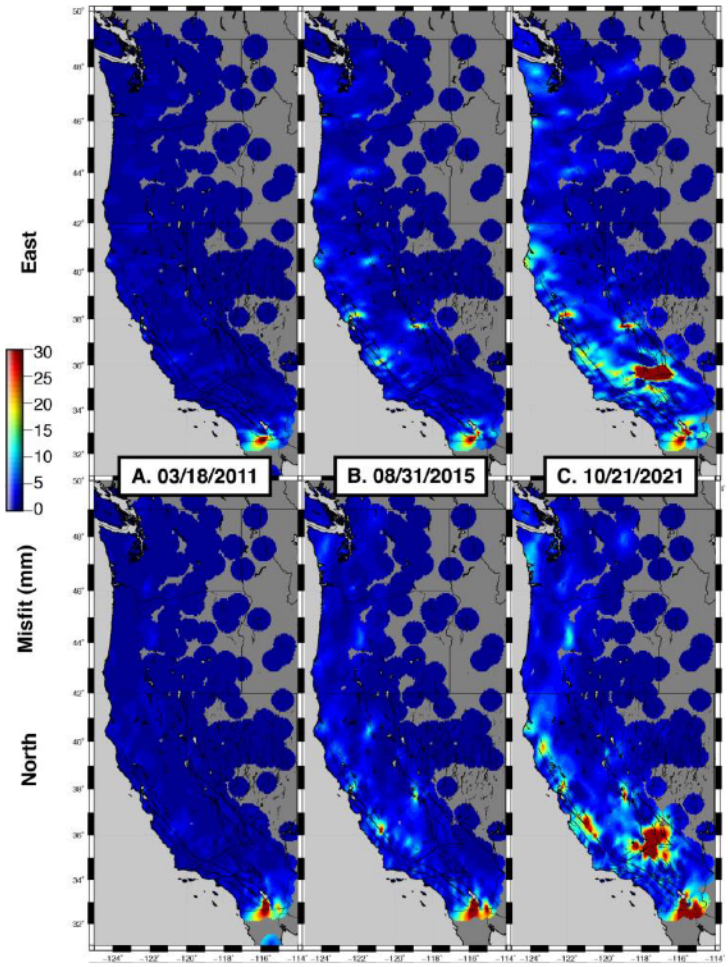

Figure 16. Horizontal misfit grids at three different epochs. 50 km circles drawn around GNSS stations indicating areas of sparse coverage.

displacements at the reference stations, and gridding the results. The misfit fields are also archived on a weekly basis.

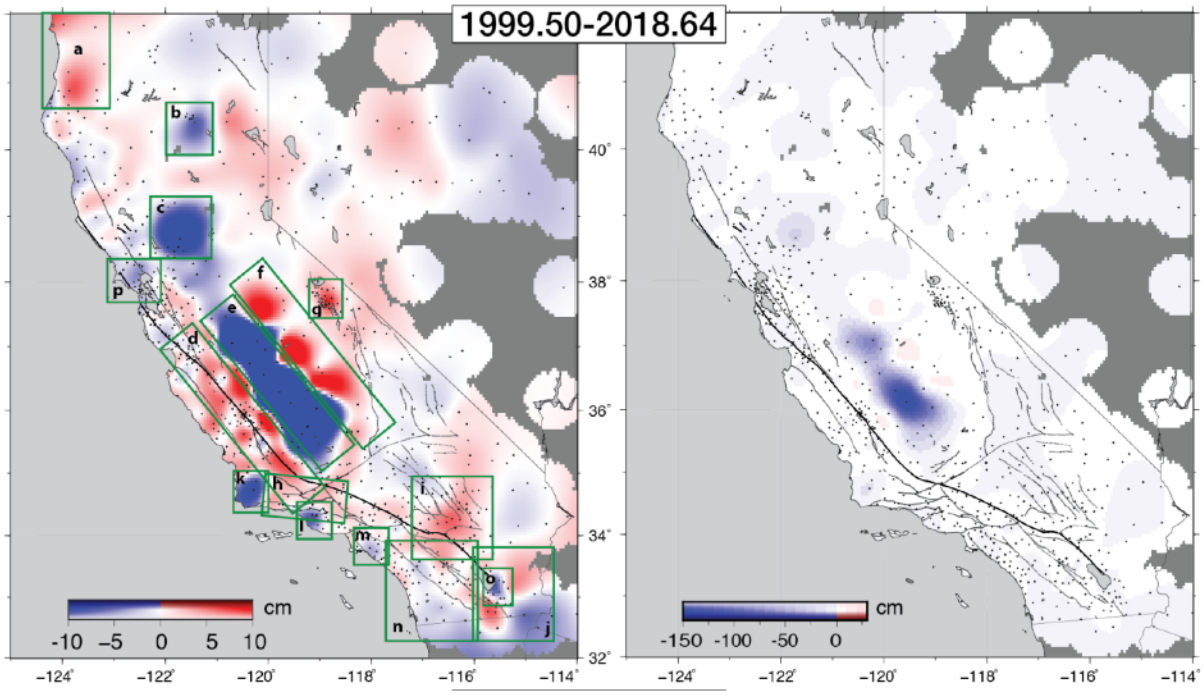

Figure 15. Accumulated vertical displacement field between 1999.5 and 2018.6, represented with 2 different color scales to show the full extent of subsidence (right panel) in the Central Valley. The lowercase letters (left panel) indicate areas of significant secular and transient vertical motion, Source (Klein et al. 2019).

5.5 Products

The input to the displacement products is weekly median values of daily displacements time series (although the resolution could be modified for special cases), updated weekly and uploaded to CDDIS (Table 3). The movies described in Table 4 provide the user with a powerful visual representation of crustal motions over time.

The .grd files are a type of netCDF file built within the GMT environment and hold all the displacement data values for each epoch of time for each given grid type. These can be used within GMT (https://docs.generic-mapping-tools.org/latest/), as well as other software types (e.g., GDAL, MATLAB).
YYYYMMDD indicates end date of the weekly grid

Table 3. Displacement Products

Dynamic Datum (total displacements)	
Horizontal	
Vectors	**Description**
dispNEvec_YYYYMMDD.pdf	Interseismic model + horizontal (NE) transients = accumulating total displacements since t0 (input to dynamic datum grids): Note:

	This shows the total motions so may partially obscure in time the transient motions and vice versa.
Grids	
dispNgrid_YYYYMMDD.pdf/grd; dispEgrid_YYYYMMDD.pdf/grd	Gridded North/East total displacements accumulating since t0. Zeng and Shen (2017) prediction [ucerf3_0.05_itrf_v*.grd] + surface interpolation of residuals between observations and model; Areas >75 km from GPS stations are masked.
misfitNgrid_YYYYMMDD.pdf/grd; misfitEgrid_YYYYMMDD.pdf/grd	Gridded North/East accumulating misfits, > 75 km mask. Gridded point values of displacements compared to interpolated values at reference stations.
Residuals	
residualNgridM_YYYYMMDD.pdf/grd; residualEgridM_YYYYMMDD.pdf/grd	Median North and East residuals between observed GNSS motions and Zeng and Shen (2017) interseismic predicted model motions
Data Tables	
dispNEgrid_YYYYMMDD.dat	North and East dynamic datum observations and predictions (FORMAT: lon; lat; NobsTotal; EobsTotal; NpredDynDat; EpredDynDat). Total displacements and dynamic datum
misfitNEgrid_YYYYMMDD.dat	North and East misfits for dynamic datum observations and prediction (FORMAT: lon; lat; NobsTotal; EobsTotal; misfitNpredDynDat; misfitEpredDynDat). Total displacements and dynamic datum
residualNEgridM_YYYYMMDD.dat;	Median North and East residuals between observed GNSS motions and Zeng and Shen (2017) interseismic predicted model motions (FORMAT: lon; lat; Nresid; Eresid).
Vertical	
Vectors	**Description**
dispUvec_YYYYMMDD.pdf	Up displacements accumulating since t0
Grids	
dispUgrid_YYYYMMDD.pdf/grd (Unmasked grids also available)	Gridded up displacements accumulating since t0; >75 km mask.
misfitUgrid_YYYYMMDD.pdf/grd (Unmasked grids also available)	Gridded Up of accumulating computed misfits, > 75 km mask. Gridded absolute values of residuals between dynamic datum displacements compared to interpolated values at reference stations.
Residuals	
residualUvec_YYYYMMDD.pdf/grd (Unmasked grids also available)	Residuals between point value at station and interpolated grid value. **Note:** Corresponds to residualUgrid
residualUgrid_YYYYMMDD.pdf/grd (Unmasked grids also available)	Gridded Up residuals between point value at reference station and interpolated grid values (observation – interpolated value). **Note:** misfitUgrid*.grd calculated using these values; see residualUvec*.dat data tables for station point values.
Data Tables	
dispUgrid_YYYYMMDD.dat	Observed up displacements and predicted up displacement from the green spline interpolation (FORMAT: lon; lat; measured; predicted).
residualUvec_YYYYMMDD.dat	Residual up values between observed displacement and the interpolated predicted values (FORMAT: lon; lat; Residual).
Horizontal Transients (wrt horizontal interseismic model)	

Vectors	Description
transientNEvec_YYYYMMDD.pdf	Horizontal transients (observed – predicted from interseismic model) accumulating since t0 at reference stations. Shows non-steady state transient deformation processes (postseismic deformation, creep, magmatic activity, etc.); transient portion of the dynamic datum. **Note:** components are gridded to transientNgrid and transientEgrid
transientNEvecW_YYYYMMDD.pdf	Horizontal weekly (**W**) transients (observed – predicted from interseismic model) non-accumulating since t0 at reference stations. Weekly non-steady state transient deformation processes (postseismic deformation, creep, magmatic activity, etc.) – postseismic transients, for example, will dissipate over time. **Note:** components are gridded to transientNgridW and transientEgridW
Grids	
transientNgrid_YYYYMMDD.pdf/grd; transientEgrid_YYYYMMDD.pdf/grd	Gridded North/East transients between observed and long-term interseismic model at the reference stations (accumulating). **Note**: Corresponds to transientNEvec
transientNgridW_YYYYMMDD.pdf/grd; transientEgridW_YYYYMMDD.pdf/grd	Gridded North/East weekly (**W**) transients between observed and predicted interseismic model at the reference stations (non-accumulating). **Note**: Corresponds to transientNEvecW
Data Tables	
transientNEgrid_YYYYMMDD.dat	North and East observed displacements and interseismic model predictions accumulating (FORMAT: lon; lat; NobsTotal; EobsTotal; NpredModelDat; EpredModelDat). Separate components of dynamic datum
transientNEgridW_YYYYMMDD.dat	North and East observed displacements and total interseismic model predictions non-accumulating **(W)** weekly (FORMAT: lon; lat; NobsTotal; EobsTotal; NpredModelDatW; EpredModelDatW). Separate components of dynamic datum (weekly)

Table 4. Displacement Movies

Movie Name	Description
Dynamic Datum	
Vectors	
dispNEvec_YYYYMMDD.mp4	Dynamic Datum horizontal
dispUvec_YYYYMMDD.mp4	Dynamic Datum up
residualNEvec_YYYYMMDD.mp4	Residual North and East vectors (accumulating)
residualUvec_YYYYMMDD.mp4	Residual vectors (U); difference of reference station values and interpolated values (accumulating)
Grids	
dispNgrid_YYYYMMDD.mp4; dispEgrid_YYYYMMDD.mp4; dispUgrid_YYYYMMDD.mp4	Dynamic data grids North, East, Up
misfitNgrid_YYYYMMDD.mp4; misfitEgrid_YYYYMMDD.mp4;	Dynamic data grid misfits North, East, Up

misfitUgrid_YYYYMMDD.mp4	
Transients	
Vectors	
transientNEvec_YYYYMMDD.mp4	Transient North East vectors (accumulating)
transientNEvecW_YYYYMMDD.mp4	Transient North East vectors weekly (non-accumulating)
Grids	
transientNgrid_YYYYMMDD.mp4; transientEgrid_YYYYMMDD.mp4	Transient grids (accumulating) North, East
transientNgridW_YYYYMMDD.mp4; transientEgridW_YYYYMMDD.mp4	Transient grids (non-accumulating) North, East

5.6 Archive Structure

File sent to CDDIS: **DisplacementGridsYYYYMMDD.tar.gz**

YYYYMMDD is the date that the file was created

SOPAC archive location:
http://garner.ucsd.edu/pub/measuresESESES_products/DisplacementGrids

Readme.txt

dynamic datum >
- **vector_products >**
  - **horizontals >**
    - dispNEvec_YYYYMMDD .pdf
    - residualNgridM_YYYYMMDD .pdf
    - residualEgridM_YYYYMMDD.pdf
    - **residuals >**
      - residualNgridM_YYYYMMDD.pdf
      - residualEgridM_YYYYMMDD.pdf
    - **data_tables >**
      - dispNEgrid_YYYYMMDD.dat
      - misfitNEgrid_YYYYMMDD.dat
      - residualNEgrid_YYYYMMDD.dat
  - **verticals >**
    - dispUvec_YYYYMMDD.pdf
    - **residuals >**
      - residualUvec_YYYYMMDD.pdf
    - **data_tables >**
      - dispUgrid_YYYYMMDD.dat
      - residualUvec_YYYYMMDD.dat
- **gridded_products >**
  - **horizontals >**
    - dispNgrid_YYYYMMDD.pdf/grd
    - dispEgrid_YYYYMMDD.pdf/grd

misfitNgrid_YYYYMMDD.pdf/grd
misfitEgrid_YYYYMMDD.pdf/grd
dispNgrid_unmasked_YYYYMMDD.grd
dispEgrid_unmasked_YYYYMMDD.grd
misfitNgrid_unmasked_YYYYMM DD.grd
misfitEgrid_unmasked_YYYYMMDD.grd
residuals >
residualNgridM_YYYYMMDD.pdf/grd
residualEgridM_YYYYMMDD.pdf/grd

verticals >
dispUgrid_YYYYMMDD.pdf/grd
misfitUgrid_YYYYMMDD.pdf/grd
dispUgrid_unmasked_YYYYMMDD.grd
misfitUgrid_umasked_YYYYMMDD.grd
residuals >
residualUgrid_YYYYMMDD.pdf/grd

transients >
vector_products >
horizontals >
transientNEvec_YYYYMMDD.pdf/grd
transientNEvecW_YYYYMMDD.pdf/grd
data_tables >
transientNEgrid_YYYYMMDD.dat
transientNEgridW_YYYYMMDD.dat

gridded_products >
horizontals >
transientNgrid_YYYYMMDD.pdf/grd
transientEgrid_YYYYMMDD.pdf/grd
transientNgridW_YYYYMMDD.pdf/grd
transientEgridW_YYYYMMDD.pdf/grd

movies >
dynamic_datum >
vectors >
dispNEvec_YYYYMMDD.mp4
dispUvec_YYYYMMDD.mp4
residualNEvec_YYYYMMDD.mp4
residualUvec_YYYYMMDD.mp4

gridded >
dispNgrid_YYYYMMDD.mp4
dispEgrid_YYYYMMDD.mp4
dispUgrid_YYYYMMDD.mp4
misfitNgrid_YYYYMMDD.mp4
misfitEgrid_YYYYMMDD.mp4
misfitUgrid_YYYYMMDD.mp4

transients >
vectors >
transientNEvec_YYYYMMDD.mp4
transientNEvecW_YYYYMMDD.mp4

gridded >

transientNgrid_YYYYMMDD.mp4
transientEgrid_YYYYMMDD.mp4
transientNgridW_YYYYMMDD.mp4
transientEgridW_YYYYMMDD.mp4

6. Level 3: High-Rate GNSS & Seismogeodetic Records for Historical Earthquakes

6.1 Background

Our level 1 products include daily GNSS displacements based on 24-hours of data, typically sampled at 15 seconds. Another product is high-rate, typically 1-10 Hz, displacements. The analysis of high-rate GNSS data is referred to as "GNSS seismology" since it can also sense dynamic motions generated by, for example, earthquakes in addition to high-rate displacements (Bock and Melgar, 2016 and references therein). "Coseismic" refers to motions during an earthquake that are a superposition of dynamic displacements and static (permanent) displacements. A comprehensive archive of GPS high-rate displacements of 29 earthquakes from 2003-2018 with moment magnitudes of Mw 6.0-9.0 is described by (Ruhl et al., 2019). However, the sensitivity of seismic instruments to ground motions is much higher than that of GNSS, which cannot sense the arrival of low-amplitude (sub mm) seismic P waves even in the near field of a great earthquake. GNSS networks have captured large amplitude teleseismic waves (seismic signals greater than about a thousand kilometers from an earthquake's location). However, at these distances dynamic GNSS displacements are only accurate enough to discern S waves from large earthquakes (~M >7.5), while traditional seismic measurements at any location on Earth can resolve earthquakes as small as > M 5.3, a factor of 1000 better than geodesy. "Seismogeodesy," the optimal combination of collocated high-rate GNSS and seismic (strong motion accelerometer) data, provides coseismic (static and dynamic) displacements and seismic velocities that can detect P waves. Table 5 shows earthquakes that have been observed with GPS seismology and seismogeodesy through 2019. A review of GNSS seismology and seismogeodesy is provided by Bock and Melgar (2016) and Bock and Wdowinski (2020), and references therein.

Table 5. Significant earthquakes measured with GPS seismology and seismogeodesy

Earthquake	Mw	References
2002 Denali fault, Alaska (teleseismic – 4000 km from source)	7.9	(Larson et al. 2003; Kouba 2003; Bock et al. 2004)
2003 San Simeon, California	6.6	(Ji et al. 2004)
2003 Tokachi-oki, Japan[1]	8.3	(Miyazaki et al. 2004; Emore et al. 2007; Crowell et al. 2009; Crowell et al. 2012)
2004 Parkfield, California	6.0	(Langbein et al. 2005; Barbot et al. 2009)
2004 Sumatra-Andaman, Indonesia (teleseismic – 14,000 km from source)	9.3	(Davis and Smalley 2009)
2005 West Off Fukuoka Prefecture, Japan	7.0	(Kobayashi et al. 2006)
2008 Wenchuan, China	8.0	(Yin et al. 2013)
2010 Mentawai, Indonesia	7.7	(Melgar et al. 2015)
2010 Maule, Chile[1]	8.8	(Melgar et al. 2015) (Yue et al. 2014)
2010 El Mayor-Cucapah, Mexico[1]	7.2	(Crowell et al. 2012)

2011 Tohoku-oki, Japan[1]	9.0	(Crowell et al. 2012) (Melgar et al. 2013; Bletery et al. 2014) (Grapenthin and Freymueller 2011 – teleseismic)
2012 Nicoya, Costa Rica	7.5	(Melgar et al. 2015) (Yin and Wdowinski 2014)
2014 Napa, California[1]	6.1	(Melgar et al. 2015)
2014 Aegean Sea, Greece	6.5	(Melgar et al. 2015)
2014 Iquique, Chile	8.2	(Melgar et al. 2016)
2015 Illapel, Chile[1]	8.3	(Melgar et al. 2016)
2016 Kumamoto, Japan[1]	7.0	(Kawamoto et al. 2016)
2016 Kaikoura, New Zealand	7.8	(Kaiser et al. 2017)
2017 Chiapas, Mexico[1]	8.2	(Ye et al. 2017)
2019 Ridgecrest, California earthquakes[1]	6.2/7.1	(Xu et al., 2019)

[1]Sufficient GPS/accelerometer collocations available for seismogeodesy

GPS seismology and seismogeodesy are particularly advantageous in the near field (within 100's of km) of large earthquakes, for local earthquake and tsunami warning and rapid response. Figures 17 and 18 indicates the advantages and disadvantages of seismic (broadband seismometers, strong-motion accelerometers) and geodetic (GPS/GNSS) instruments compared to the seismogeodetic combination. Broadband seismometers that measure ground velocities go off-scale ("clip") when close to an earthquake's epicenter, while GPS does not. Therefore, seismic stations are equipped with strong-motion instruments (accelerometers) that do not clip. Absolute station displacement is the most useful measurement for down-stream modeling of the earthquake source, but seismology requires single integration of observed broadband velocities or a double integration of accelerations. The accuracy of absolute displacements from broadband seismometers is poor because of its limits in dynamic range. Doubly-integrating accelerations to displacements is subject to various spurious

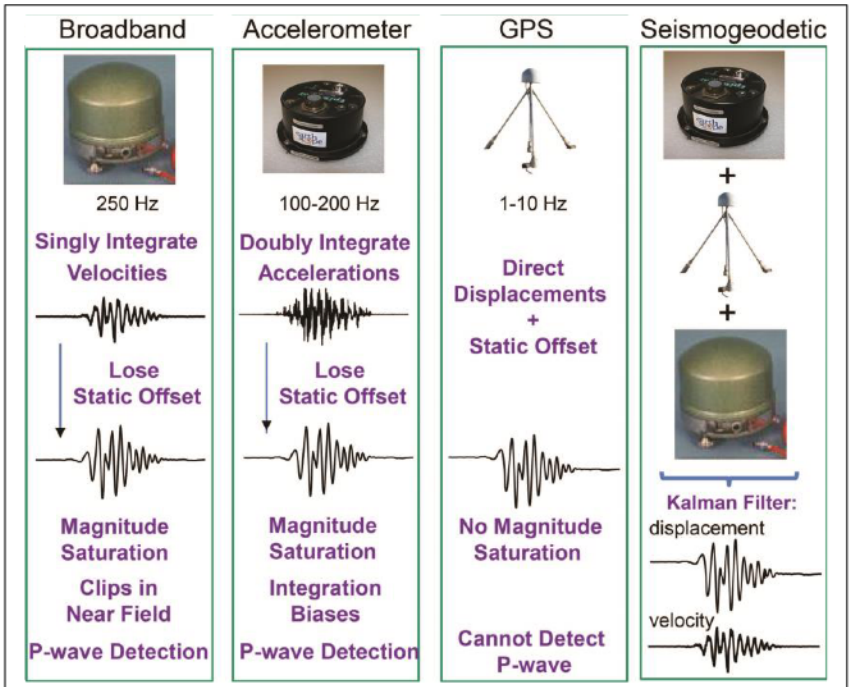

Figure 17. Displacements derived from GPS and seismic instruments: advantages and disadvantages. The seismogeodetic combination of GPS displacements, broadband velocities, and strong motion accelerations using a Kalman filter maintains the advantages of each data type and minimizes their disadvantages.

breaks, termed "baseline" errors (not to be confused with GNSS baselines), due to numerical errors in the integration procedure, mechanical hysteresis, and cross-axis sensitivity between the test mass/electromechanical system used to measure each component of motion. The main disadvantage is that accelerometers are incapable of discerning between rotational and translational motions, leading to unphysical drifts in the resulting displacements. Baseline corrections are usually taken into account by a high-pass filter, resulting in accurate recovery of the mid- to high-frequency portion of the displacement record. However, in the process long-period information in particular the static offset is lost. The static offset (permanent motion) is critical for rapid estimation of earthquake magnitude and mechanism, an essential element for earthquake and tsunami early warning. Finally, unlike GNSS, seismic instruments are subject to magnitude saturation, meaning that is not possible to distinguish between, say, a magnitude 8 and 9 earthquake (a factor of about 30 in energy release), since the scaling relationships between seismic wave arrivals and earthquake magnitude break down at the higher magnitudes.

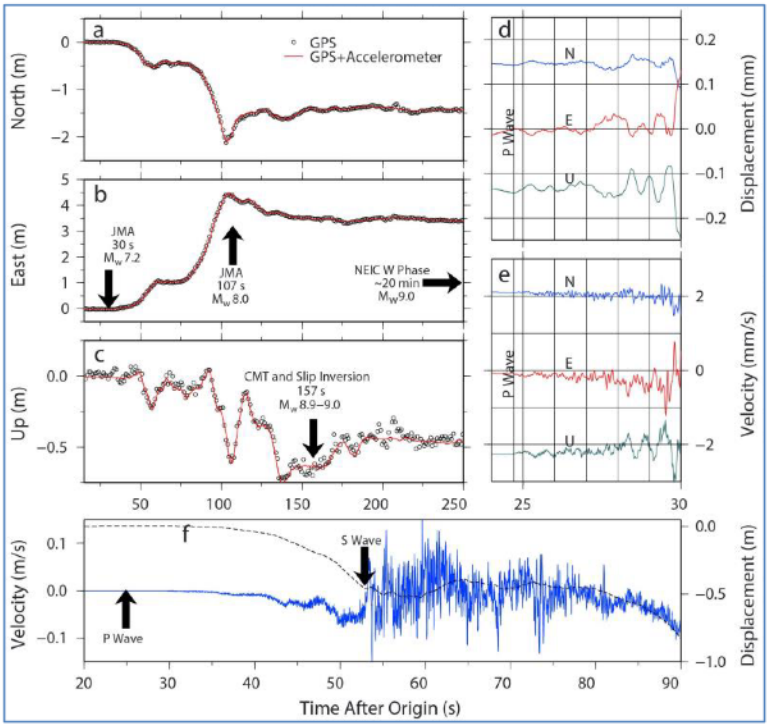

Figure 18. Demonstration of the utility of GNSS and seismogeodetic data for rapid earthquake and tsunami warning systems. 3-D seismogeodetic displacements and velocities estimated from 1 Hz GPS displacements at Japan's GEONET station 0914 (black circles) and 100 Hz K-NET accelerometer MYG003, 155 km from the earthquake's epicenter determined by the Japan Meteorological Agency. The Japanese earthquake early warning system, dependent on regional seismic station data, estimated an initial magnitude of Mw7.2, 30 seconds after earthquake onset time and Mw8.0 after 107 seconds, a classic example of magnitude saturation. Replay of the event with seismogeodetic data or GNSS data alone (black circles) indicates that a magnitude of Mw8.9-9.0 within 157 seconds. The seismogeodetic data also allows the P wave to be detected as a basis for earthquake early warning. Rapid and accurate magnitude estimation is key for issuing tsunami early warnings. Source: (Melgar et al. 2013).

For earthquake early warning where timely near-source observations are critical, GNSS is not sensitive enough to detect seismic P-waves, particularly in the vertical direction where the P-wave with mm-level amplitudes is most pronounced; the precision of real-time GPS instantaneous displacements is about 1 cm in the horizontal components and 5-10 cm in the vertical (Genrich and Bock 2006). The displacement precision observed with seismogeodesy during dynamic shaking is reduced by a factor of two in the vertical and by about 20% in the horizontal component, compared to GPS alone, though

still dominated by long-period errors in the GPS observations due to multipath (Saunders et al. 2016). Since the dynamic range of GPS instruments has no upper limit, GPS and broadband seismic sensors cover together the entire possible range of dynamic and static surface displacement (up to the Nyquist frequency). A study comparing the displacements and seismic velocities obtained with observatory-grade accelerometers and inexpensive Microelectromechanical (MEMS) accelerometers demonstrated the same level of precision in seismic velocity at distances of tens of km for earthquakes as small as ~M4, where there is no permanent displacement (Saunders et al. 2016; Goldberg and Bock 2017).

6.2 Description of ESDR

The preferred analysis for GPS seismology is the method of precise point positioning (PPP) (Zumberge et al., 1997; Kouba et al., 2001) since it is performed with respect to a global reference frame rather than relative positioning, which requires base stations that may be in the zone of deformation of a large earthquake. As in our daily displacement Level 1C ESDRs, JPL and SOPAC use different PPP software. JPL uses the GipsyX software (https://gipsy-oasis.jpl.nasa.gov/index.php?page=software) and SOPAC uses a variation of the PANDA software (Geng et al., 2012), the PRIDE PPP_AR software https://github.com/PrideLab/PRIDE-PPPAR from Wuhan University (not the GAMIT software used for earlier ESDRs).

(1) Using a common source of metadata from the SOPAC archive, the two groups will independently analyze the historical record of GPS/GNSS data collected during significant earthquakes and any new earthquakes during the project period to produce a time series of high-rate displacements. These data will be supplemented from data archived at other centers. Although the data were collected in real time, the PPP analysis will be performed in 24-hour batches and a solution will include 1 Hz displacement spanning a day (i.e., 86,400 samples). If data are available at a higher rate (PBO stores data collected at 10 Hz for large events within their zone of coverage), we will analyze the data at the higher rates (up to 864,000 samples per day). Of course, one can then average the high-rate solutions to any sub-daily interval to study other phenomena. We will include data from one full day before to three full days after each event, that is, if the earthquake occurs at mid-day on day x, then a full day of data will be collecting for x-3 and x+3. SOPAC maintains an archive of relevant high-rate data from stations in the Western U.S. to capture the early postseismic period.

(2) SOPAC will also process data from collocated seismic (accelerometer) and GNSS stations using the seismogeodetic approach (Bock et al., 2011; Saunders et al., 2016); Goldberg and Bock, 2017) (Figure 18) for historical events and new events occurring over the project period. High-rate displacements and seismic velocities will be estimated at the sampling rate of the seismic instruments (typically, 100 Hz).

(3) The high-rate GNSS and seismic displacements and the raw data will be archived at SOPAC and at the CDDIS DAAC for use by other investigators.

6.3 Products

Our products (Figure 19) are delivered to the CDDIS in a tar file, *EarthquakeDisplacements_MEaSUREs_ESESES_YYYYMMDD* that is updated with the most recent significant earthquakes. *YYYYMMDD is the date of the most recent submission.*

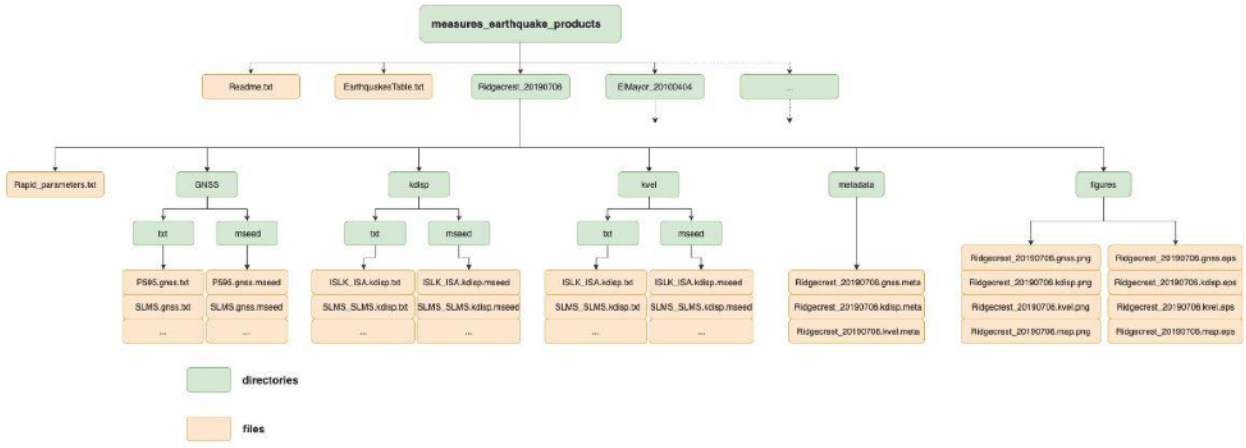

Figure 19. Directory Structure – Earthquake Products

SOPAC archive directory

http://garner.ucsd.edu/pub/measuresESESES_products/EarthquakeDisplacements/

File Descriptions

(1) Readme.txt – this file (top level)
(2) EarthquakesTable.csv (top level)

earthquakeName(_Solution) examples (name_ YYYYMMDD):

Ridgecrest_20190706
Ridgecrest_20190706_2
Parkfield_20040928
Tohoku_20110311

Note: these names refer to a particular high-rate analysis of an earthquake rather than the earthquake itself. For example, there could be a 2nd analysis by a different research group. In the directory structure we would specify a second file, Ridgecrest_20190706_2 or another designation after the underscore instead of "2".

http://garner.ucsd.edu/pub/measures_earthquake_products/EarthquakesTable.csv

Example:
Event Name;Country;Mw;Origin Time (UTC);Latitude(deg. N);Longitude (deg. E),Depth (km);Mechanism;GNSS Stations;Collocated stations;GNSS processing

Ridgecrest_20190706;United States;7.1;2019_07_06T03:19:53.0;35.770;-117.599;8.0;StrikeSlip;490;91;PPP

Second level (See Directory Structure figure 19):

(3) "metadata" (text file) (third level)

e.g.,
http://garner.ucsd.edu/pub/measuresESESES_products/EarthquakeDisplacements/Ridgecrest_20190706/metadata/

 # GNSS Network;GNSS Station;Latitude (N);Longitude I;Elevation (m);Sampling Rate (Hz),Gain,Units

NOTA;BBDM;34.582201;-119.981518;204.885800;1.00;1000.00;counts/m

(4) Seismogeodetic Displacements

e.g., http://garner.ucsd.edu/pub/measuresESESES_products/EarthquakeDisplacements/Ridgecrest_20190706/kdisp/

GNSS Network;GNSS Station;Latitude (N);LongituI€;Elevation (m);Sampling Rate (Hz);Gain;Units;Seismic Network ;Seismic Station;Latitude (N);LongI€(E);Elevation (m)

NOTA;SONG;33.380750;-117.560270;23.000000;100.00;1000.00;counts/m;CI;SOC;33.387610;-117.5801;52.000000

(5) Seismogeodetic Velocities

http://garner.ucsd.edu/pub/measuresESESES_products/EarthquakeDisplacements/Ridgecrest_20190706/kvel/

GNSS Network;GNSS Station;Latitude (N);LIitude (E);Elevation (m);Sampling Rate (Hz);Gain;Units;Seismic Network;Seismic Station;Latitude (NIongitude (E);Elevation (m)

NOTA;SONG;33.380750;-117.560270;23.000000;100.00;1000.00;counts/(m/s);CI;SOC;33.387610;-117.580130;52.000000

(6) "figures" directory (figures are available in PNG and EPS formats)

GNSS displacements:

http://garner.ucsd.edu/pub/measuresESESES_products/EarthquakeDisplacements/Ridgecrest_20190706/figures/Ridgecrest_20190706.gnss.png

Seismogeodetic displacements (Figure 20)

http://garner.ucsd.edu/pub/measuresESESES_products/EarthquakeDisplacements/Ridgecrest_20190706/figures/Ridgecrest_20190706.kdisp.png

Seismogeodetic velocities (Figure 21)

http://garner.ucsd.edu/pub/measuresESESES_products/EarthquakeDisplacements/Ridgecrest_20190706/figures/Ridgecrest_20190706.kvel.png

Map (Figure 22)

http://garner.ucsd.edu/pub/measuresESESES_products/EarthquakeDisplacements/Ridgecrest_20190706/figures/Ridgecrest_20190706.map.png

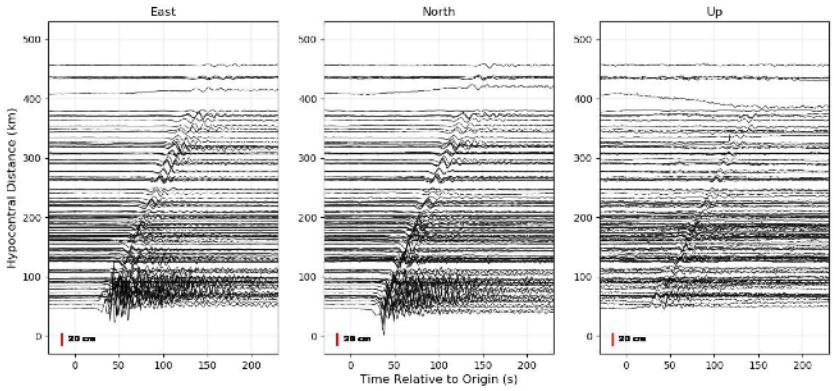

Figure 20. 2010 Mw 7.1 El Mayor-Cucapah Earthquake Station Displacements as a function of epicentral distance

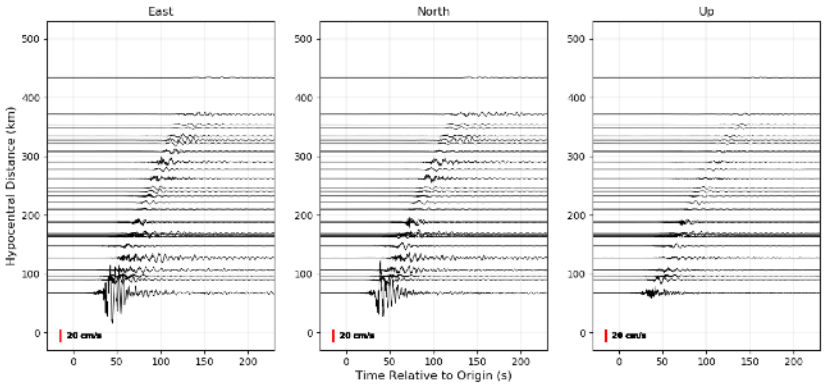

Figure 21. 2010 Mw 7.1 El Mayor-Cucapah Earthquake Station Velocities as a Function of Epicentral Distance

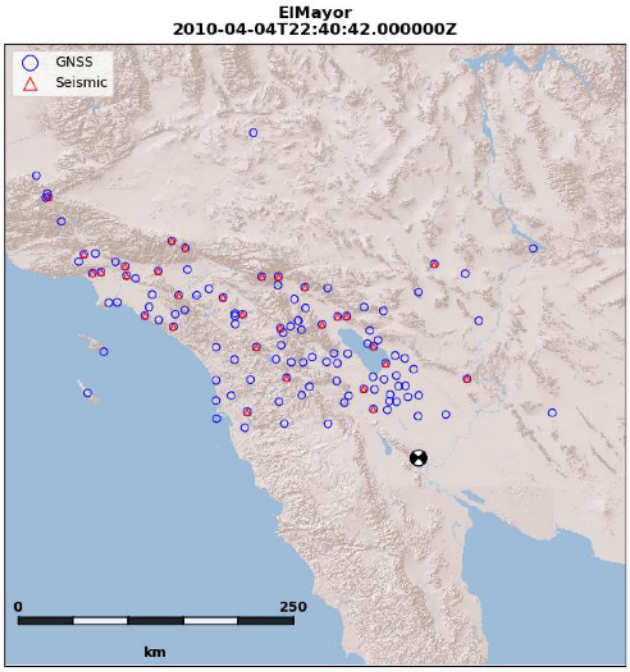

Figure 22. 2010 Mw 7.1 El Mayor-Cucapah Earthquake Stations with CMT solution (beachball) of Epicentral Distance

Data Directories (time tags are UTC), e.g.:

http://garner.ucsd.edu/pub/measuresESESES_products/EarthquakeDisplacements/Ridgecrest_20190706/

(7) "GNSS" - GNSS-only solutions

MiniSEED (".mseed") binary file

e.g., ACSB.gnss.mseed.gz (ACSB is 4-character GNSS station code)

Text (".txt") file

e.g., ACSB.gnss.txt.gz

(8) ".kdisp" – Seismogeodetic displacements

MiniSEED (".mseed") – binary file

e.g., BILL_BLL.mseed.gz (BILL is 4-character GNSS station code; BLL is accelerometer station code)

Text (.txt) file

e.g., BILL_BLL.kdisp.txt.gz

(9) ".kvel" – Seismogeodetic velocities

MiniSEED (".mseed") – binary file

e.g., BILL_BLL.kvel.mseed.gz

Text (.txt) file

e.g., BILL_BLL.kvel.txt.gz

(8) "Coseismic_Parameters"

Filename: Coseismic_parameter.txt

Header: Network Station BI Lat Lon Alt(m) dE(mm) dN (mm) dU (mm) dE presig(mm) dNpresig(mm) dUpresig(mm) dEpostsig(mm) dNpostsig(mm) dUpostsig(mm) PGD(mm) PGDtime(s) SNR(all) SNR(hor) Hyp.Distance(km)

Table 6. Coseismic Parameters[1]

Parameter	Units	Description
Network		Name of real-time network
Station		GNSS 4-character code/Accelerometer Code
BI[2]		Band code: general sampling rate and response band. For example: S for short period, H for high broad band, I – instrument code. What is being measured. For example: H is high gain seismometer, N is an accelerometer.
Lat	Decimal degrees	Latitude of station
Lon	Decimal degrees	Longitude of station
Altitude	Meters	
dE	Millimeters	East component
dN	Millimeters	North component
dU	Millimeters	Up component
dE presig	Millimeters	Pre-earthquake displacement sigma East
dNpresig	Millimeters	Pre-earthquake displacement sigma North
dUpresig	Millimeters	Pre-earthquake displacement sigma Up
dE postsig	Millimeters	Post-earthquake displacement sigma East
dNpostsig	Millimeters	Post-earthquake displacement sigma North
dUpostsig	Millimeters	Post-earthquake displacement sigma Up
PGD[3]	Millimeters	Peak ground displacement
PGDtime	Seconds	Time of peak ground displacement from earthquake onset time
SNR(all)		Single/Noise ratio all components (N, E, U)
SNR(hor)		Single/Noise ratio horizontal (N, E)
Hypocentral Distance	Kilometers	Distance of station to hypocenter

[1] Golriz et al. (2021)
[2] http://www.fdsn.org/pdf/SEEDManual_V2.4_Aendix-A.pdf
[3] Ruhl et al. (2019)

MiniSEED – binary format (has provision for displacements and seismic velocities)

Reference: https://ds.iris.edu/ds/nodes/dmc/data/formats/miniseed/

Convert MiniSeed to Text: https://github.com/iris-edu/mseed2ascii/blob/master/doc/mseed2ascii.md

Text – format is described in the header of each file:
East;North;Up;time(sec. relative to origin)
Positions are taken relative to 10 seconds average before origin time
Data start 1-minute before origin time, and end 15-minutes after, depending on availability

Note: We have expanded and modified the approach taken by the zenodo archive of GNSS earthquake displacement waveforms described by Ruhl et al. (2019). They do not archive seismogeodetic velocities.

References:

Bock, Y., D. Melgar, B. W. Crowell (2011), Real-Time Strong-Motion Broadband Displacements from Collocated GPS and Accelerometers, Bulletin Seismological Society of America, 101, 2904-2925, doi: 10.1785/0120110007.

Bock, Y. & D. Melgar (2016), Physical Applications of GPS Geodesy: A Review, Rep. Prog. Phys. 79, 10, doi:10.1088/0034-4885/79/10/106801

Bock, Y. & S. Wdowinski (2020), GNSS Geodesy in Geophysics, Natural Hazards, Climate, and the Environment, in Position, Navigation, and Timing Technol[og]ies in the 21st Century: Integrated Satellite Navigation, Sensor Systems, and Civil Applications, IEEE, 2021, 741-820, doi: 10.1002/9781119458449.ch28.

Golriz, D, Y. Bock & X. Xu (2021), Defining the Coseismic Phase of the Crustal Deformation Cycle with Seismogeodesy, J. Geophys. Res.: Solid Earth, 126, e2021JB022002. https://doi.org/10.1029/2021JB022002

Ruhl, C.J., Melgar, D., Geng, J., Goldberg, D.E., Crowell, B.W., Allen, R.M., Bock, Y., Barrientos, S., Riquelme, S., Baez, J.C. and Cabral-Cano, E. (2019). A global database of strong-motion displacement GNSS recordings and an example application to PGD scaling. Seismological Research Letters, 90(1), pp.271-279.

Zenodo Web Page (2018): https://zenodo.org/record/1434374#.X-udln-YLQl

Zenodo Archive: https://zenodo.org/record/1434374/files/dataset_ruhl_etal_2018_version2.tar.gz?download=1

7. Level 4: ETS Transients

7.1 Plate Boundary Aseismic Transients

Advances in observational techniques in geodesy and seismology have led to the discovery of a diverse spectrum of slow earthquakes such as slow slip events (SSEs), non-volcanic tremor, low frequency earthquakes and very low frequency earthquakes (Peng and Gomberg, 2010). These slow earthquakes have distinctive scaling relations (Ide et al., 2007) and rupture characteristics compared to conventional earthquakes. The discovery of slow slip events such as episodic tremor and slip (ETS) in Cascadia margin over the past decades has changed our understanding of tectonic hazards and the earthquake cycle (Dragert et al., 2001; Rogers and Dragert, 2003). Slow slip transients can change stress on the fault interface, trigger earthquake swarms or seismicity (e.g., Segall et al., 2006; Lohman and McGuire, 2007; Fu et al., 2015), and release accumulated elastic strain on the fault interface (e.g., Liu et al., 2015a; Dixon et al., 2014). They seem to occur throughout the interseismic period and have now been observed at a number of subduction zones (Beroza and Ide, 2011). As slow slip transient may evolve into catastrophic megathrust earthquakes (Segall and Bradley, 2012), proper detection and characterization of slow slip events is crucial in our understanding of earthquake hazard. Combined with seismic tremor catalog, a high-quality transient catalog enables the investigation of the genesis and mechanism of slow earthquakes.

The Level 3 residual displacement time series (Figure 3) analysis (section 2.1.8) can be mined for transient motions that can vary both temporally and spatially.

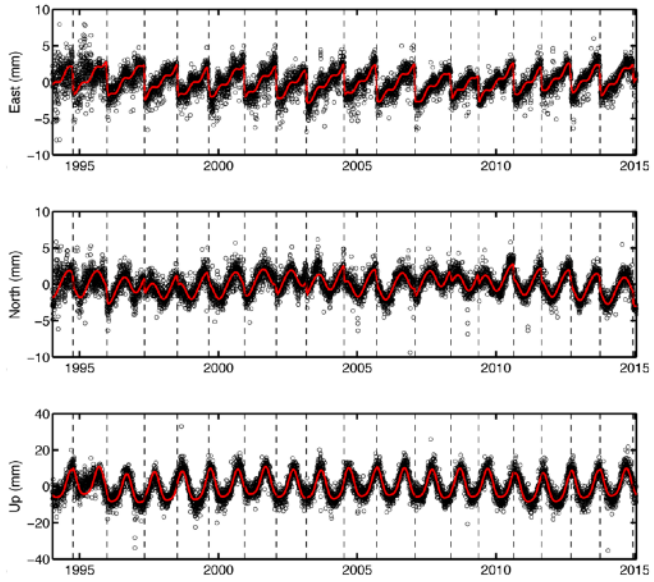

Figure 23. Model fit (red line) to the detrended position time series (black circles) at the Cascadia site ALBH. Top to bottom: East, North and Up components respectively. Source: (Liu et al., 2015b; Crowell et al., 2016).

7.2 Methodology

For this Level 4 ESDR (Figure 2), we will use a methodology developed for the financial sector, a financial momentum oscillator based on relative strength index (RSI) to detect when the residual time series deviate above the normal variance. Kurtosis minimization is then used to quantify the transient probabilities associated with any detected events. This approach has been applied by Crowell et al. (2016) to Level 1C residual time series to detect episodic tremor and slip events (RTS) in northern Cascadia. An advantage of this approach is that it can be performed on a station-by-station basis, which allows for the detection of outliers more readily than network approaches. Furthermore, it can be

fully automated and thus is well suited for operational transient detection and classification.

The RSI based algorithm provides initial estimates of the centroid time and duration of ETS events. To estimate the total displacement of the detected transients we model the residual displacement time series for inter-ETS linear rates, annual and semi-annual variations, and episodic slow slip (Figure 23) (Liu et al., 2015b). We use a hyperbolic function and employ a grid-search to estimate the optimal duration and centroid time. This parametric model ensures a robust estimate of transient displacement with uncertainties. Examination of the accumulated displacements for the ETS events in northern Cascadia margin shows considerable variability of surface deformation in spite of fairly regular recurrence, implying underlying slip complexity.

Once the surface transients are quantified in space and time, the next step is to model transient slip on the fault interface using the mature Network Inversion Filter (NIF) (Figure 24) (Segall and Matthews, 1997; McGuire & Segall, 2003; Liu et al., 2010, 2015a, b). The NIF and its variants have been successfully applied to model slip transients in diverse tectonic settings including Cascadia (e.g., Schmidt and Gao 2010; Bartlow et al. 2011), Japan (e.g., Miyazaki et al. 2006; Ozawa et al. 2007; Liu et al. 2010, 2015a), New Zealand (e.g., Bartlow et al., 2014), southcentral Alaska (Fu et al., 2015), Hawaii (e.g., Segall et al. 2006) and Costa Rica (Voss et al., 2018). This ESDR will, for the first time, combine automated transient detection and NIF to systematically analyze the state of the Cascadia margin and other subduction zones around the globe.

To summarize, starting with the Level 1 combined displacement time series residuals (section 6), we will (1) identify the transients, their duration and centroid, (2) estimate the total surface displacements, (3) model the fault slip and (4) catalog the Level 4 results. We will continue to

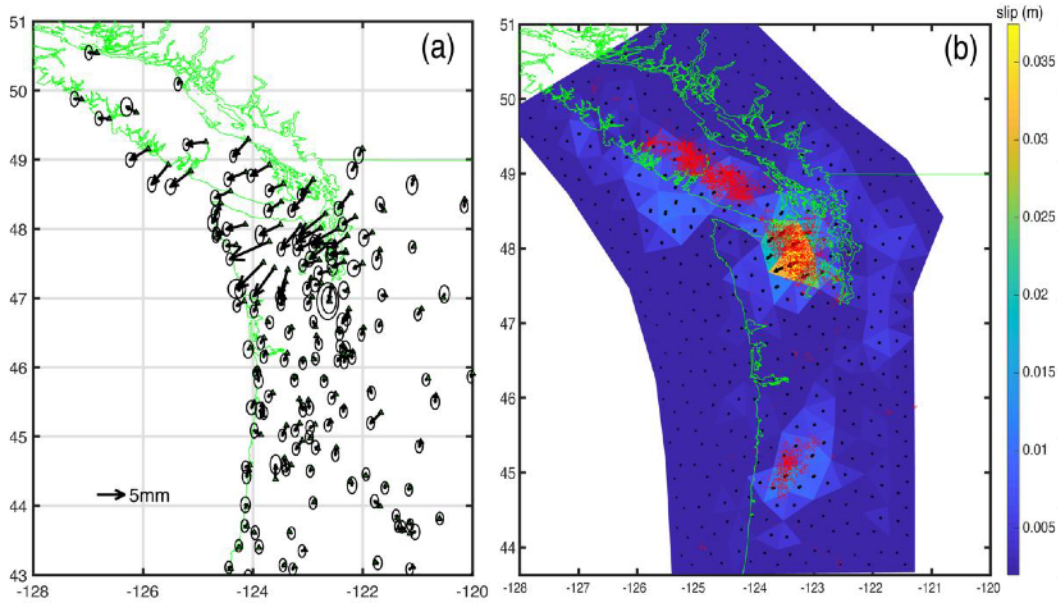

Figure 24. (a) Total surface displacements for 2014 November ETS event along the Cascadia subduction zone; (b) Accumulated transient slip from slip inversion. Red dots: tremor from PNSN catalog.

focus on Cascadia and expand to other tectonically active and transient rich regions as we include more GNSS sites in our network densification efforts.

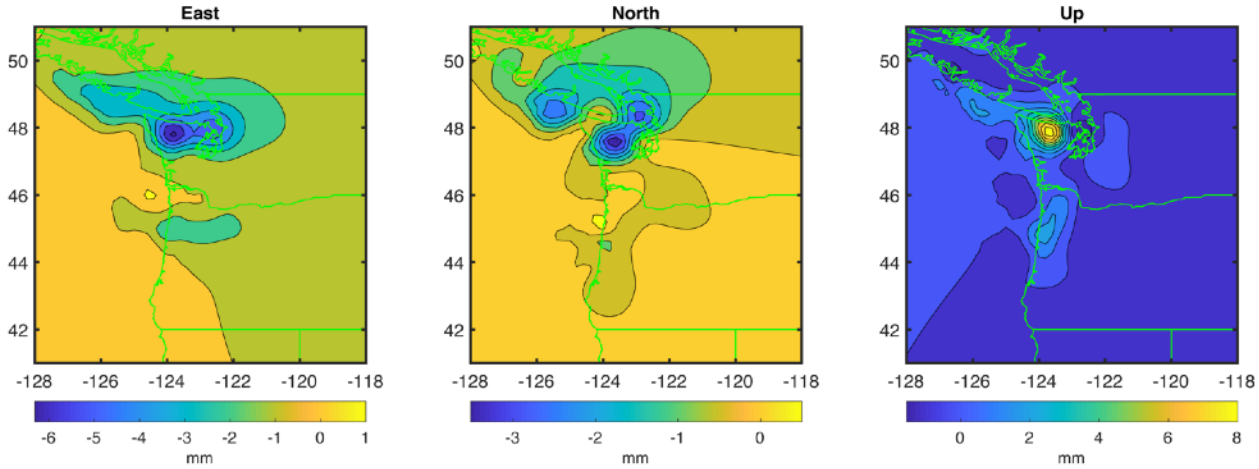

Figure 25. (Left to right) Mapview of east, north, up component of transient surface displacement for 2014 ETS event on a uniform grid.

7.3 Transient Products

The transient products are contained in a tar file with the name:

RegionTransient_YYYYMMDD.tar.gz at the date (YYYYMMDD) of the most recent upload to CDDIS

e.g., CascadiaETS_20210412.tar.gz ("Cascadia" is region; "ETS" is the transient type)

The directory structure for the SOPAC archive is as follows for Cascadia ETS events

http://garner.ucsd.edu/pub/measuresESESES_products/Transients/CascadiaETS/

Top directory:

ReadMe.txt

Subdirectory for each region and type of transient, e.g., CascadiaETS

The subdirectory will include:

A list of all ETS events:

ETS_event.list - list of ETS transients with event tag, start and end times, e.g.,

Event	start	end
evt94	1994-Sep	1994-Dec
evt95	1995-Nov	1996-Mar

Then a folder for each event, *evtYY*, e.g.,

evt94

evt95

In each folder:

evttag_disp.txt: Transient displacements and uncertainties at GNSS sites, Units: mm

Format: site_name start_date end_date longitude latitude e n u se sn su; se,sn and su are one sigma uncertainties, e.g.,

site start_date end_date longitude latitude e(mm) n(mm) u(mm) se(mm) sn(mm) su(mm)

ALBH 20001030 20010109 -123.487 48.390 -4.3486 -2.1548 -4.2028 0.318 0.460 1.339

BCOV 20001030 20010109 -126.843 50.544 0.4230 0.2306 -4.2355 0.335 0.472 1.398

evttag_disp.pdf: Map of transient displacements at GNSS sites (Figure 24a)

evttag_disp_grd.txt: Transient displacements at uniform grid (0.2x0.2 deg) from slip model, Units: mm

Format: longitude latitude east(mm) north(mm) up(mm), e.g.,

Lon Lat e(mm) n(mm) u(mm)

-128.000 41.000 0.0189 0.0245 0.0029

evttag_disp_grd.pdf: Map of transient displacements on a uniform grid (Figure 25)

evttag_slip.txt: Accumulated transient slip of ETS event

e.g.,

lon1 lat1 z1 lon2 lat2 z2 lon3 lat3 z3 u1 u2 u3 u1sig u2sig u3sig

-126.9202 48.4140 -5.242 -126.6596 48.0974 -5.223 -126.4634 48.5169 -8.575 -0.000 0.000 0.000 0.001 0.001 0.000

-121.2872 44.6730 -106.319 -121.2872 45.0089 -106.046 -121.6892 44.9196 -90.296 -0.000 0.000 0.000 0.001 0.001 0.000

where:

lon1,lat1,z1 – longitude, latitude, depth (km) of the first vertex of triangle patch

lon2,lat2,z2 – longitude, latitude, depth (km) of the 2nd vertex of triangle patch

lon3,lat1,z3 – longitude, latitude, depth (km) of the 3rd vertex of triangle patch

u1,u2,u3 – Dip-slip (normal "+"), strike-slip"("long-strike "+"), tensile component (opening "+") of slip vector at the center of triangle patch, Units: meters

u1sig, u2sig, u3sig – uncertainties of u1, u2, u3. Units, meters

evttag_slip.pdf: Plot of accumulated transient slip model with PNSN tremor locations (when available) (Figure 24b)

evttag_movie.avi: Movie of transient slip rate of ETS event with PNSN tremor locations (when available)

7.4 Status

A new set of displacements will be made available whenever a transient event is detected and analyzed and/or when newly updated time series solutions warrant the re-analysis. The latest is March to June, 2021. We plan to expand our transient products to other subduction zones beyond Cascadia, such as Japan, New Zealand and Costa Rica, depending on the addition of a sufficient number of stations in these regions.

8. Level 4: Horizontal strain rate grids

8.1 Background

Strain rate grids (fields/maps) are an important tool for crustal deformation studies. They reflect the buildup of elastic stress in the crust, are indicative of crustal rheology and aid in assessing earthquake hazards. Strain rate grids are independent of a reference frame since in its simplest representation a strain is a velocity between two-points divided by the distance between them. However, there are many ways to construct strain rate grids (UCERF3 2011; Sandwell et al., 2016) related to the interpolation and weighting method, underlying rheological assumptions and fault geometry. Typically, strain rate grids are constructed from steady-state geodetic velocities that are calculated over the interseismic period, wherein transients such as coseismic and postseismic deformation are nuisances and dealt with in various ways, through removal of observations over the affected time interval and/or modeling as we do as part of parametric time series analysis (section 2.1.4).

In our project, we are also focused on transient motions (see also ETS transients in the Western U.S. – section 7). We create strain rate grids based on weekly residual displacements relative to an underlying interseismic fault slip model (section 5) according to the methodology of Klein et al. (2019). Currently, we limit ourselves to the horizontal (2-D grids). We introduce the interseismic fault slip model for the Western U.S. (Zeng & Shen 2017) for better resolution or elastic deformation near faults for California and Nevada. In lieu of a fault-slip model, for Cascadia, we grid our estimated velocities (section 4.2). The strain rate product is constructed from the weekly residual displacement time series (observed minus predicted) as described in Klein et al. (2019). Figure 25 shows an example of residual displacement maps (vectors), interpolated displacement fields and maximum shear strain and dilatation rates.

8.2 Methodology

The horizontal strain rate tensor components are computed from the weekly residual velocity fields as follows:

$$\dot{\varepsilon}_{ij} = \frac{1}{2}\left(\frac{\partial v_i}{\partial x_j} + \frac{\partial v_j}{\partial x_i}\right) \tag{22}$$

The derivatives are calculated using the *grdgradient* function in GMT. From these velocity grids, we calculate the principal strain rates

$$\dot{\varepsilon}_{1,2} = \frac{\dot{\varepsilon}_{xx}+\dot{\varepsilon}_{yy}}{2} \pm \sqrt{\left(\frac{\dot{\varepsilon}_{xx}-\dot{\varepsilon}_{yy}}{2}\right)^2 + \dot{\varepsilon}_{xy}^2}\,, \tag{23}$$

the maximum shear strain rate

$$\dot{\varepsilon}_{12}^{MAX} = \frac{\dot{\varepsilon}_1 - \dot{\varepsilon}_2}{2} = \sqrt{\left(\frac{\dot{\varepsilon}_{xx} - \dot{\varepsilon}_{yy}}{2}\right)^2 + \dot{\varepsilon}_{xy}^2} \ , \tag{24}$$

and the dilatation rate

$$\delta = \dot{\varepsilon}_1 + \dot{\varepsilon}_2 = \dot{\varepsilon}_{xx} + \dot{\varepsilon}_{yy} \ . \tag{25}$$

8.3 Products

A series of files are created every week in parallel with the displacement grids and other weekly products. The files are stored on the SOPAC archive at:

http://garner.ucsd.edu/pub/measuresESESES_products/StrainRateGrids/

CDDIS file path: ~/GPS_Explorer/archive/StrainRateGrids/V1/YYYY/

Tar file: StrainRateGrids_yyyymmdd.tar.gz

Directory structure:

Tables >
ResRate_Zeng_YYYYMMDD.dat
Dilatation_YYYYMMDD.dat
MaxShearRate_YYYYMMDD.dat
SecularModelGrd >
rn_YYYYMMDD.grd -- north component of ResRate_Zeng in grid form
re_YYYYMMDD.grd -- east component of ResRate_Zeng in grid form
StrainRateGrd >
Dilatation_YYYYMMDD.pdf
Dilatation_YYYYMMDD.grd
SecondInvariant_YYYYMMDD.pdf
SecondInvariant_YYYYMMDD.grd
MaxShearRate_YYYYMMDD.pdf
MaxShearRate_YYYYMMDD.grd
RateTS >
WNAM_{YYYYMMDD of input time series}_WeekRateMod_tYYYY.YYYY.dat -- rates extracted from stations at each epoch
Movies (to be available, shortly)>
Dilatation_YYYYMMDD.mp4
MaxShearRate_YYYYMMDD.mp4
SecondInvariant_YYYYMMDD.mp4

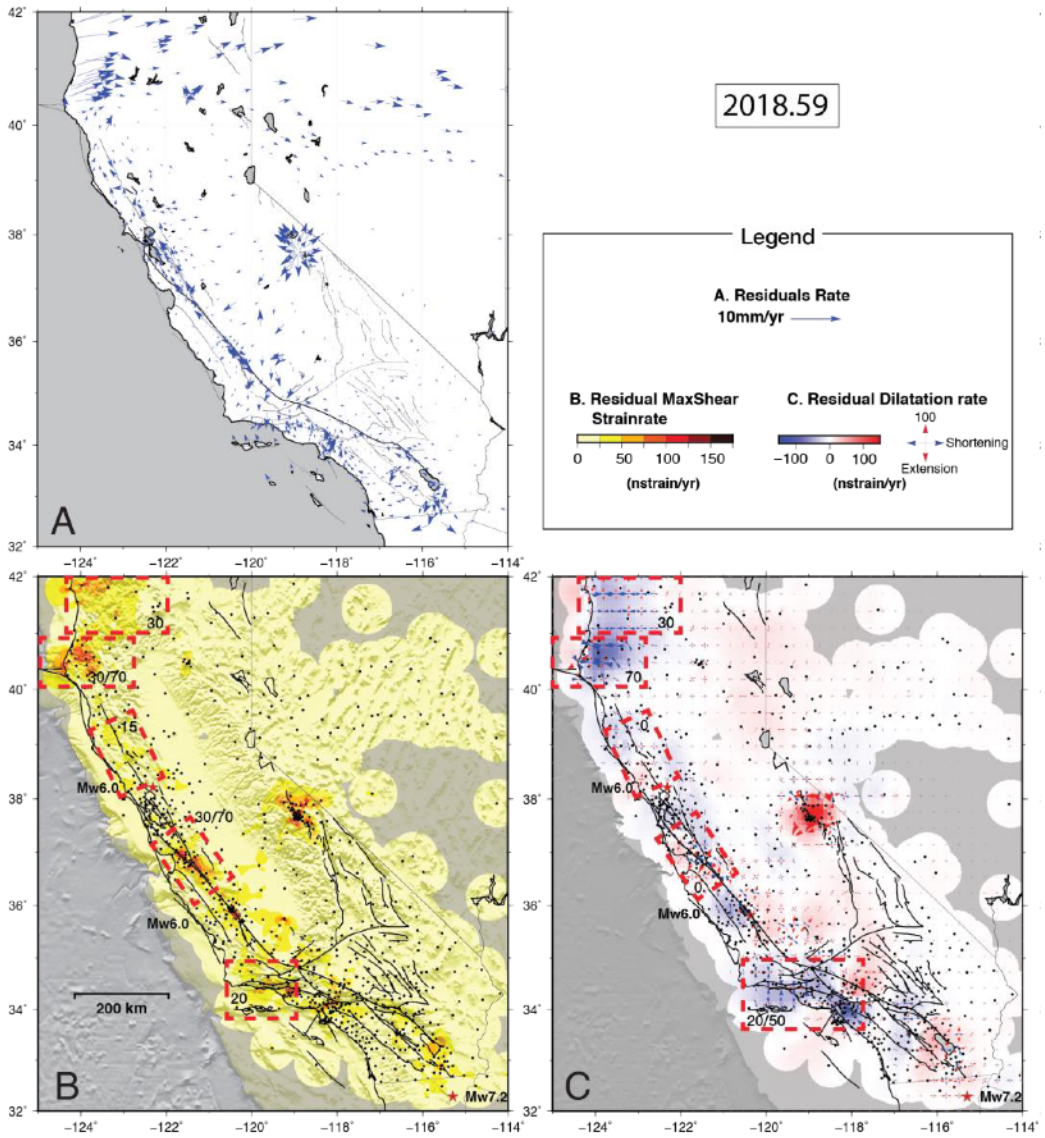

Figure 25. Residual maps and interpolated fields at epoch 2018.59. A) Velocity residual map (observed minus ZS2017-predicted); B) Maximum shear strain rate residual grids; C) Dilatation rate residual grids. Red vectors indicate extension, blue vectors indicate contraction. Areas of interest described are indicated by red dashed boxes including magnitudes. Values of strain rate are indicated for each area highlighted by a red contour. When important variations are observed, the mean and the maximum values ('mean/max') are given. For areas where strain rate is homogeneous, only the mean value is indicated. ZS2017 is the interseismic slip model of Zeng & Shen (2017). Source: (Klein et al., 2019).

9. Level 4 ESDR: Change in Total Water Storage Time Series

The capability to weigh mass change ’t Earth's surface with GPS is emerging as an excellent, effective technique to evaluate available water resources. Many studies have established that solid Earth responds elastically to changes in mass surface load, particularly in the vertical (Blewitt et al. 2001; Davis et al. 2004; Bevis et al. 2005; Tregoning et al. 2009; Nahami et al. 2012, Ouellette et al. 2013; Chew et al. 2014; Wahr et al. 2015). We and others have rigorously inferred changes in total water ’t Earth's surface as a function of location and time using elastic displacements of solid Earth (Argus et al. 2014, 2017; Borsa et al. 2014; Fu et al. 2015; Jin and Zhang 2016).

9.1 Background

9.1.1 Solid Earth's elastic response to a mass load

We will follow the method of Argus et al. (2017) to infer change in water as a function of time and location. Solid Earth’s elastic response to a point load is specified by u = m x GPS (θ), where u is vertical displacement ’f Earth's surface (in m) at an angular distance θ (in degrees) from the point load, m is the mass of the point load (in kg), and GPS is the Green's function (in m/kg), which depends on θ. We use the Green's functions for a gravitating, stratified PREM Earth (Wang et al. 2012b). Solid Earth's response to a surface mass load is tight in space. For a disk with a radius of 7 km, the vertical displacement at 20 km from the load center is half that at 10 km from the load center (Figure 26) (Wahr et al. 2015; Argus et al. 2014). The spatial resolution’ of GPS's determination of mass change is therefore high and limited only by the spacing of GPS sites. If a GPS array were to have a 10 km spacing, then GPS could determine mass change in individual watersheds and ice basins. We numerically integrate the Green's function to obtain a modified’ (Green's) function specifying solid Earth's elastic response to a disk load with a specific radius. We calculate many such modified’ (Green's) functions, varying the disk radius so that the disk area is equal to the area of a rectangular spherical cap bounded by specific latitude/longitude intervals.

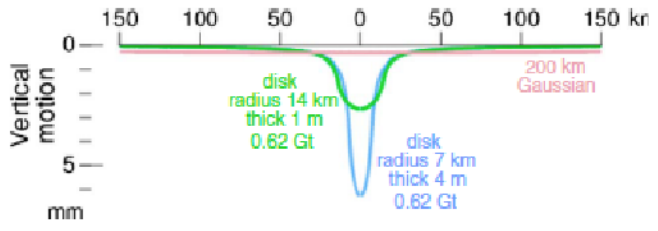

Figure 26. (Green curve) Vertical motion in elastic response to unloading of a disk with a radius of 14 km and a water thickness of 1 m. This disk has the same area as a pixel at 36°N that we estimate water thickness for (1/4° latitude by 1/4° longitude). (Blue curve) Vertical motion in elastic response to unloading of a disk with a radius of 7 km and a water thickness of 4 m. This disk has the same area as 1 NLDAS pixel at 36°N (1/8° latitude by 1/8° longitude). The Green’s functions for PREM are used (Wang et al., 2012b). (Pink curve) Vertical motion that would be inferred by GRACE is approximated by a Gaussian distribution with a halfwidth of 200 km. “Gt” is gigatons (10^{12} kg).

9.1.2 Sustained changes in water in the ground during alternating periods of drought and heavy precipitation

GPS is providing striking new constraints on hydrology. Using GPS measurements of solid Earth's elastic displacement, Argus et al. (2017) quantify change in total water in three California mountains provinces (the Sierra Nevada, the Klamath mountains, and the Coast Ranges). In the western U.S., snow falls and accumulates on the ground in the fall and winter, then melts in the spring and summer, leaving negligible snow in October. Argus et al. (2017) thus quantify change in water in the ground by taking differences between successive Octobers. Argus et al. (2017) find California's three mountain provinces to have lost 97 km^3 of during the four years of harsh California drought from Oct 2011 to 2015, exceeding by a factor of five the 18 km^3 of water lost in a composite hydrology model (Figure 27). We find the three mountain provinces to have gained 51 km^3 of water in the ground during two years of heavy precipitation from Oct 2015 to Oct 2017.

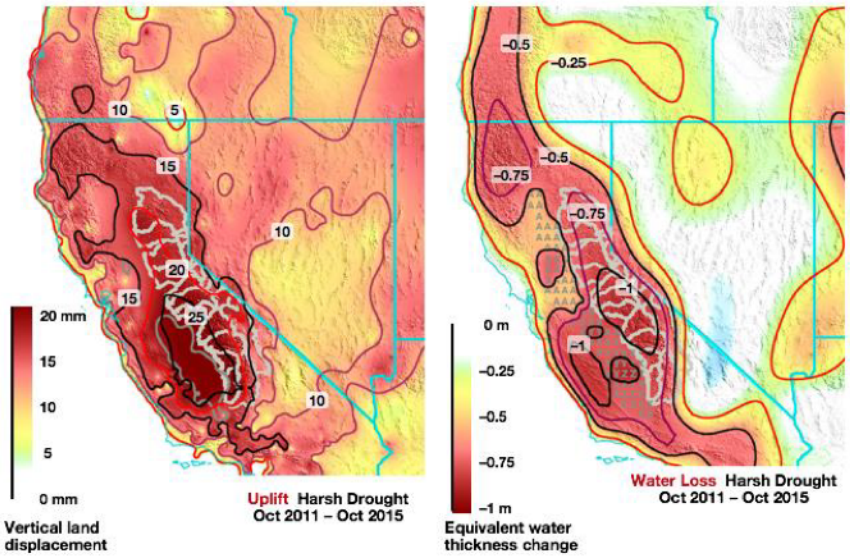

Figure 27. (Left) Vertical land displacement observed with GPS is inverted to infer (Right) change in total water during harsh drought from Oct 2011 to Oct 2015. At left, the vertical displacement field is determined using only GPS sites recording solid Earth's elastic response to water change; GPS sites in Central Valley subsiding in porous response to groundwater loss are excluded. At right, groundwater loss in Central Valley is assumed to be to 34 km^3 in the inversion; groundwater loss at 1/4° pixels (small gray letters) are set equal to –1.64 m (Z's), –1.23 m (Y's), –0.82 m (X's), and –0.41 m (A's). Because snow accumulation in California is insignificant in October, we infer all water change from Oct to Oct to be in the ground. During the four years of drought, the Sierra Nevada mountains lost an average of 0.66 m of water in the ground, for a total loss of 45 km^3. The Sierra Nevada, Klamath mountains, and Coast Ranges loss an average of 0.51 m of water in the ground, for a total loss of 97 km^3, far exceeding the 18 km^3 of water lost in a composite hydrology model. From Argus et al. (2017).

In summary, we are finding that in California's mountains more water in the ground is lost during drought and gained in heavy precipitation than in the hydrology models. The sustained changes in water cannot result from snow because snow accumulation is negligible in October. Either changes in soil moisture in the ground are far understated in the hydrology models or there are large changes in groundwater in river alluvium, pastures, and fractured crystalline basement that is not in the hydrology models. The ground must have a greater capacity to store water than previously believed.

9.2 Methodology

We will infer **changes in total water storage ’t Earth's surface** following a sequence of 10 carefully constructed and practiced steps following the techniques in Argus et al. (2017).

2. Carefully analyze all series of GNSS positions; identify all offsets due to antenna substitutions, earthquakes, and other phenomena; identify postseismic transients that are clearly associated in time and space with earthquakes; construct series of GNSS displacements of more than five years passing through January 2012 (by eliminating data after offsets occurring after Jan 2012 and data before offsets occurring before 2012.
3. Distinguish between GNSS sites primarily recording solid Earth's elastic response to mass changes; solid Earth's porous response to groundwater and oil changes; and solid Earth's response to magma changes in volcanoes.
4. Remove solid Earth's elastic response to changes in the atmosphere and non-tidal changes in the ocean.
5. Remove solid Earth's elastic response to known changes in surface water in artificial reservoirs and large lakes.
6. Remove interseismic strain accumulation produced by locking of the Cascadia subduction zone. Remove displacements produced by slow slip events occurring along the Cascadia megathrust.
7. Remove solid Earth's viscous response to unloading of the late Pleistocene ice sheets.
8. Transform Earth's reference frame into the frame minimizing differences between observations of vertical displacements and predictions from a postglacial rebound model. The velocity ’f Earth's mass center (CM) estimates using SLR observations of satellite LAGEOS is somewhat uncertain; We maintain that this transformation into the soli’ Eartha's mass center (CE) results in more accurate estimates of vertical displacement (Argus 2007, 2012; Argus et al. 2014; Riddell et al. 2017).
9. Constrain total water change outside the western United States area for which water change is being estimated to be that inferred from GRACE.
10. Constrain groundwater change in California’s Central Valley to an a priori hydrological model (Faunt et al. 2015; Xiao et al. 2017).
11. Invert for changes in total water storage **(“water.gps”)** as a function of posi¼n at 1/4° intervals of latitude and longitude each month from Jan 2006 to the Present. Solid Earth's elastic response to a surface mass load is nearly known if the surface load is more than about 50 km across (Wahr et al. 2013; Argus et al. 2014b, 2017). Apply Laplacian regularization to limit water changes between adjacent pixels. Estimate uncertainty using linear propagation of errors on the basis of a realistic error budget.

9.3 Products

Changes in components of water storage are archived in seven text files. The first two columns in each file are latitude and longitude. The third column is the value of the product and the fourth column is uncertainty (units of mm).

(1) Change in total water storage inferred from GPS – "water.gps"
(2) Change in equivalent water thickness – "atmosphere"
(3) Change in snow water equivalent (SWE) – "snow"
Snow depth and snow water equivalent (SWE) data are available from NOAA's National Weather Service's National Operational Hydrologic Remote Sensing Center (NOHRSC) SNOw Data Assimilation System (SNODAS). https://nsidc.org/data/g02158
(4) Change in soil moisture content (SMC) – "soil"
NLDAS_NOAH is a monthly climatology data set contains a series of land surface parameters, including Soil Moisture Content (SMC), simulated from the Noah land-surface model (LSM) for Phase 2 of the North American Land Data Assimilation System (NLDAS-2).
https://disc.gsfc.nasa.gov/datasets/NLDAS_NOAH0125_MC_V002/summary
(5) Change in artificial reservoir surface water – "reservoir"
These hydrological data are from the California Data Exchange Center (CDEC) Weather Gauging Stations, including automatic snow reporting gages for the Cooperative Snow Surveys Program and precipitation and river stage sensors for flood forecasting.
https://www.calfish.org/ProgramsData/ReferenceLayersNaturalResources/(CDEC)WeatherGagingStations.aspx
(6) Change in total mass – "mass"
Total mass = water.gps + reservoir + atmosphere
(7) Change in water in the ground not in hydrology models – "ground"
Inferred to be water.gps–- snow - soil moisture

Note: Check if accurate: The start date for the water storage products is taking zero to be 1 Jan 2012, about halfway through the time series (circa May 2020). The start time will be modified to 1 Jan 2013 as the series lengthens.

9.4 Directory Structure

CDDIS Product Name: water_storage

CDDIS file path: ~/GPS_Explorer/archive/WaterStorage/YYYY.yyy_YYYY.yyy/

Only first one (combwm) is sent to CDDIS.

/GPS_Explorer/archive/WaterStorage/YYYY.yyy_YYYY.yyy-combg/

/GPS_Explorer/archive/WaterStorage/YYYY.yyy_YYYY.yyy-jpl/

/GPS_Explorer/archive/WaterStorage/YYYY.yyy_YYYY.yyy-sio/

Note: Check CDDIS links above

WaterStorage_yyyymmdd.tar.gz (yyyymmdd indicates date that tar file was archived)

SOPAC archive directory:
http://garner.ucsd.edu/pub/measuresESESES_products/WaterStorage
Example:
http://garner.ucsd.edu/pub/measuresESESES_products/WaterStorage/2006.042_2021.458-combwm/

2006.042_2021.458: data set denoted by start and end dates in decimal years
Extensions (time series source):
-jpl
-sopac
-combwm (weighted mean combination)
-combg (GLOBK combination)

In water storage directories:
readme.txt (update header when new product is ready to upload to JPL – source and tar file names), e.g.,

```
NASA MEaSUREs ESESES Project
Water Storage: Level 4 products
Source: Weighted Mean Combination of JPL and SOPAC solutions:
WNAM_Clean_TrendNeuTimeSeries_combwm_20210810.tar;
GLB_Clean_TrendNeuTimeSeries_combwm_20210810.tar
August 29, 2021 (date when archived)
```

atmosphere
ground
mass
reservoir
snow
soil
water.gps

The WaterStorage directories (atmosphere, ground, etc.) contain daily files named by decimal year. Formats described in readme.txt and section 9.3.

9.5 Data Grids

Note: In progress
Data Grids

Illustrations will be made each month of Water Year 2020, with zero being October 2019, to show water storage growing through the rainy Autumn and Winter.

1. Oct 2019 to Oct 2018 would quantify water change over Water Year 2019.
2. Oct 2019 to Feb 2020 would quantify water change to date over the current year.
3. Water change from Oct 2011 to Oct 2015 quantifies water change over the four years of harsh drought. Identical to the figure in Argus et al. 2017 and similar to that in the project logo.
4. Water change (to this month in that year) in a heavy precipitation year.
5. Water change (to this month in that year) in a drought year.

9.6 Status

Updated every 3 months.

10. Web Presence

10.1 MEaSUREs Web Pages

The project logo and web pages are found at http://sopac-csrc.ucsd.edu/index.php/measures-2/. An ESESES page at CDDIS directs users to our products located there, https://cddis.nasa.gov/Data_and_Derived_Products/GNSS/MEaSUREs_products.html.

10.2 MGViz

The primary web interface to our ESDRs has shifted from GPS Explorer to the MEaSUREs GNSS Visualizer (MGViz) (Figures 28 and 29) (http://mgviz.ucsd.edu/?mission=ESESES), which is based on the Multi-Mission Geographic Information System (MMGIS), previously developed at JPL to localize and visualize Mars mission science instrument data. This transition recognizes that due to evolution of technology over the past 15 years, GPS Explorer's underlying portlet-based framework (GridSphere) has reached end of life, and Java time series applet support is unavailable in many browsers.

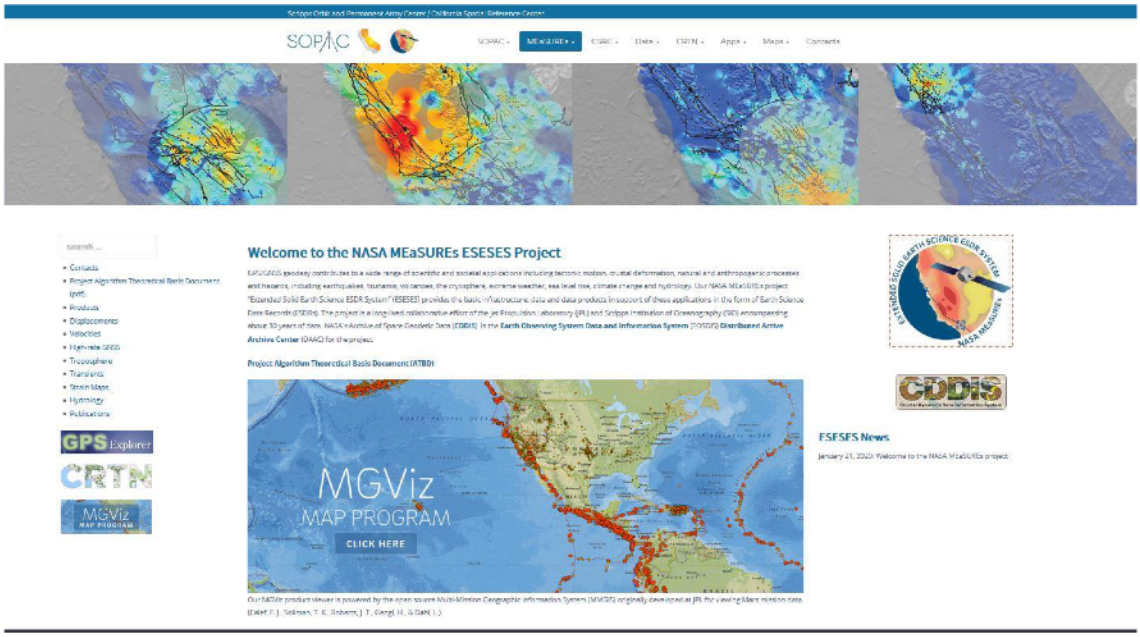

Figure 28. Screen shot of the MEaSUREs web home page

MGViz has been approved by JPL as open source and is available for download in the NASA Advanced Multi-Mission Operations System repository (https://github.com/NASA-AMMOS). It is now installed on a server at SOPAC. The GPS Explorer portal continues to provide the interactive interface for the administrator time series functions (section 2).

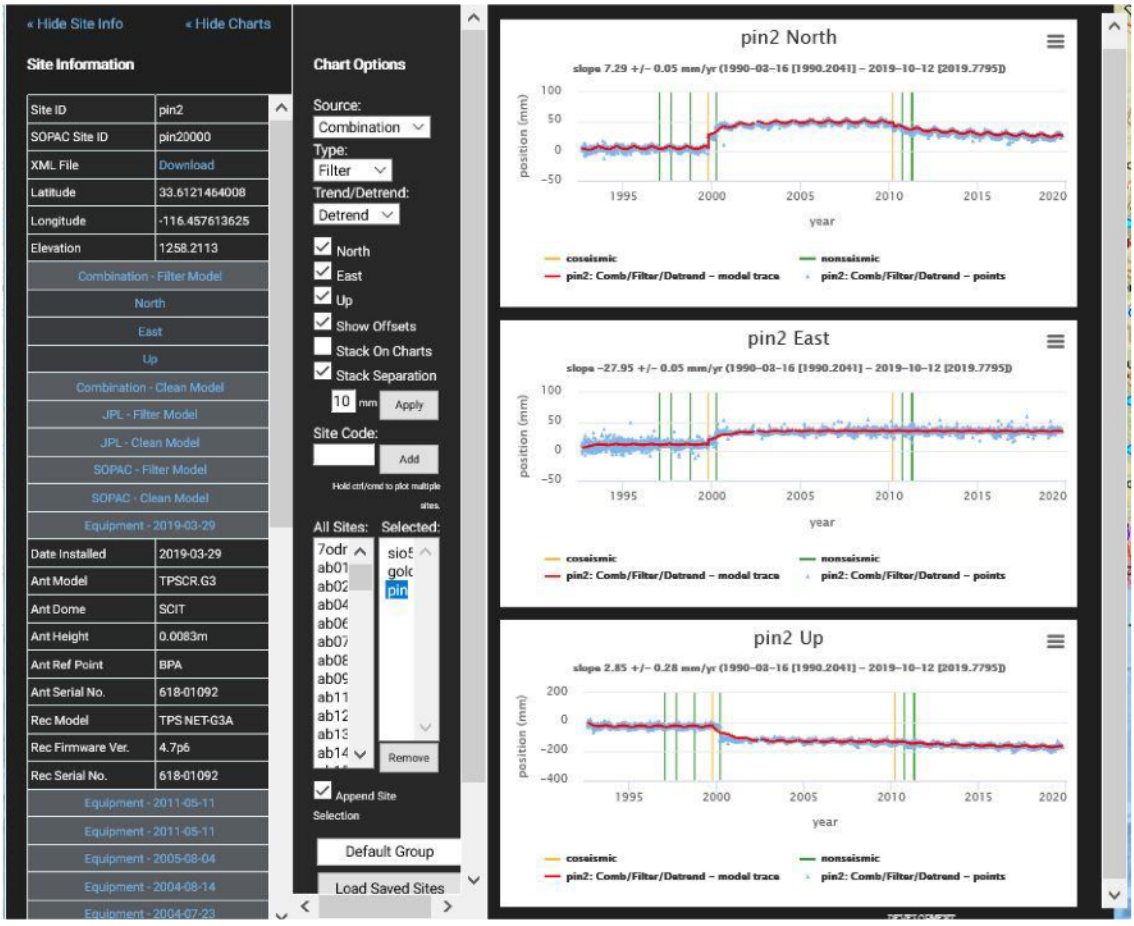

Figure 29. Screen shot of our new interactive interface, MGViz, showing the estimated (L1C) detrended combination time series for one of our long-lived station PIN2 showing the coseismic and postseismic effects of two events – the 1999 Mw7.2 Hector Mine and 2010 Mw7.2 El Mayor-Cucapah earthquakes. The far-left panel shows the relevant data for that station. The next panel shows the different time series options available to the user. http://mgviz.ucsd.edu/?mission=ESESES (section 10.2)

10.3 Events Page

Note: We are in the process of creating event pages. For example, we responded to the July 2019 Mw6.2 and Mw7.1 earthquakes near Ridgecrest, California by estimating coseismic offsets (Figure 30) and subsequent postseismic deformation. In this case, we split the 24-hour period into pre- and post-earthquake data. Initially, we thought that about 100 stations had significant permanent coseismic offsets (Figure 30). Further, we determined that more than 50 additional stations were affected extending throughout the Los Angeles basin. Furthermore, for this L1C ESDR we estimated and archived the coseismic (dynamic and static) motions of the event itself (Figure 31). We created an event page for this earthquake sequence (http://sopac-csrc.ucsd.edu/index.php/ridgecrestjuly2019/).

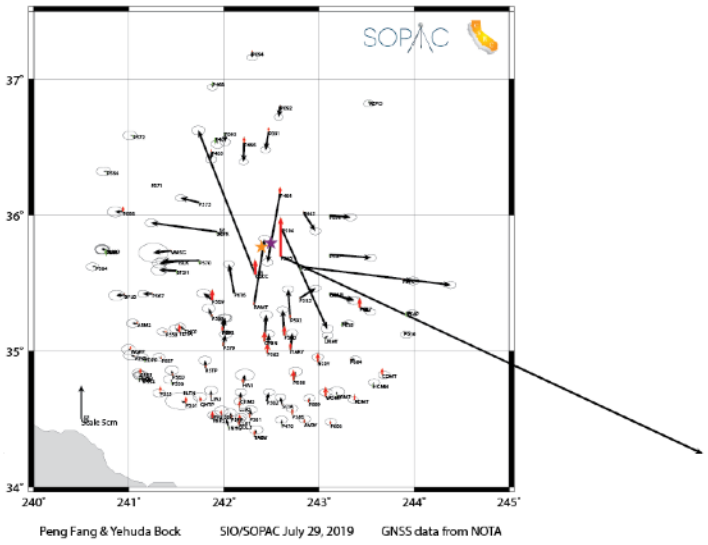

Figure 30. Total coseismic displacements at about 100 stations for the Mw6.4 and Mw7.1 earthquakes on July 4, 2019 estimated by SIO – the coseismic offsets were also estimated by JPL. Our combination time series provides a more accurate estimate of coseismic displacements for about 150 stations.

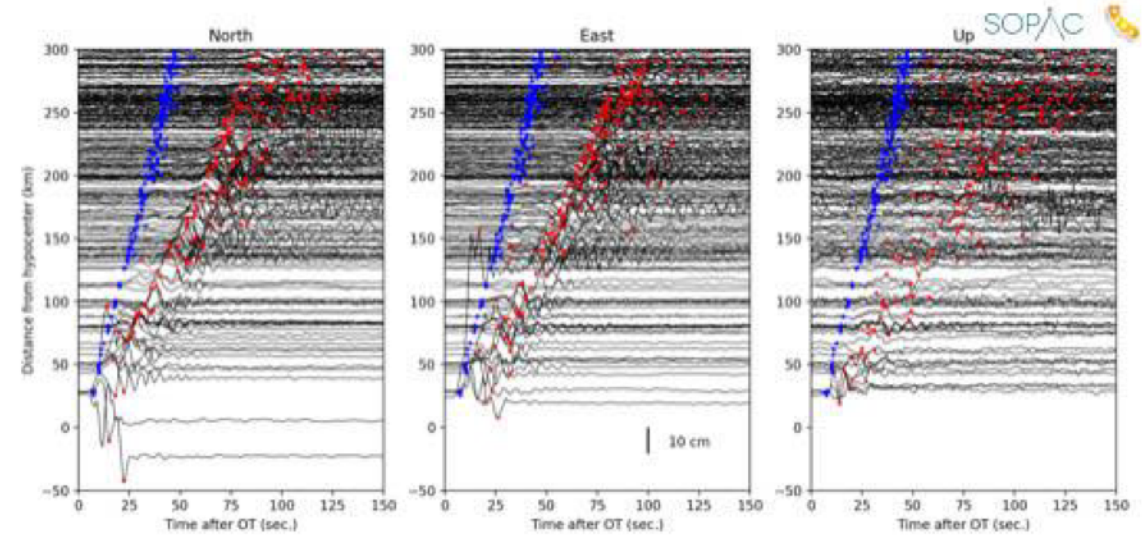

Figure 31. 1 Hz displacement waveforms as a function of distance from the July 6, 2019 Mw7.1 Ridgecrest earthquake's epicenter. The blue dots represent P-wave arrivals. The red dots denote peak ground displacements.

References

Agnew, D. C. (2012). SPOTL: Some programs for ocean-tide loading, Scripps Institution of Oceanography Technical Report, August 31, 2013.

Altamimi, Z., P. Rebischung, L. Métivier, and X. Collilieux (2016), ITRF2014: A new release of the International Terrestrial Reference Frame modeling nonlinear station motions, Journal of Geophysical Research: Solid Earth, 121: 6109-31.

Argus, D.F., Landerer, F.W., Wiese, D.N., Martens, H.R., Fu, Y., Famiglietti, J.S., Thomas, B.F., Farr, T.G., Moore, A.W. and Watkins, M.M. (2017), Sustained water loss in California's mountain ranges during severe drought from 2012 to 2015 inferred from GPS, Journal of Geophysical Research: Solid Earth, 122. https://doi.org/10.1002/2017JB014424.

Argus, D. F. (2007), Defining the translational velocity of the reference frame of Earth. Geophysical Journal International, 169(3), 830–838. https://doi.org/10.1111/j.1365-246X.2007.03344.x

Argus, D. F. (2012), Uncertainty in the velocity between the mass center and surface of Earth. Journal of Geophysical Research, 117, B10405, https://doi.org/10.1029/2012JB009196

Argus, D. F., Peltier, W. R., Drummond, R., & Moore, A. W. (2014), The Antarctica component of postglacial rebound model ICE-6G_C (VM5a) based on GPS positioning, exposure age dating of ice thicknesses, and relative sea level histories. Geophysical Journal International, 198(1), 537–563. https://doi.org/10.1093/gji/ggu140

Argus, D. F., Y. Fu and F. W. Landerer (2014b), Seasonal variation in total water storage in California inferred from GPS observations of vertical land motion, Geophysical Research Letters 41(6): 1971-1980. https://doi.org/10.1002/2014GL059570

Barbot, S., Y. Fialko, and Y. Bock (2009), Postseismic deformation due to the Mw 6.0 2004 Parkfield earthquake: Stress-driven creep on a fault with spatially variable rate-and-state friction parameters, J. Geophys. Res., 114, B07405. http://dx.doi.org/10.1029/2008JB005748

Bar-Sever, Y., Bertiger, W., Davis, E., and Anselmi, J. (1996). Fixing the GPS Bad Attitude: Modeling GPS satellite yaw during eclipse season. Navigation, 43(1):25-39.

Bar-Sever, Y. E., P. M. Kroger, and J. A. Borjesson (1998), Estimating horizontal gradients of tropospheric path delay with a single GPS receiver, J. Geophys. Res., *103*(B3), 5019–5035.

Bartlow, N. M., S. Miyazaki, A. M. Bradley, and P. Segall (2011), Space-time correlation of slip and tremor during the 2009 Cascadia slow slip event, Geophys. Res. Lett., 38, L18309, https://doi.org/10.1029/2011GL048714

Bartlow, N.M., L. M. Wallace, R. J. Beavan, S. Bannister, and P. Segall (2014), Time-dependent modeling of slow slip events and associated seismicity and tremor at the Hikurangi subduction zone, New Zealand, J. Geophys. Res. Solid Earth, 119, 734–753. https://doi.org/10.1002/2013JB010609

Beroza, G.C. and Ide, S. (2011), Slow earthquakes and nonvolcanic tremor, Annual Review of Earth and Planetary Sciences, 39: 271–296. https://doi.org/10.1146/annurev-earth-040809-152531

Bertiger, W., S. D. Desai, B. Haines, N. Harvey, A.W. Moore, S. Owen, and J. P Weiss (2010), Single receiver phase ambiguity resolution with GPS data, Journal of Geodesy, 84: 327-37.

Bevis, M., S. Businger, S. Chiswell, T. A. Herring, R. A. Anthes, C. Rocken and R. H. Ware (1994), GPS meteorology: Mapping zenith wet delays onto precipitable water, Journal of applied meteorology 33(3): 379-386.

Bletery, Quentin, Anthony Sladen, Bertrand Delouis, Martin Vallée, Jean-Mathieu Nocquet, Lucie Rolland, and Junle Jiang (2014), A detailed source model for the Mw9. 0 Tohoku-Oki earthquake reconciling geodesy, seismology, and tsunami records, Journal of Geophysical Research: Solid Earth, 119: 7636-53.

Blewitt, G. (2008), Fixed point theorems of GPS carrier phase ambiguity resolution and their application to massive network processing: Ambizap, J. Geophys. Res., 113, B12410.

Bock, Y. & D. Melgar (2016), Physical Applications of GPS Geodesy: A Review, Rep. Prog. Phys. 79, 10, doi:10.1088/0034-4885/79/10/106801

Bock, Y. & S. Wdowinski (2020), GNSS Geodesy in Geophysics, Natural Hazards, Climate, and the Environment, in Position, Navigation, and Timing Technologies in the 21st Century: Integrated Satellite Navigation, Sensor Systems, and Civil Applications, IEEE, 2021, 741-820.

Bock, Y., D. Melgar, B. W. Crowell (2011), Real-Time Strong-Motion Broadband Displacements from Collocated GPS and Accelerometers, Bulletin Seismological Society of America, 101, 2904-2925. https://doi.org/10.1785/0120110007.

Bock Y., S. Wdowinski, P. Fang, J. Zhang, S. Williams, H. Johnson, J. Behr, J. Genrich, J. Dean, M. van Domselaar, D. Agnew, F. Wyatt, K. Stark, B. Oral, K. Hudnut, R. King, T. Herring, S. DiNardo, W. Young, D. Jackson, and W. Gurtner (1997), Southern California Permanent GPS Geodetic Array: Continuous measurements of crustal deformation between the 1992 Landers and 1994 Northridge earthquakes, J. Geophys. Res., 102, 18,013-18,033.

Bock, Y., D. Melgar, B. W. Crowell (2011), Real-Time Strong-Motion Broadband Displacements from Collocated GPS and Accelerometers, Bull. Seismol. Soc. Am., 101, 2904-2925, doi: 10.1785/0120110007.

Bock, Y., L. Prawirodirdjo, and T. I. Melbourne (2004), Detection of arbitrarily large dynamic ground motions with a dense high-rate GPS network, Geophys. Res. Lett., 31, L06604, doi:10.1029/2003GL019150.

Bock, Y. and D. Melgar (2016), Physical Applications of GPS Geodesy: A Review, Rep. Prog. Phys. 79, 10, doi:10.1088/0034-4885/79/10/106801.

Bock, Y., Fang, P. & Helmer, G.R. (2018). California Spatial Reference System CSRS Epoch 2017.50 (NAD83), Report to the California Department of Transportation (http://sopac-csrc.ucsd.edu/index.php/epoch2017/).

Bock, Y. & S. Wdowinski (2020), GNSS Geodesy in Geophysics, Natural Hazards, Climate, and the Environment, in Position, Navigation, and Timing Technologies in the 21st Century: Integrated Satellite Navigation, Sensor Systems, and Civil Applications, IEEE, 2021, 741-820, doi: 10.1002/9781119458449.ch28.

Boehm, J., A. Niell, P. Tregoning and H. Schuh (2006), Global Mapping Function (GMF): A new empirical mapping function based on numerical weather model data, Geophysical Research Letters 33(7).

Boehm, J., Werl, B., & Schuh, H. (2006). Troposphere mapping functions for GPS and very long baseline interferometry from European Centre for Medium-Range Weather Forecasts operational analysis data. *Journal of Geophysical Research: Solid Earth*, *111*(B2).

Crowell, B. W., Y. Bock, and M. Squibb (2009), Demonstration of earthquake early warning using total displacement waveforms from real time GPS networks, Seismo. Res. Lett., 80(5), 772-782.

Crowell, B. W., Y. Bock and D. Melgar (2012), Real-time inversion of GPS data for finite fault modeling and rapid hazard assessment, Geophys. Res. Lett., 39, L09305.

Crowell, B., Y. Bock, Z. Liu (2016), Single-station automated detection of transient deformation in GPS time series with the relative strength index: A case study of Cascadian slow-slip, J. Geophys. Res., 121.

Davis J., T. Herring, I. Shapiro, A. Rogers and G. Elgered (1985), Geodesy by radio interferometry: effects of atmospheric modeling errors on estimates of baseline length Radio Sci. 20 1593–607.

Davis, J. P, and R. Smalley (2009), Love wave dispersion in central North America determined using absolute displacement seismograms from high-rate GPS, Journal of Geophysical Research: Solid Earth, 114.

Dixon, T. H., Y. Jiang, R. Malservisi, R. McCaffrey, N. Voss, M. Protti, V. Gonzalez (2014), Earthquake and tsunami forecasts: relation of slow slip events to subsequent earthquake rupture, PNAS, 111(48), 17039-17044.

Dong, D. N. and Y. Bock (1989), Global Positioning System network analysis with phase ambiguity resolution applied to crustal deformation studies in California, *J. Geophys. Res.*, *94*, 3949-3966.

Dong, D., P. Fang, Y. Bock, F. Webb, L. Prawirodirdjo, S. Kedar, and P. Jamason (2006), Spatiotemporal filtering using principal component analysis and Karhunen-Loeve expansion approaches for regional GPS network analysis, J. Geophys. Res., *111*, B03405.

Dong et al. (co-authors) (1998), Estimating regional deformation from a combination of space and terrestrial geodetic data, Jour. Geod., *72*, 200-214.

Dow, J.M., R.E. Neilan, G. Gendt (2005), "The International GPS Service (IGS): Celebrating the 10th Anniversary and Looking to the Next Decade," Adv. Space Res, 36, no. 3, pp. 320-326.

Dragert H., K. Wang, T. S. James (2001), A silent slip event on the deeper Cascadia subduction interface. Science, 292(5521), 1525-1528.

Emore, Gordon L, Jennifer S Haase, Kyuhong Choi, Kristine M Larson, and Atsushi Yamagiwa (2007), Recovering seismic displacements through combined use of 1-Hz GPS and strong-motion accelerometers, Bulletin of the Seismological Society of America, 97: 357-78.

Faunt, C. C., Sneed, M., Traum, J., & Brandt, J. T. (2015). Water availability and land subsidence in the Central Valley, California, USA (2015). Hydrogeology Journal, 24(3), 675–684.

Feigl, K. L., R. W. King, T. H. Jordan (1990), Geodetic Measurement of Tectonic Deformation in the Santa Maria Fold and Thrust Belt, California, J. Geophys. Res., 95, B3, 2679-2699.

Freed, A. M. (2007). Afterslip (and only afterslip) following the 2004 Parkfield, California, earthquake, Geophysical Research Letters, 34.

Fu, Y., Z. Liu, J. Freymueller (2015), Spatiotemporal variations of the slow slip event between 2008 and 2013 in the southcentral Alaska subduction zone, Geochemistry, Geophysics, Geosystems, 2450-2461.

Genrich, J. F. and Y. Bock (2006), Instantaneous geodetic positioning with 10-50 Hz GPS Measurements: Noise characteristics and implications for monitoring networks, J. Geophys. Res., 111, B03403.

Goldberg, D., Y. Bock (2017), Self-contained local broadband seismogeodetic early warning system: Detection and location, J. Geophys. Res. Solid Earth, 122(4), 3197-3220, https://doi.org/10.1002/2016JB013766 .

Golriz, D, Y. Bock & X. Xu (2021), Defining the Coseismic Phase of the Crustal Deformation Cycle with Seismogeodesy, J. Geophys. Res.: Solid Earth, 126, e2021JB022002. https://doi.org/10.1029/2021JB022002

Grapenthin, R. and J. T. Freymueller (2011), The dynamics of a seismic wave field: Animation and analysis of kinematic GPS data recorded during the 2011 Tohoku-oki earthquake, Japan, Geophysical Research Letters, 38.

Ji, Chen, Kristine M Larson, Ying Tan, Kenneth W Hudnut, and Kyuhong Choi (2004), Slip history of the 2003 San Simeon earthquake constrained by combining 1-Hz GPS, strong motion, and teleseismic data, Geophysical Research Letters, 31: L17608.

Klein, K., Y. Bock, X. Xu, D. Sandwell, D. Golriz, P. Fang, L. Su (2019), Transient deformation in California from two decades of GPS displacements: Implications for a three-dimensional dynamic reference frame, Journal Geophysical Research, *124*(11), 12189-12223. https://doi.org/10.1029/2018JB017201.

Kobayashi, R., S. Miyazaki, and K. Koketsu (2006), Source processes of the 2005 West Off Fukuoka Prefecture earthquake and its largest aftershock inferred from strong motion and 1-Hz GPS data, Earth, Planets, and Space, 58: 57-62.

Kouba, J. (2003), Measuring seismic waves induced by large earthquakes with GPS, Studia Geophysica et Geodaetica, 47: 741-55.

Kouba, J. and P. Héroux (2001), Precise point positioning using IGS orbit and clock products, GPS Solutions, 5: 12-28.

Herring, T. A., R. W. King, and S. C., McClusky (2018), GAMIT Reference Manual release 10.70, MIT (http://geoweb.mit.edu/gg/).

Jin, S., and T. Zhang (2016), Terrestrial water storage anomalies associated with drought in the southwestern USA from GPS observations, Surv. Geophys., 37:1139-1156, https://link.springer.com/article/10.1007/s10712-016-9385-z.

Ide, S., Beroza, G. C., Shelly, D. R., & Uchide, T. (2007), A scaling law for slow earthquakes. Nature, 447(7140), 76. https://doi.org/10.1038/nature05780

Langbein, J. (2008), Noise in GPS displacement measurements from Southern California and Southern Nevada. Journal of Geophysical Research: Solid Earth, 113(B5).

Langbein, J., R. Borcherdt, D. Dreger, J. Fletcher, J. L. Hardebeck, M. Hellweg, C. Ji, M. Johnston, J. R. Murray, and R. Nadeau (2005), Preliminary report on the 28 September 2004, M 6.0 Parkfield, California earthquake, Seismological Research Letters, 76: 10-26.

Larson, K. M., P. Bodin, and J. Gomberg (2003), Using 1-Hz GPS data to measure deformations caused by the Denali fault earthquake, Science, 300: 1421-24.

Liu, Z., S. Owen, D. Dong, P. Lundgren, F. Webb, E. Hetland, M. Simons (2010), Integration of transient strain events with models of plate coupling and areas of great earthquakes in southwest Japan, 181, 1292-1312, Geophys. J. Int., https://doi.org/10.1111/j.1365-246X.2010.04599.x .

Liu, Z., D. Dong and P. Lundgren (2011), Constraints on time-dependent volcanic source models at Long Valley Caldera from 1996 to 2009 using InSAR and geodetic measurements, Geophysical Journal International 187(3): 1283-1300.

Liu, Z., A. Moore, S. Owen (2015a), Recurrent slow slip event reveals the interaction with seismic slow earthquakes and disruption from large earthquake, Geophys. J. Int., 202, 1555-1565, https://doi.org/10.1093/gji/ggv238.

Liu, Z., Y. Fu, Y. Bock, Y. Jiang, A. Moore, S. Owen, S. Kedar (2015b), Investigate the Spatiotemporal Relationship Between Slow Slip Transients and Tremor in Cascadia Subduction Zone, S31A-2719, 2015 AGU Fall Meeting.

Lohman, R. B., and J. J. McGuire (2007), Earthquake swarms driven by aseismic creep in the Salton Trough, California, J. Geophys. Res., 112, B04405. https://doi.org/10.1029/2006JB004596

McGuire, J. & Segall, P. (2003), Imaging of aseismic fault slip transients recorded by dense geodetic networks, Geophys. J. Int., 155, 778– 788

Melgar, D., B. W. Crowell, Y. Bock, and J. S. Haase (2013), Rapid modeling of the 2011 Mw 9.0 Tohoku-oki earthquake with seismogeodesy, Geophys. Res. Lett., 40, 1-6. https://doi.org/10.1002/grl.50590

Melgar, D., B. W. Crowell, J. Geng, R. M. Allen, Y. Bock, S. Riquelme, E. M. Hill, M. Protti, A. Ganas (2015), Earthquake Magnitude Calculation without Saturation from the Scaling of Peak Ground Displacement, *Geophys. Res. Lett. 42* (13), 5197-5205. https://doi.org/10.1002/2015GL064278

Melgar, D., R. M. Allen, S. Riquelme, J. Geng, F. Bravo, J. Carlos Baez, H. Parra, S. Barrientos, P. Fang, Y. Bock, M. Bevis, D. J. Caccamise, C. Vigny, M. Moreno and R. Smalley Jr. (2016), Local Tsunami Warnings: Perspectives from Recent Large Events, Geophys. Res. Lett., 43, 1109–1117. https://doi.org/10.1002/2015GL067100

Miyazaki, Shin-ichi, Kristine M Larson, Kyuhong Choi, Kazuhito Hikima, Kazuki Koketsu, Paul Bodin, Jennifer Haase, Gordon Emore, and Atsushi Yamagiwa (2004), Modeling the rupture process of the 2003 September 25 Tokachi-Oki (Hokkaido) earthquake using 1-Hz GPS data, Geophysical Research Letters, 31.

Miyazaki, S., Segall, P., McGuire, J.J., Kato, T.& Hatanaka, Y. (2006), Spatial and temporal evolution of stress and slip rate during the 2000 Tokai slow earthquake, J. Geophys. Res., 111, B03409. https://doi.org/10.1029/2004JB003426

Moore, A.W., I. J. Small, S. I. Gutman, Y. Bock, J. L. Dumas, P. Fang, J. S. Haase, M. E. Jackson, J. L. Laber (2015), National Weather Service Forecasters Use GPS Precipitable Water Vapor for Enhanced Situational Awareness during the Southern California Summer Monsoon, Bull. Amer. Meteorol. Soc. (BAMS) 96(11), 1867-1877. DOI:10.1175/BAMS-D-14-00095.1

Nikolaidis, R. (2002). Observation of geodetic and seismic deformation with the Global Positioning System, PhD thesis, University of California, San Diego.

Nilsson, T. and Elgered, G. (2008), Long-term trends in the atmospheric water vapor content estimated from ground-based GPS data. Journal of Geophysical Research: Atmospheres, 113(D19).

Noll, C., Y. Bock, H. Habrich, and A. Moore (2009), Development of data infrastructure to support scientific analysis for the International GNSS Service, J. Geod., 83, 309–325. doi:10.1007/s00190-008-0245-6

Ozawa, S., H. Suito, T. Imakiire, M. Murakami (2007), Spatio-temporal evolution of interplate slip between 1996 and 1998 and between 2002 and 2004, in Bungo Channel, southwest Japan, J. Geophys. Res., 112, B05409, doi: 10.1029/2006JB004643.

Petit G. and B. Luzum (2010), IERS technical note No. 36, IERS conventions (2010) Int. Earth Rotation and Reference Systems Service.

Peng Z., J. Gomberg (2010), An integrated perspective of the continuum between earthquakes and slow-slip phenomena. Nature Geoscience, 3(9), 599. doi:10.1038/ngeo940

Rogers, G. and H. Dragert (2003), Episodic tremor and slip on the Cascadia subduction zone: The chatter of silent slip, Science 300(5627): 1942-1943.

Riddell, A. R., King, M. A., Watson, C. S., Sun, Y., Riva, R. E. M., & Rietbroek, R. (2017). Uncertainty in geocenter estimates in the context of ITRF2014. Journal of Geophysical Research: Solid Earth, 122, 4020–4032. https://doi.org/10.1002/2016JB013698

Ruhl, C.J., Melgar, D., Geng, J., Goldberg, D.E., Crowell, B.W., Allen, R.M., Bock, Y., Barrientos, S., Riquelme, S., Baez, J.C. and Cabral-Cano, E. (2019). A global database of strong-motion displacement GNSS recordings and an example application to PGD scaling. Seismological Research Letters, 90(1), pp.271-279.

Saastamoinen, J. (1973), Contributions to the theory of atmospheric refraction, Bulletin Géodésique (1946-1975) 107(1): 13-34.

Saunders, J. K., D. E. Goldberg, J. S. Haase, Y. Bock, D. G. Offield, D. Melgar, J. Restrepo, R. B. Fleischman, A. Nema, J. Geng, C. Walls, D. Mann, G. Mattioli (2016), Seismogeodesy using GNSS and low-cost MEMS accelerometers: perspectives for earthquake early warning and rapid response, Bull. Seismol. Soc. Am., 106, 6, 2469–2489, doi: 10.1785/0120160062.

Schmidt, D. A., H. Gao (2010), Source parameters and time dependent slip distributions of slow-slip events on the Cascadia subduction zone from 1998-2008, J. Geophys. Res., doi:10.1029/2006RG000208.

Segall, P., E. Desmarais, D. Shelly, A. Miklius, and P. Cervelli (2006), Earthquakes triggered by silent slip events on Kilauea volcano, Hawaii, Nature, 442, doi:10.1038/nature04938.

Segall, P., and A. M. Bradley (2012), Slow-slip evolves into megathrust earthquakes in 2D numerical simulations, Geophys. Res. Lett., 39, L18308, doi:10.1029/2012GL052811.

Springer, T. A., G. Beutler, and M. Rothacher (1999), Improving the orbit estimates of GPS satellites, *Journal of Geodesy*, *73*, 147-157

Voss, N., T. H. Dixon, Z. Liu, R. Malservisi, M. Protti, S. Schwartz (2018), Do slow slip events trigger large and great megathrust earthquakes? Science Advances, 4, eaat8472, doi: 10.1126/sciadv.aat8472.

Wahr, J., Khan, S. A., van Dam, T., Liu, L., van Angelen, J. H., van den Broeke, M. R., & Meertens, C. M. (2013). The use of GPS horizontals for loading studies, with applications to northern California and southeast Greenland. Journal of Geophysical Research: Solid Earth, 118, 179.

Wang, Kelin, Yan Hu, & Jiangheng He (2012a). Deformation cycles of subduction earthquakes in a viscoelastic Earth, Nature, 484: 327-32.

Wang, H., Xiang, L., Jia, L., Jiang, L., Wang, Z., Hu, B., & Gao, P. (2012b). Load Love numbers and Green's functions for elastic Earth models PREM, iasp91, ak135, and modified models with refined crustal structure from crust 2.0. Computational Geosciences, 49, 1

Wang N., Yuan Y., Li Z., Montenbruck O., Tan B. (2016) Determination of differential code biases with multi-GNSS observations, Journal of Geodesy, Vol. 90, No. 3, pp. 209-228, DOI 10.1007/s00190-015-0867-4

Wang M., J. Wang, Y. Bock, H. Liang, D. Dong, P. Fang (2019), Dynamic Mapping of the Movement of Landfalling Atmospheric Rivers over Southern California with GPS Data, Geophys. Res. Lett, 46, https://doi.org/10.1029/2018GL081318.

Watkins, M. M., Wiese, D. N., Yuan, D.-N., Boening, C., & Landerer, F. W. (2015). Improved methods for observing Earth's time variable mass distribution with GRACE using spherical cap mascons. Journal of Geophysical Research: Solid Earth, 120, 2648–2671. https://doi.org/10.1002/2014JB011547

Wdowinski, S., Y. Bock, J. Zhang, P. Fang, and J. Genrich (1997), Southern California Permanent GPS Geodetic Array: Spatial filtering of daily positions for estimating

coseismic and postseismic displacements induced by the 1992 Landers earthquake, *J. Geophys. Res.*, *102*(B8), 18,057–18,070.

Williams, S. (2003), The effect of coloured noise on the uncertainties of rates estimated from geodetic time series, Journal of Geodesy 76(9-10): 483-494.

Williams, S. D. P., CATS: GPS coordinate time series analysis software, *GPS Solutions*, Vol. 12, No. 2, doi: 10.1007/s10291-007-0086-4, 2008.

Xiao, M., Koppa, A., Mekonnen, Z., Pagán, B.R., Zhan, S., Cao, Q., Aierken, A., Lee, H. and Lettenmaier, D.P. (2017), How much groundwater did Cifornia's Central Valley lose during the 2012–2016 drought? Geophysical Research Letters, 44(10), pp.4872-4879.

Yin, Haitao, Shimon Wdowinski, Xiqiang Liu, Weijun Gan, Bei Huang, Genru Xiao, and Shiming Liang (2013), Strong Ground Motion Recorded by High-Rate GPS of the 2008 M s 8.0 Wenchuan Earthquake, China, Seismological Research Letters, 84: 210-18.

Yue, Han, Thorne Lay, Luis Rivera, Chao An, Christophe Vigny, Xiaopeng Tong, and Juan Carlos Báez Soto (2014), Localized fault slip to the trench in the 2010 Maule, Chile Mw= 8.8 earthquake from joint inversion of high-rate GPS, teleseismic body waves, InSAR, campaign GPS, and tsunami observations, Journal of Geophysical Research: Solid Earth, 119: 7786-804.

Zeng, Y. and Shen Z-K. (2017), A Fault-Based Model for Crustal Deformation in the Western United States Based on a Combined Inversion of GPS and Geologic Inputs, Bulletin of the Seismological Society of America, 107: 2597-612.

Zenodo Web Page (2018): https://zenodo.org/record/1434374#.X-udln-YLQl

Zenodo Archive: https://zenodo.org/record/1434374/files/dataset_ruhl_etal_2018_version2.tar.gz?download=1

Zhang, J. (1996), Continuous GPS measurements of crustal deformation in Southern California, Ph.D. dissertation, Univ. of California San Diego.

Zumberge, J. F., M. B. Heflin, D. C. Jefferson, M. M. Watkins, and F. H. Webb (1997), Precise point positioning for the efficient and robust analysis of GPS data from large networks, *J. Geophys. Res.*, *102*(B3), 5005–5017.

Appendix

A1. Analyz_tseri options

See https://qoca.jpl.nasa.gov/advclass/tsa_intro.html for explanation of this driver parameters

A1.1 Analyz_tseri driver file

```
(e=======
*       << key word-controlled driving file format >>              *
*"s"mbol ":" must exist in command lines as index pointer           *
* any non-blank character at first column means comment line        *
* empt" "fter ":" means comment line too, but line appears in out file   *
```

clean_template_singleHost.drv (cleaned time series)

----------art 1 -- general i/o information

apriori value file:	APRIORI_FILE
input file:	TYPE_data_PROJECT.SEQ.list
sit_list file:	SITE_LIST
est_parameter file:	PARAM_FILE
output file:	reg_PROJECT.MODE.SEQ.out 2
residual file:	reg_PROJECT.MODE.SEQ.resi
res_option:	RES_OPTION
omitted_span file:	OMITSPAN_FILE
specific term_out file:	reg_PROJECT.MODE.SEQ.mdl
specific term_option:	SPEC_TERM_OPT
resi_file2:	reg_both_PROJECT.MODE.SEQ.resi
res2_option:	RES2_OPTION
mdl2_out:	reg_both_PROJECT.MODE.SEQ.mdl
mdl2_option:	MDL2_OPTION
enu_correlation usage :	yes
color_noise analysis model :	2
jump_day removal :	no
adjust_allsite option :	yes
oneline_netformat :	yes

```
cutoff criterion: unit: year, give a numerical number, for example
       2.5 means 2.5 years. It the data span of this site is less than 2.5
years,
       this site will be neglected.
       Such a criterion is necessary to avoid weak site, in particular for
velocity and seasonal
       term estimates.
```

cutoff criterion: 0.5

```
span and sigma factor to estimate jump apr value: unit: year, real value.
       This is one-side span. The analyze_tseri program will check if there
are
       effective jump parameters. If the answer is yes, the program will use
the data
       within the span around the jump epoch to estimate the apriori value of
the jump
       parameter. Then reset the apriori value of the jump parameter using
the estimated
```

```
       value and reset the jump parameter constraint using the formal
sigma*factor value.
       The default span value is 0.1 year. The default sigma factor is 0.2
(20%).
```

span and sigma factor to est jump apr (est_jump_span) : 0.5 20
weak_obs (big sigma) criteria : 40.0 40.0 80.0
outlier (big o-c) criteria mm : OC_OUTLIER_FILE
very bad_obs criteria mm : BAD_OBS_OUTLIER_FILE
t_interval: 1990.0 2099.0
minimum interval for parameter (t_est) : 0.587 0.934 0.550
end:
---------- art 2 -- apriori information

A.1.2 Residual output options

If the option is empty, that means output original time series and
hence the residual file is ignored.
The option is a bit map integer.
if bit(1) = 1 (number 1): the bias term is removed in residuals
if bit(2) = 1 (number 2): the secular motion is removed in residuals
if bit(3) = 1 (number 4): the annual terms are removed in residuals
if bit(4) = 1 (number 8): the semi-annual terms are removed in residuals
if bit(5) = 1 (number 16): the co-seismic jump terms are removed in residuals
if bit(6) = 1 (number 32): the user defined harmonic terms are removed in residuals
if bit(7) = 1 (number 64): the Spline function terms are removed in residuals
if bit(8) = 1 (number 128): the global quadratic terms are removed in residuals
if bit(9) = 1 (number 256): the global cubic terms are removed in residuals
if bit(10) = 1 (number 512): the modulation terms are removed in residuals
if bit(11) = 1 (number 1024): the postseismic decay terms are removed in residuals
if bit(12) = 1 (number 2048): the local polynomial terms are removed in residuals
if bit(13) = 1 (number 4096): the non-co-seismic jump terms are removed in residuals
For example, if the res_option = 29, that means the bias, jump, annual and semi-annual
terms are removed. The residuals contain the other terms, including
velocity (secular motion) term.

A.1.3 Model term output options

specific term output file: output time series with specified Terms.
specific term_option: option to select the specific terms.
If the option is empty, that means output nothing.
The option is a bit map integer.
if bit(1) = 1 (number 1): the bias term is included in the output terms.
if bit(2) = 1 (number 2): the secular motion is included in the output terms.
if bit(3) = 1 (number 4): the annual terms are included in the output terms.
if bit(4) = 1 (number 8): the semi-annual terms are included in the output terms.

if bit(5) = 1 (number 16): the co-seismic jump terms are included in the output terms.
if bit(6) = 1 (number 32): the user defined harmonic terms are included in the output terms.
if bit(7) = 1 (number 64): the Spline function terms are included in the output terms.
if bit(8) = 1 (number 128): the global quadratic terms are included in the output terms.
if bit(9) = 1 (number 256): the global cubic terms are included in the output terms.
if bit(10) = 1 (number 512): the modulation terms are included in the output terms.
if bit(11) = 1 (number 1024): the postseismic decay terms are included in the output terms.
if bit(12) = 1 (number 2048): the local polynomial terms are included in the output terms.
if bit(13) = 1 (number 4096): the non-co-seismic jump terms are included in the output terms.
For example, if the res_option = 29, that means the bias, jump, annual and semi-annual terms are included in the specific output file.

A.2 PCA Input file (e=======

```
*         << key word controlled driving file format >>              *
*“s”mbol ":" must exist in command lines as index pointer             *
* any non-blank character at first column means comment line          *
* empt“ ”fter ":" means comment line too, but line appears in out f=======
c-----------art 1 -- general i/o information
 job-type:                      regional filtering
 decomposition method:              PCA
 apriori value file:              itrf2008.net
 input site list file(site_list):    pca_trans.site
 input qob list file(in_list):      pca_data_jplATS.list
 output file:                    pca_jplATS.out
 component file:                   pca_jplATS.cpt
 regional filtered time series file: pca_jplATS.res
 spatial eigenvector file:          pca_jplATS.seign
 network range (sit_range, degree):  200.0 260.1 31.0 80.5
 solution span (soln_span):         1990.0 2020.0
 fill_gap option:                 yes
 adj_6par option:                  no
 outlier_sigma criterion (enu, mm):  50.0 50.0 100.0
 outlier_value criterion (enu, mm):  100.0 100.0 300.0
 minimum data percentage (cut_p):    10.0
 minimum station percentage (cut_t): 3.0
 reference frame:                  WGS84
 reference coordinate, rtime:       geodetic 2005.000
 end:
 exit:
```

A Principal Component Analysis (PCA) filter is applied to the cleaned time series. The PCA driver file settings are as follows and include additional outlier criteria.

network range (longitude, latitude, decimal degrees): 200.0 260.1 31.0 80.5
outlier_sigma criteria (enu, mm): 50.0 50.0 100.0
outlier_value criteria (enu, mm): 100.0 100.0 300.0
minimum data percentage (cut_p): 10.0
minimum station percentage (cut_t): 3.0
reference frame: WGS84
reference coordinate, rtime: geodetic 2014.006.

A.2 Weighted Mean of JPL and SOPAC solutions

Start with the JPL & SOPAC XYZ Raw_M files, e.g.,
http://garner.ucsd.edu/pub/measuresESESES_products/Timeseries/WesternNorthAmerica/WNAM_Raw_M_TrendNeuTimeSeries_jpl_20220203.tar.gz &

http://garner.ucsd.edu/pub/measuresESESES_products/Timeseries/WesternNorthAmerica/WNAM_Raw_M_TrendNeuTimeSeries_sopac_20220130.tar.gz

Given (Epoch by Epoch):

$$A_1 = \begin{bmatrix} X_1 \\ Y_1 \\ Z_1 \end{bmatrix}; (\text{X sig;} \quad \text{Y sig;} \quad \text{Z sig;} \quad \text{CorrXY;} \quad \text{CorrXZ;} \quad \text{CorrYZ})_1$$

$$A_2 = \begin{bmatrix} X_2 \\ Y_2 \\ Z_2 \end{bmatrix}; (\text{X sig;} \quad \text{Y sig;} \quad \text{Z sig;} \quad \text{CorrXY;} \quad \text{CorrXZ;} \quad \text{CorrYZ})_2$$

Form covariance matrix:

$$C_1 = \begin{bmatrix} (X\ sig)^2 & (X\ sig)(Y\ sig)\text{CorrXY} & (X\ sig)(Z\ sig)\text{CorrXZ} \\ (X\ sig)(Y\ sig)\text{CorrXY} & (Y\ sig)^2 & (Y\ sig)(Z\ sig)\text{CorrYZ} \\ (X\ sig)(Z\ sig)\text{CorrXZ} & (Y\ sig)(Z\ sig)\text{CorrYZ} & (Z\ sig)^2 \end{bmatrix}_1$$

$$C_2 = \begin{bmatrix} (X\ sig)^2 & (X\ sig)(Y\ sig)\text{CorrXY} & (X\ sig)(Z\ sig)\text{CorrXZ} \\ (X\ sig)(Y\ sig)\text{CorrXY} & (Y\ sig)^2 & (Y\ sig)(Z\ sig)\text{CorrYZ} \\ (X\ sig)(Z\ sig)\text{CorrXZ} & (Y\ sig)(Z\ sig)\text{CorrYZ} & (Z\ sig)^2 \end{bmatrix}_2$$

Align epochs between the JPL and SOPAC values

If an epoch missing both JPL and SIO, skip

If only JPL or SIO, use the one value and skip mean computation

Observation equations:

$A_1 = M + v_1$

$A_2 = M + v_2$

$\begin{bmatrix} A_1 \\ A_2 \end{bmatrix} = \begin{bmatrix} I \\ I \end{bmatrix} M + \begin{bmatrix} v_1 \\ v_2 \end{bmatrix}$

$P_1 = C_1^{-1}; P_2 = C_2^{-1}$

Weighted least-squares estimate:

$$\widehat{M} = \left(\begin{bmatrix} I & I \end{bmatrix} \begin{bmatrix} P_1 & 0 \\ 0 & P_2 \end{bmatrix} \begin{bmatrix} I \\ I \end{bmatrix} \right)^{-1} \begin{bmatrix} I & I \end{bmatrix} \begin{bmatrix} P_1 & 0 \\ 0 & P_2 \end{bmatrix} \begin{bmatrix} A_1 \\ A_2 \end{bmatrix}; I = \begin{bmatrix} 1 & 0 & 0 \\ 0 & 1 & 0 \\ 0 & 0 & 1 \end{bmatrix}$$

$\widehat{M} = [P_1 + P_2]^{-1}[P_1 A_1 + P_2 A_2]$

$$C_{\widehat{M}} = \hat{\sigma}^2 [P_1 + P_2]^{-1}; \hat{\sigma}^2 = \hat{v}^T \begin{bmatrix} P_1 & 0 \\ 0 & P_2 \end{bmatrix} \hat{v}\ ;\ \hat{v} = \begin{bmatrix} A_1 - \widehat{M} \\ A_2 - \widehat{M} \end{bmatrix} = \begin{bmatrix} A_{X1} - \widehat{M}_X \\ A_{Y1} - \widehat{M}_Y \\ A_{Z1} - \widehat{M}_Z \\ A_{X2} - \widehat{M}_X \\ A_{Y2} - \widehat{M}_Y \\ A_{Z2} - \widehat{M}_Z \end{bmatrix} \ldots$$

Since there is only one degree of freedom in the computation of $\hat{\sigma}^2$ and none in the case of only a JPL or SOPAC solution, we do not scale the covariance matrix. Also, $\hat{v}$ may have a zero value if the two solutions are identical. Therefore, we only use $\hat{\sigma}^2$as a diagnostic. If it is much greater than 1, it may point to an outlier in one of the solutions that could be the basis for further investigation.

This is now Raw_MC:

$\widehat{M} = \begin{bmatrix} X_C \\ Y_C \\ Z_C \end{bmatrix}$; combined XYZ values

Convert $C_{\widehat{M}}$ *to* $Coor_{\widehat{M}}$

$$C_{\widehat{M}} = \hat{\sigma}^2 \begin{bmatrix} (Xsig)^2 & (XY\ sig) & (XZ\ sig) \\ (XY\ sig) & (Ysig)^2 & (YZ\ sig) \\ (XZ\ sig) & (YZ\ sig) & (Zsig)^2 \end{bmatrix}_C$$

$$Corr_{\widehat{M}} = \begin{bmatrix} 1 & \frac{(XY\ sig)}{(Xsig)(Ysig)} & \frac{(XZ\ sig)}{(Xsig)(Zsig)} \\ \frac{(XY\ sig)}{(Xsig)(Ysig)} & 1 & \frac{(YZ\ sig)}{(Ysig)(Zsig)} \\ \frac{(XZ\ sig)}{(Xsig)(Zsig)} & \frac{(YZ\ sig)}{(Ysig)(Zsig)} & 1 \end{bmatrix} = \begin{bmatrix} 1 & CorrXY & CorrXZ \\ CorrXY & 1 & CorrYZ \\ CorrXZ & CorrYZ & 1 \end{bmatrix}$$

The combined (c) data points then are output as:

$(Dec\ Yr;\ \ Yr;\ \ DayOfYr;\ X;\ Y;\ Z;$ X sig; Y sig; Z sig; CorrXY; CorrXZ; CorrYZ; $\hat{\sigma}^2)_C$

Convert to N,E,U at each epoch using first mean value and WGS84 ellipsoid

$$\begin{bmatrix}\Delta N_i(t_i)\\ \Delta E_i(t_i)\\ \Delta U_i(t_i)\end{bmatrix} = \begin{bmatrix}-sin\phi cos\lambda & -sin\lambda sin\phi & cos\lambda\\ -sin\lambda & cos\phi & 0\\ cos\lambda cos\phi & cos\phi sin\lambda & sin\phi\end{bmatrix}_{t_0} \left\{\begin{bmatrix}X_i(t_i)\\ Y_i(t_i)\\ Z_i(t_i)\end{bmatrix} - \begin{bmatrix}X_{t_0}\\ Y_{t_0}\\ Z_{t_0}\end{bmatrix}\right\}$$

Run weighted mean time series through ATS, run post-ATS to created new combination tar files.

A.3 Estimating parameter uncertainties for displacement time series

Note: this has not yet been implemented (see section 2.1.10)

We use a weighted least squares analysis of the 1-D displacement vector $\boldsymbol{y}$ to estimate the vector of the model parameters $\boldsymbol{x}$.

$$\boldsymbol{y} = \boldsymbol{A}\boldsymbol{x} + \boldsymbol{\varepsilon};\ E\{\boldsymbol{\varepsilon}\} = \boldsymbol{0};\ D\{\boldsymbol{\varepsilon}\} = \sigma_0^2 \boldsymbol{C}_{\boldsymbol{\varepsilon}} \qquad (14)$$

where the error $\boldsymbol{\varepsilon}$ is assumed to be unbiased and have the unscaled covariance matrix $\boldsymbol{C}_{\boldsymbol{\varepsilon}}$. We assume a power law function according to Williams (2003) and express the covariance matrix $\boldsymbol{C}_{\boldsymbol{\varepsilon}}$ as the sum of a time-independent "white noise" matrix and a time-dependent "colored noise" matrix such that:

$$\boldsymbol{C}_{\boldsymbol{\varepsilon}}(t) = a^2\boldsymbol{I} + b_{\kappa}^2\boldsymbol{J}_{\kappa}(t)$$

Coefficients a^2 and b^2 are the magnitude of white noise (uncertainties in the daily displacements) and colored noise, respectively, and $\boldsymbol{\kappa}$ is the spectral index**.** We estimate b and κ through the following steps to construct $\boldsymbol{C}_{\boldsymbol{\varepsilon}}$.

A3.1 Estimating the Spectral Index of Colored Noise

To estimate the spectral indices of the colored noise for each of the three components, we calculate the Lomb-Scargle periodogram of the time series residuals (time series displacements – the estimated time series model) for each component. To do this, we calculate the Lomb-Scargle periodogram of the time series residuals (time series displacements – the estimated time series model) for each component. We chose to compute the Lomb-Scargle periodogram because it can incorporate irregularly spaced data.

In order to estimate the spectral index (κ) of each component, we start with the equation for a power law function (equation [10] of Williams (2003)):

$$P = \frac{(D_{\kappa} * b_{\kappa}^2)}{(f_s^{\frac{\kappa}{2}+1})} * f^{\kappa} \qquad [1]$$

Where f^{κ} is the spatial or temporal frequency, $D_{\kappa} = 2 * 2\pi^{\kappa} * 1^{\frac{\kappa}{2}}$, modifying the equation (11) from Williams (2003) for using decimal year instead of seconds, and $f_s = 365$, or daily displacements

If we take the log10 of both sides of this equation, we end up with an equation for a linear function $y = b + ax$,

$$log10(PS) = log10\left(\frac{(D_{\kappa} * b_{\kappa}^2)}{\left(f_s^{\frac{\kappa}{2}+1}\right)}\right) + \kappa * log10(f^{\kappa}) \quad [2]$$

where y = log10(P), x = log10(f^{κ}), slope, $a = \kappa$, and y intercept is

$$b = log10\left(\frac{(D_{\kappa} * b_{\kappa}^2)}{\left(f_s^{\frac{\kappa}{2}+1}\right)}\right) \quad [3]$$

From this relationship, we can estimate a best-fit line to the computed power and frequency in log-log space, which will estimate the slope (spectral index, κ), and the best-fit y-intercept value (b). An example fit is presented in Figure A1. To avoid white noise affecting our estimate as much as possible, we exclude the highest frequencies greater than log10(1/15) days in the best-fit line estimation (Nikolaidis, 2002).

A3.2 Calculating the Amplitude of Colored Noise

Once we have estimated the spectral index κ for our components, we can now calculate the amplitude of the colored noise (b_{κ}) for each component using a rearranged equation [3]:

$$b_{\kappa} = \sqrt{\left(\frac{10^{b}}{D_{\kappa}} * f_s^{\frac{\kappa}{2}+1}\right)} \quad [4]$$

A3.3 Constructing the Colored Noise Covariance Matrix

To calculate the full covariance matrix $\boldsymbol{C_{\varepsilon}}$ for each component, we need the daily displacement uncertainty (one-sigma) a, the amplitude of colored noise b_{κ}, and the colored noise covariance matrix $J_{\kappa}(t)$. Constructing $J_{\kappa}(t)$ involves calculating the transformation matrix $\mathbf{T}$ from equation [8] of Williams (2003) and scaling it appropriately:

$$\boldsymbol{J_{\kappa}}(t) = \mathbf{T}\mathbf{T}^{\mathbf{T}}$$

$$\mathbf{T} = \Delta T^{-\frac{\kappa}{4}} \begin{bmatrix} \psi_0 & \cdots & 0 \\ \vdots & \ddots & \vdots \\ \psi_n & \cdots & \psi_0 \end{bmatrix} \quad [5]$$

with sampling interval $\Delta T = (length\ of\ time\ series)/(n-1)$, where length is in decimal year units and n = the number of total observations in the component time series. The expanded form of $\mathbf{T}$ is

$$\mathbf{T} = \Delta T^{-\kappa/4} \begin{bmatrix} \psi_0 & 0 & 0 & \cdots & 0 \\ \psi_1 & \psi_0 & 0 & \cdots & 0 \\ \psi_2 & \psi_1 & \psi_0 & \cdots & 0 \\ \cdots & \cdots & \cdots & \cdots & \cdots \\ \psi_N & \psi_{N-1} & \psi_{N-2} & \cdots & \psi_0 \end{bmatrix} \quad [6]$$

where the matrix is a lower-left triangular matrix filled with ψ values as a function of row – column number. Using the gamma function Γ, the following describes ψ from equation [9] of Williams (2003):

$$\psi_n = \frac{\Gamma\left(n-\left(\frac{\kappa}{2}\right)\right)}{\left(n!\,\Gamma\left(-\frac{\kappa}{2}\right)\right)} \quad [7]$$

where Williams (2003) describes that for the case where n → ∞ we can take:

$$\psi_n \sim \frac{\left(n^{\frac{-\kappa}{2}-1}\right)}{\Gamma\left(-\frac{\kappa}{2}\right)} \quad [8]$$

Once we have constructed $\boldsymbol{J_\kappa}(t)$, we can now calculate the full data covariance matrix as in:

$$\boldsymbol{C_\varepsilon}(t) = a^2\boldsymbol{I} + \boldsymbol{b_\kappa^2 J_\kappa}(t) \quad [9]$$

where the white noise component is constructed from a diagonalized matrix of the data measurement variances, and the colored noise component is formed from the $\boldsymbol{J_\kappa}(t)$ matrix scaled by the amplitude of colored noise. Now, the model term covariance matrix $\boldsymbol{C_{\hat{x}}}$ can be calculated from the weighted least squares inversion,

$$\hat{\boldsymbol{x}} = (\boldsymbol{A^T C_\varepsilon^{-1}}(t)\boldsymbol{A})^{-1}\boldsymbol{A^T C_\varepsilon^{-1}}(t)\boldsymbol{y}) \quad [10]$$

as

$$\boldsymbol{C_{\hat{x}}} = \sigma_0^2(\boldsymbol{A^T C_\varepsilon^{-1}}(t)\boldsymbol{A})^{-1} \quad [11]$$

The uncertainties calculated from this covariance matrix will now incorporate the effects of both white and colored noise.

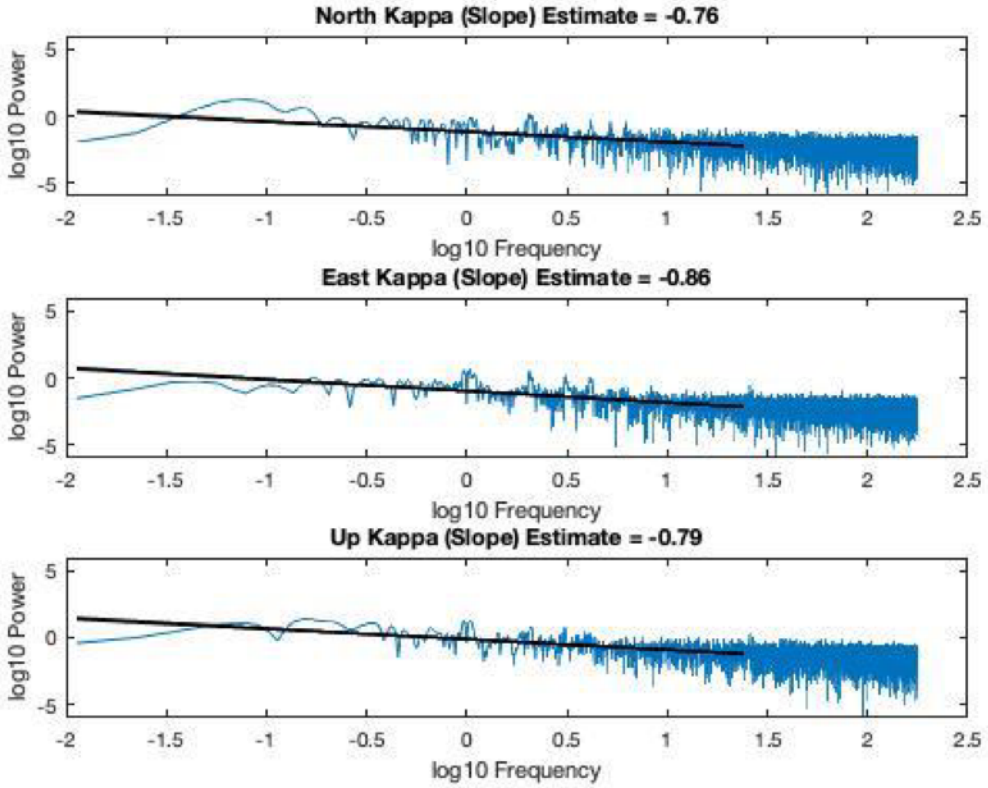

Figure A1. Example plotted log10 of the computed Lomb-Scargle periodogram (blue) with an estimated best fit y = ax + b linear function plotted on top (in black) for station VNPS. Frequencies greater than log10(1/15) days are excluded in the best-fit line estimation.